QUANTITATIVE METALLOGRAPHY TRACKING AND ANALYSIS FOR THE SCANNING LASER EPITAXY PROCESS APPLIED TO CMSX-4 AND RENÉ-80 NICKEL-BASED SUPERALLOYS

A Thesis
Presented to
The Academic Faculty

by

Justin Gambone

In Partial Fulfillment
of the Requirements for the Degree
Masters of Science in the
School of Mechanical Engineering

Georgia Institute of Technology
December 2012

QUANTITATIVE METALLOGRAPHY TRACKING AND ANALYSIS FOR THE SCANNING LASER EPITAXY PROCESS APPLIED TO CMSX-4 AND RENÉ-80 NICKEL-BASED SUPERALLOYS

Approved by:

Dr. Suman Das, Committee Chair
School of Mechanical Engineering
Georgia Institute of Technology

Dr. Arun Gokhale
School of Material Science
Georgia Institute of Technology

Dr. Yan Wang
School of Mechanical Engineering
Georgia Institute of Technology

Date Approved: 10/30/2012

TABLE OF CONTENTS

LIST OF TABLES

LIST OF FIGURES

SUMMARY

This thesis involves the development of digital algorithms for the microstructural analysis of metallic deposits produced through the use of Scanning Laser Epitaxy (SLE). SLE is a new direct digital manufacturing (DDM) technique which allows for the creation of three dimensional nickel-based superalloy components using an incremental layering system. Using a bed of powder placed on an underlying substrate and a laser propagating a melt-pool across the sample, a layer of material can be added and through the careful control of SLE settings various microstructures can be created or extended from the substrate. To create parts that are within specified microstructure tolerances the ideal SLE settings must be located through experimental runs, with each material needing different operating parameters. This thesis focuses on improving the microstructural analysis by use of a program that tracks various features found in samples produced through the SLE technique and a data analysis program that provides greater insights into how the SLE settings influence the microstructure. Using this program the isolation of optimal SLE settings is faster while also providing greater insights into the process than is currently possible.

The microstructure recognition program features three key aspects. The first evaluates major characteristics that typically arise during the SLE process; such as sample deformation, the aspects of a single crystal deposit, and the total deposit height. The second saves the data and all relevant test settings in a format that will allow for future analysis and comparison to other samples. Finally, it features a robust yet rapid execution so it may be used for entire runs of SLE samples, which can number up to 25, within a week. The program is designed for the types of microstructure found in CMSX-4 and René-80, specifically single crystal and equiaxed

regions.

The data fitting program uses optimally piecewise-fitted equations to find relationships between the SLE settings and the microstructure traits. The data is optimally piecewise fitted as the SLE process is a two-stage procedure, establishing then propagating the melt-pool across a sample, which creates distinct microstructure transitions. Using the information gathered, graphs provide a visual aid to better allow the experimenter to understand the process and a DOE is performed using sequential analysis; allowing the previously run samples to influence the future trials, reducing the amount of materials used while still providing great insight into the parameter field. Having access to the microstructure data across the entire sample and an advanced data fitting program that can accurately relate them to the SLE settings allows the program to track and optimize features that were never before possible.

CHAPTER I

INTRODUCTION

Scanning Laser Epitaxy (SLE) is a new direct digital manufacturing (DDM) technology being developed by the Direct Digital Manufacturing Lab at Georgia Tech, that allows for the creation of three dimensional nickel-based superalloy components using an incremental layering system. The goal of the development effort is to create functionally graded components, with specified microstructure and other attributes, to allow the formation of heterogeneous multifunctional components (HMCs). HMCs are commonly found in the aerospace industry due to the extreme temperatures and pressures that are prevalent within a turbine engine during operation. Hot sections, critical parts of the engine that are used to extract energy from the high temperature and high pressure environment created by the combustor, are the current focus for the application of the SLE technique.

Figure 1: Aero-engine turbine blade [17]

Hot section turbine engine components such as turbine blades are made of advanced nickel-based superalloys, materials that exhibit the ability to withstand large loads at high temperatures and pressures, with a complex geometry, to allow for the cooling of the blade through the incorporation of airflow, and an advanced microstructure, which increases the load the superalloy can sustain during operation. The SLE manufacturing technique is capable of working with advanced nickel-based superalloys, conforming to the shape of the component and extending the existing microstructure into the repaired section.

SLE can produce a three-dimensional object through the creation of individual layer deposits. The underlying substrate, which can be either an initial seeding piece or a previously created layer, has a metal powder placed over it before processing begins. For each layer a highly focused laser is used to establish a meltpool along the width of the sample and propagate it along the sample length using a raster scan. To minimize waste and reduce costs, several steps are taken before attempting a deposit on a turbine blade. Simple coupons of the same composition to the turbine blade alloy are used during three earlier stages; first a rectangular layout is considered, followed by a wave deposit and finally to a turbine blade shaped deposit as shown in Figure 2.

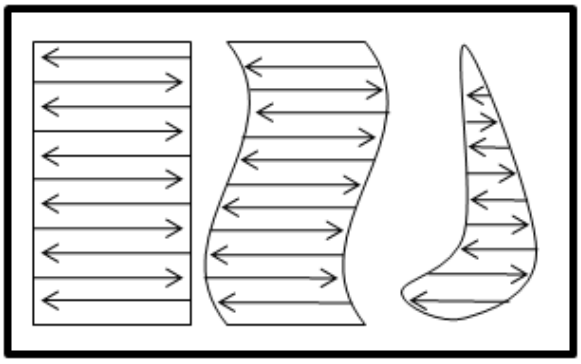

Figure 2: Rectangular, wave and turbine blade raster scans.

When processing a sample, the meltpool established by the laser must melt both

the powder and a portion of the underlying substrate to allow any underlying microstructure to be extended into the newly developed segment, as seen below. The laser must also be moved rapidly to induce surface tension gradients that pull powder into the meltpool, feeding the process as it progresses along the sample length.

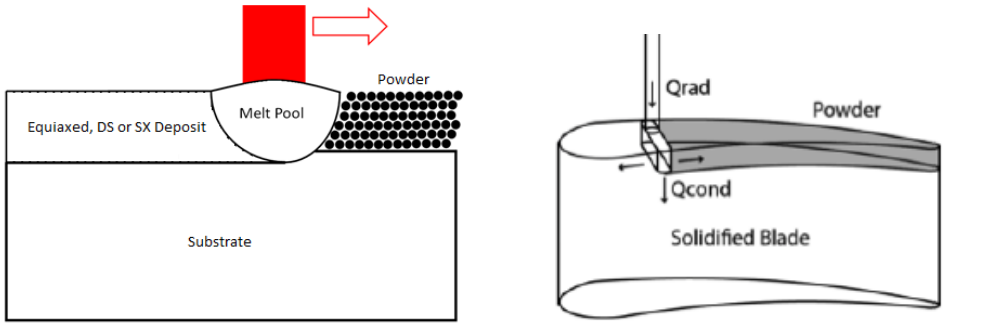

(a) SLE Process sideview (b) SLE Process used on a turbine blade

Figure 3: SLE Process Overview

At present, the primary application of the SLE process is in the creation and repair of turbine blades for the aerospace industry. The final blade can be comprised of multiple microstructures throughout its volume including single crystal (SX), columnar and equiaxed. By remelting a small portion of a substrate, any of the microstructure used in the previous section of the turbine blade can be extended into the new area. This is important for single-crystal components as it allows for the creation of new material without a grain boundary, a necessity that has to this day branded SX materials as non-weldable. The process also mitigates other problems, such as hot tearing and cracks, that arise in other repair techniques.

The development of SLE for a new alloy requires the optimization of its three primary settings: laser power, the laser scanning speed and the number of repeated scans performed at the initial edge of the sample to establish a meltpool. These three settings allow for the establishment of a stable meltpool and temperature gradient which will effectively seed and grow any desired microstructure within the newly placed material. The three research areas that lend to complete microstructure control

are process modeling, properly controlling the creation of a part and characterization. By creating a model of the system, the number of experimental runs needed to find the ideal settings for a part is reduced; this lowers the material cost while improving the efficiency for SLE. When creating a part, the use of an advanced control system allows for an exact heat distribution to be created for each layer while also giving the process the ability to conduct on-the-fly repairs to keep the sample within the specified guidelines. Finally, for each manufactured part, the microstructure must be analyzed to determine what occurred at the runtime settings and to find how the settings can be improved for the final product.

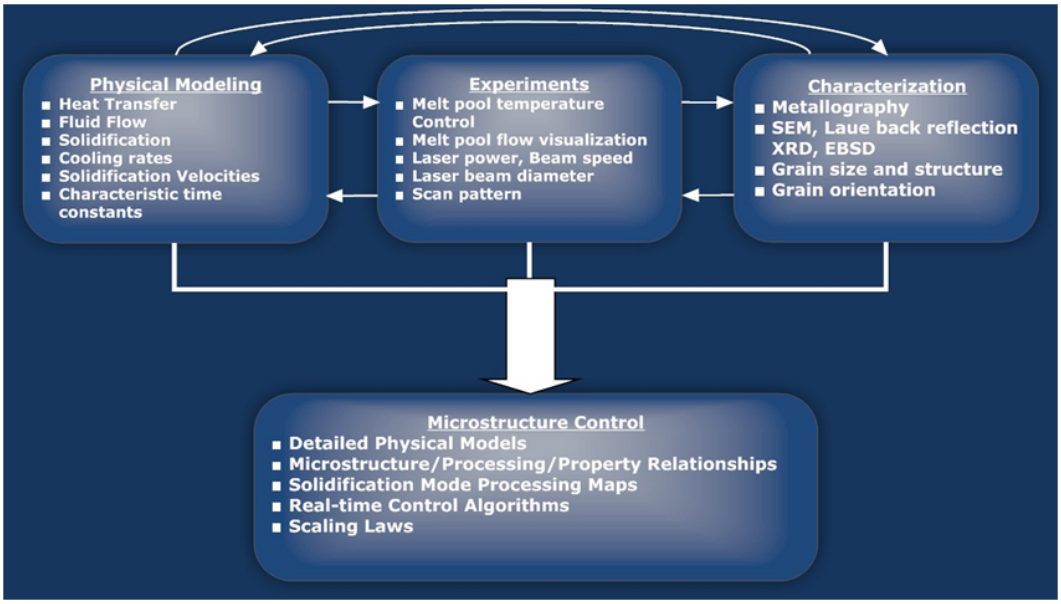

Figure 4: Direct Digital Manufacturing

At present, the focus is on developing the SLE process for three superalloys common to the aerospace industry; Mar-M-247, René-80 and CMSX-4. Initial trials have been performed on test coupons of simplified geometry for all three materials with significant results. The development of SLE running conditions for Mar M-247 has been completed to within specified conditions provided by ONR with the final result seen in Figure 5.

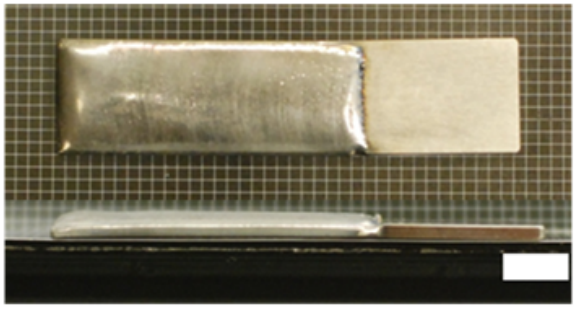

Figure 5: Macro image of a Mar M-247 sample after processing.

After performing a lengthwise cut along the center line of a sample and imaging the exposed surface three primary observations can be made. A fully dense deposit was achieved across the entire sample length, a complete metallurgical bond was formed between the cast substrate and the newly processed material and finally, no hot tearing or cracking occurred during the process or after a post-process heat treatment. Figure 6 outlines the meltback depth of two samples with white lines and contrasts the microstructure before and after a stress relief heat treatment at 1067^oC.

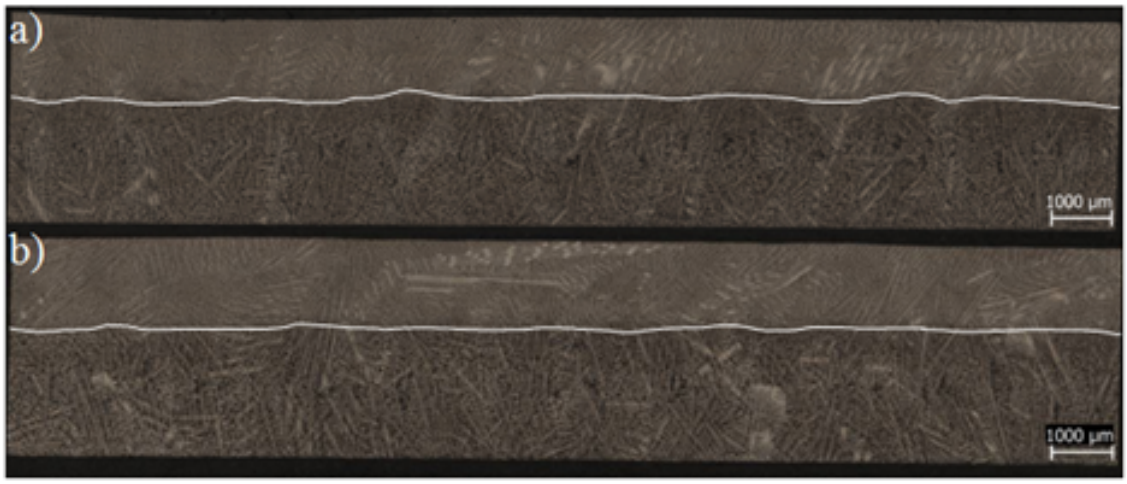

Figure 6: Top: Longitudinal micrograph of a Mar M-247 sample. Bottom: Longitudinal micrograph of a heat treated Mar M-247 sample.

The processing conditions for René-80 are currently being investigated to find the optimal parameters at which to create future parts. At this time, fully dense equiaxed René-80 deposits have been produced on René-80 cast rectangular test coupons as

shown in Figure 7. Inspection shows that a complete metallurgical bond has been created along the entire length of the sample with no evidence of cracking or hot tearing.

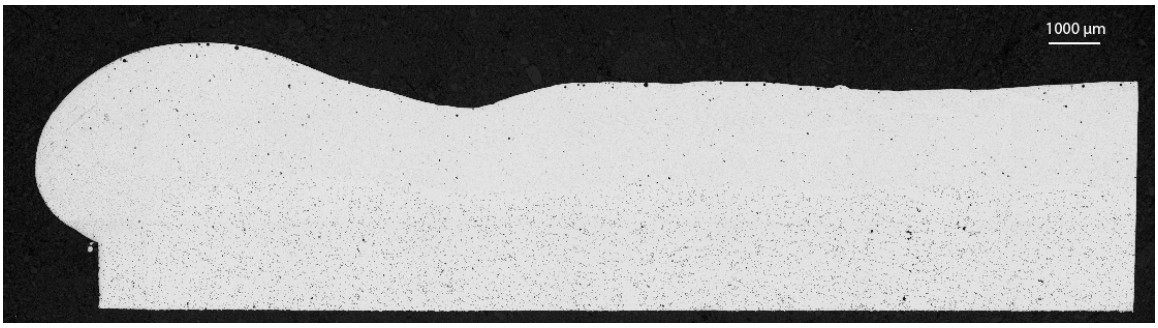

Figure 7: Longitudinal micrograph of a René-80 sample.

The third material currently being investigated for the SLE process is CMSX-4, a Ni-based superalloy that has a single crystal microstructure. A fully dense deposit has can be produced on investment cast single crystal plates with a complete metallurgical bond across the entire length while showing no evidence of cracking, porosity or hot tearing. Most importantly the single-crystal microstructure found in the cast section was successfully extended into the newly developed region; maintaining one single boundary across the processed part.

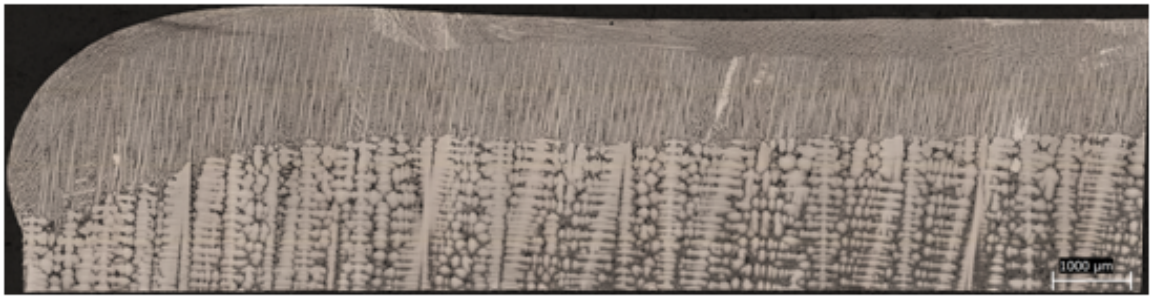

Figure 8: Longitudinal micrograph of a CMSX-4 sample.

For each of the materials being processed with SLE, a set of parameters were required to be explored to isolate the optimal operating range, including: the laser power, laser scanning speed, number of repeats and the amount of powder deposited.

When developing the SLE settings for each material the corresponding microstructure must be analyzed for positive and negative attributes so that the best parameter values can be found that keep the samples within tolerance while mitigating unwanted features.

An example of carefully considering a parameter is the development of the laser power setting. The lower the power level, the less intense of a meltpool is formed and when sufficiently weak the meltpool may not extend into the underlying substrate, instead only being encompassed by the melted powder. When this occurs, a lack of fusion between the substrate and newly deposited material occurs and is regarded as an unacceptable feature. When the laser power is very high the substrate and new deposit can be properly fused but it may be found that the meltpool extends excessively into the substrate. A laser power must be chosen that avoids these negative attributes to create an ideal setting while also considering all of the other SLE parameters.

This thesis focuses on improving the microstructure analysis by use of a program that tracks various features found in samples produced through the SLE technique, a data fitting program that provides greater insights into how the SLE settings influence the microstructure and a DOE program that helps find future operating conditions worthy of exploration. This technique only uses optical micrographs and can be quickly completed using a typical laboratory computer through the use of Matlab to provide rapid feedback for future experiments. The motivation for this thesis is to create a system for identifying ideal parameters that bridges the low end microstructure tracking, conducted by eye or basic feature recognition programs, and the more time-consuming and costly techniques, such as EBSD.

The microstructure tracking program is designed to locate several features shared between the three materials being explored including meltback depth, sample deformation and deposit height. The total deposit height must be found to compare

against minimum desired deposit height required to satisfy repair criteria for a given turbine blade. The sample deformation, the warping of the test coupon due to excess energy being introduced into the sample during processing, must be minimized as much as possible to avoid placing any additional stress on a repaired blade. The meltback depth must extend into the substrate to allow proper fusion between the cast section and newly deposited layer but a large meltback depth needs to be avoid damage to cast features existing on the repaired component. Figure 9 shows a microstructure feature unique to the CMSX-4 samples, single-crystal deposit height. When repairing CMSX-4 parts only the [001] single-crystal microstructures is desired and all other microstructure located near the top of the part must be removed, this topic is discussed in detail later in the thesis, essentially making the SX deposit height equivalent to the total deposit height for CMSX-4 samples.

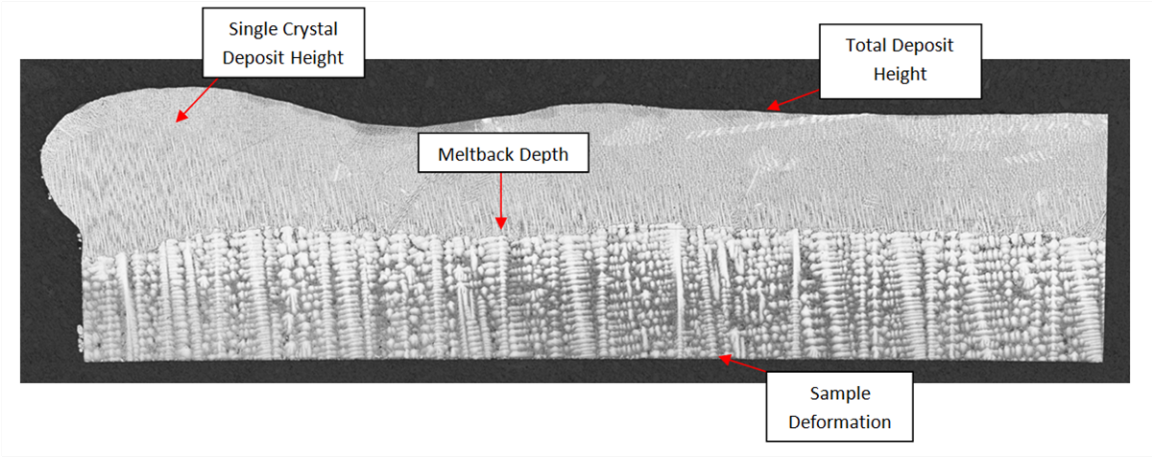

Figure 9: Cross-sectional image of CMSX-4 with listed features.

Figure 10 shows two additional features that are unique to CMSX-4 in this microstructure tracking program; the primary dendrite angle and the primary dendrite trunk width. A tolerance is usually specified for the amount the primary dendrite angle of the SX deposit may deviate relative to the cast sections primary dendrite angle. The width of the dendrite is important to understand the impact on the deposit's thermo-mechanical properties.

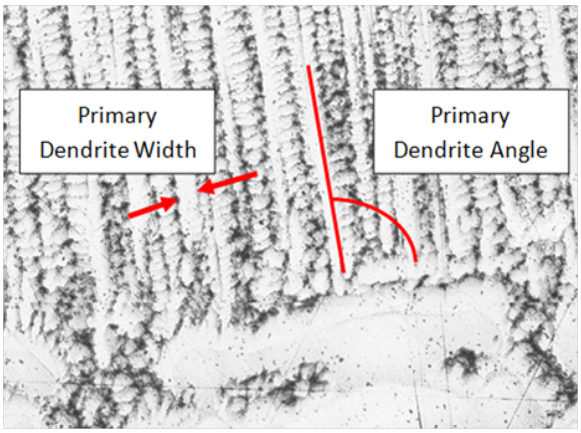

Figure 10: Cross-sectional image of CMSX-4 with primary dendrite angle and width labeled.

A René-80 sample, Figure 11, details the final three microstructure features that are explored. Pores and cracks are two occurrences most commonly found in René-80 samples and must be mitigated in final parts to stay within the bounds set by ONR. The lack of fusion in a sample, when the meltpool does not extend into the cast section of the sample, can be found in all of the materials being explored and is not an acceptable feature in a final product.

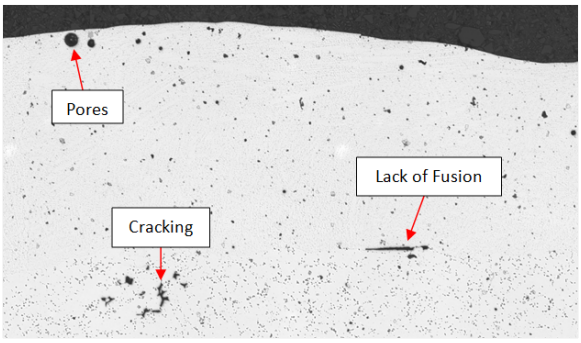

Figure 11: Cross-sectional image of René-80 with listed features.

The SLE process needs this mid-range microstructure tracking and analysis program to find the optimal settings for every new material, microstructure layout, deposit height, sample size, etc. This program is also necessary since the SLE technique is currently being used for casting repair and other programs are not designed to distinguish between different manufacturing techniques. An example is that of EBSD

which provides great detail of the single-crystals orientation across an entire CMSX-4 sample but does not differentiate between the cast and laser-processed regions.

Creating a custom data analysis program that works with the microstructure tracking program allows the inclusion of features never before considered to now have weight in choosing processing parameters, while also allowing the inclusion of every useful sample, due to its rapid execution. Relations can be better presented to the user through the use of various plots so that the information may be visualized in a manner that enhances the experimenter's understanding of the SLE process. The final aspect of the thesis deals with finding ideal locations for further testing. By combining the information gathered in the data analysis program and weighing the importance of each microstructure feature, a set of suggested areas of exploration is given to the user, and upon choosing where the next set of experiments will be conducted, a DOE is created to provide the best insight.

CHAPTER II

MOTIVATION

The initial purpose of the SLE process is to repair damaged and worn turbine engine hot section component such as turbine blades. Hundreds of turbine blades are used in a single engine and are critical to its high efficiency operation. After extended use, the edges of the turbine blade, which are located near the inner wall of the engine, begin to degrade and after as little as one millimeter of wear on a turbine tip the efficiency of the engine can drop drastically, caused by the excess air that can now bypass the turbine blade through the exposed section. Wear causes the most significant drop in efficiency in smaller engines as the wear section represents a larger portion of the flow path annulus height, and it is the turbine blades associated with these smaller engines that is the focus for the current SLE research. [11]. This makes it vital to keep well-formed turbine blades in an engine at all times and necessitates the removal of any blade that does not allow for high efficiency operation. Normally the worn turbine blades are not repaired and are instead replaced with a new blade; this drives the operational cost of the engine very high as a single blade can cost hundreds to thousands of dollars. The average expected lifecycle of a turbine blade is approximately three years, or 5 million miles of flight, though each blade must be routinely checked for earlier failure [40]. Turbine blade tip repair is a promising area of study and is being pursued to allow for a low cost alternative to the current replacement program.

Several processes are being developed to work with advanced materials like Ni-based superalloys, though all have significant problems. Selective laser melting (SLM), direct metal laser sintering (DMLS), and shape deformation manufacturing (SDM)

Figure 12: Turbine blade with excessive wear at the tip.

tend to have similar flaws in their repair work. Excessive meltback depth and warping can lead to delamination of layers and cracking in the samples [36, 30, 51]. If the melt viscosity is too high during a process then a problem that can easily arise is the creation of small spheres at the laser interaction area, known as balling [2]. During the solidification of the sample, if the strain caused by the shrinkage cannot be accounted for in the elastic and plastic deformation of the material then hot tearing can occur [50]. The level of microstructure control and formation are also problematic for competing repair techniques. Nickel-based superalloys have shown a strong susceptibility to stray grain formation during manufacture, especially with processes like SLM, and unlike the SLE process the aforementioned manufacturing techniques are incapable of extending a single crystal microstructure [37, 45].

There are two techniques that are direct competitors for SLE repair work; LENS and ELMF. LENS, laser engineered net shaping, uses a laser to establish a meltpool on a piece of substrate then injecting powder into the meltpool to deposit new material. The powder feeder then follows the laser to deposit a new layer of material [24].

When injecting the metal powder into the meltpool there is a possibility that some of the powder will not melt, leaving behind trace areas of unmelted powder. Another

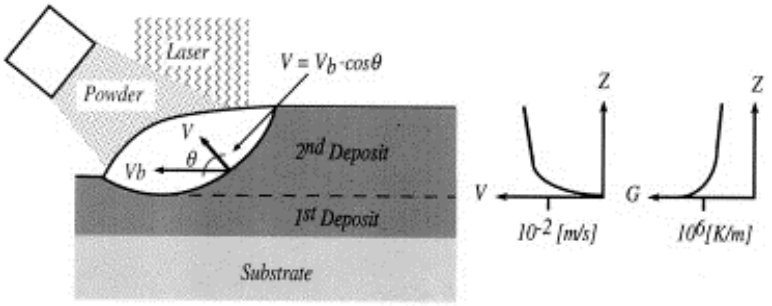

Figure 13: Longitudinal schematic along clad centerline for Laser Engineered Net Shaping. [22].

issue with this technique is the occurrence of hot tearing as the sample cools and re-solidifies.

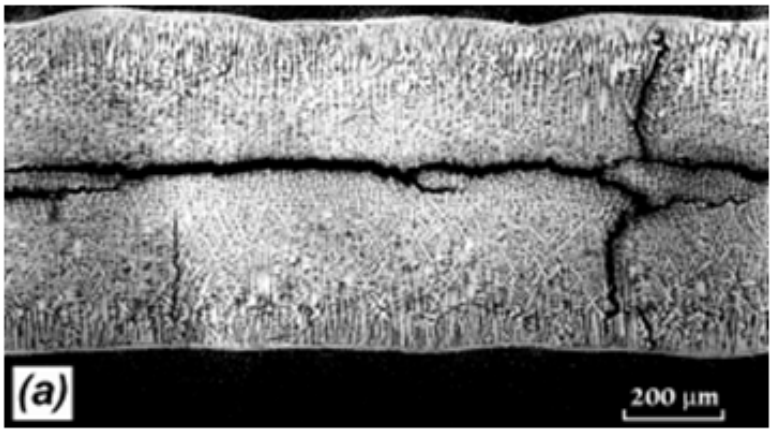

Figure 14: Crack formation on PWA-1480 discs [44].

ELMF, epitaxial laser metal forming, uses the same powder injection method as LENS but utilizes multiple displacements of the laser beam. A common issue with this technique is a lack of thermal control when attempting complex geometry, which has a negative effect on the microstructure creation. Another problem is the creation of unintended microstructure due to the flow of powder creating convection of broken dendrites.

The issues that arise in the listed processes are not found, or are greatly diminished, in the SLE process when the optimal parameters are used for each specific

material. Reducing these problematic features while creating the needed microstructure within the part makes finding the optimal SLE settings for each alloy a high priority. The process hinges on three primary variables that can be controlled during the process; laser power, laser scanning speed and the number of initial repeated scans. In order to find the optimal settings for each new material a large series of experiments must be conducted. For each experiment a metallographic image is used to evaluate several broad microstructural characteristics and problematic features. The previous method of SLE parameter exploration started with basic trends initially found through naked eye comparison and intuition before moving onto more controlled experiments once an operating range has been established.

Additional data is collected using more advanced microstructural tracking techniques, such as EBSD. EBSD tracks the diffraction patterns that exist when an object is sampled with a scanning electron microscope. The output, an orientation map, shows the orientation of the microstructure across the entire image and provides insight into the grain structures [26]. An example of an EBSD image is shown in Figure 15. There are several drawbacks to EBSD, for single crystal materials it can find the angle of orientation of the microstructure but is incapable of differentiating between the cast and reprocessed regions. Also, if an EBSD machine is not directly available, the cost can be high and the turnaround time can be long. Without a fast image return the results found in the analysis may not influence the next set of experiments.

In the past, after a suspected trend for every parameter had been found and a general area of interest had been located, several DOEs were conducted to find the best settings. Using the simple parameter measurements, like laser power, the DOEs performed find trends and the optimal variable values to repeatedly create the best samples possible. The DOE programs used provide only moderately useful information as they are incapable of fitting predictions accurately to the complex microstructure and cannot be used to optimize several important features.

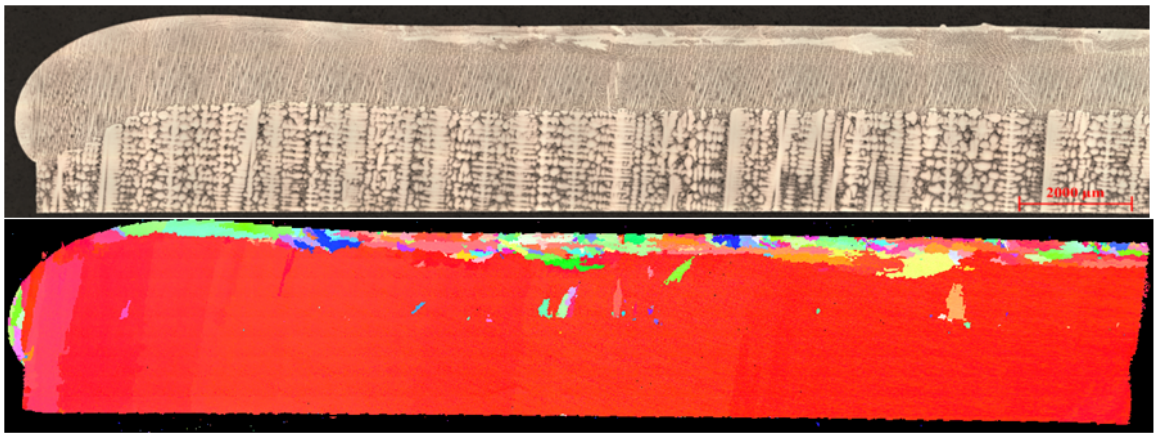

Figure 15: Top: Longitudinal micrograph of a CMSX-4 sample. Bottom: Corresponding EBSD orientation map.

A major hinderance with the DOE software is the microstructure representation. Given a tolerance such as the minimum deposit height, the sample micrograph would undergo a quick inspection at that tolerance level. Any portions of the image beyond the threshold, in this example a low deposit height, is tabulated. After searching the entire image the amount within tolerance is totaled and saved, this provides a single scalar value to be used in the DOE. Figure 16 shows an example for the minimum deposit height, where green sections are good and red sections are bad, and maximum allowable meltback depth. The percentage of the samples that are within tolerance, the green sections, are the points totaled. As can be seen in the images the resulting scalar values do not provide any insight into where the problematic areas are occurring or how badly the section may pass the threshold.

Creating a microstructural feature recognition program that directly interfaces with a data analysis system allows for greater improvement over the previous method. For features already being considered, such as meltback depth, the advanced tracking system performs a more comprehensive search and records a larger amount of data for later use. Instead of finding a single scalar value using a threshold technique, each point of the feature is found and saved. For the meltback depth this amounts to

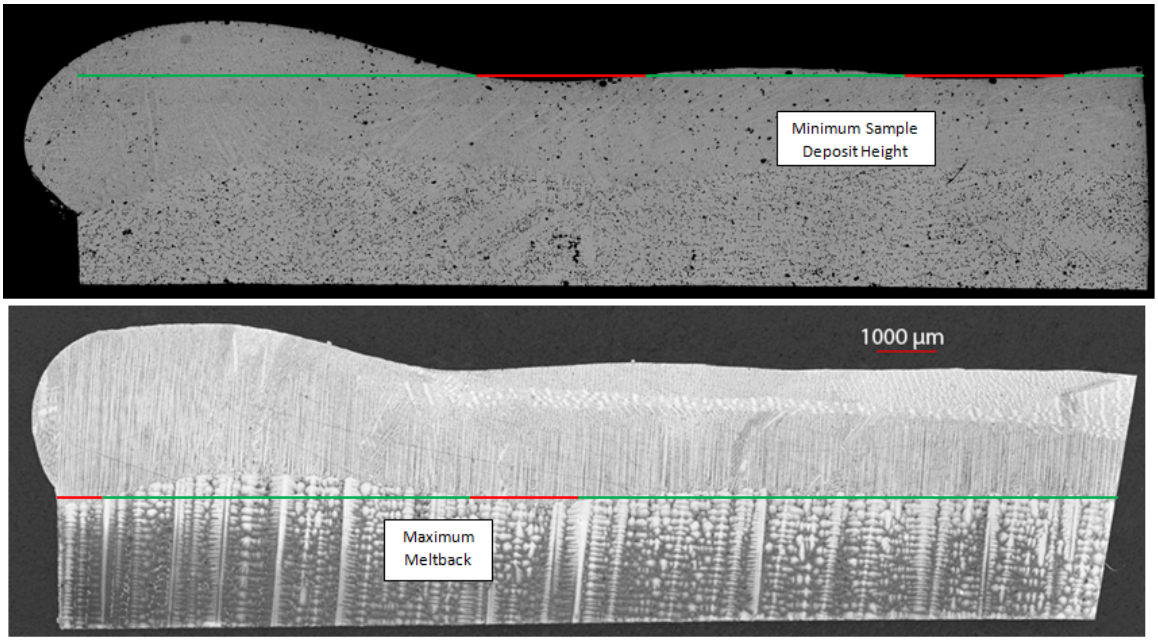

Figure 16: Top: Rene-80 sample with thresholding applied to the minimum deposit height. Bottom: CMSX-4 sample with thresholding applied to the maximum meltback depth.

a matrix containing the coordinates for every point of the meltback transition point across the sample, this can be several thousands of data points long. Having access to this information allows the analysis program to not only see how often a threshold is passed but also where it occurs and by how much. Further analysis can be done with the same information as well, such as finding the slope of the meltback line across the sample. All of these program features, and more that will be described later in the thesis, are able to be implemented due to an advanced image processing program being designed for additive manufacturing attributes and having this program being directly coupled with an analysis program.

CHAPTER III

BACKGROUND

When evaluating samples created using an additive manufacturing technique, such as SLE, the standard procedure is to consider the microstructure found along the centerline of the sample. The typical features tracked are the deposit height, pores, excessive meltback, SX orientation and lack of fusion between the cast and re-melted regions. To date, the most prevalent method of tracking these microstructural features found in Nickel-based superalloys created using additive manufacturing is visual evaluation with a set threshold. This method of evaluation leads to simple results being recorded for future consideration and does not evaluate the location along the sample where the feature in question occurs, or the magnitude of the occurrence. There are also several techniques available that are capable of measuring an individual feature found with the SLE process. A program, provided by Clemex, can track the entire crack and pore formations in a sample, outputting a list of all occurrences [14]. The well-known Electron Back Scatter Diffraction (EBSD) technique also allows for the tracking of SX orientation in CMSX-4 across an entire sample. However, this procedure requires specialized equipment, a longer turnaround time and requires still further image processing to categorize and record the information for further use.

This thesis creates a consistent technique to evaluate microstructural features previously listed in addition to several that have not been pursued, such as the primary dendrite trunk width. The entire process can be completed using digital micrographs from an optical microscope equipped with a camera. Using only digital optical micrographs, the techniques presented in this thesis can find the full scope of information

while accessing the input previously used for visual comparison. Continuous features such as the height of the deposit across the entire sample, which can be several thousand pixels long, are tracked and saved for future reference. The ease of image acquisition in addition to the advanced nature of the features being tracked gives a distinct advantage over simplistic visual comparison and more complex, and time consuming, methods such as EBSD. Each of the microstructural features is saved with no significant loss of information allowing for more advanced visualization and data fitting techniques to be employed.

3.1 Turbine Blades

Experimental gas turbine engines were developed in the early 1900s with the first patent being issued in the US in 1899 by Charles Curtis under the title "Apparatus for generating mechanical power" [15]. Over the years the power of turbine engines has increased drastically, from 4,000 kW in 1939 to values exceeding 300,000 kW in present day engines [31]. It was not until the 1920s that aircraft were being designed to incorporate a gas turbine engine in place of the traditional piston engine.

Turbine blades are critical components of gas turbine engines and with respect to this thesis, jet engines. Jet engines operate under the Brayton Cycle with three distinct stages: compression, heating, and expansion. During operation air enters the engine and is slowed in the inlet where it then flows to the compressor. Next the air enters a combustor where fuel is mixed with the high pressure air before being burned. The high temperature and high pressure byproduct then transverses the turbine, where energy is extracted to drive the compressor and other components, before finally exiting the engine through the nozzle where the engines thrust is derived [49].

Since the advent of World War II, the gas turbine has become a commonly used technology. In order to increase the efficiency of the engine and its power generation

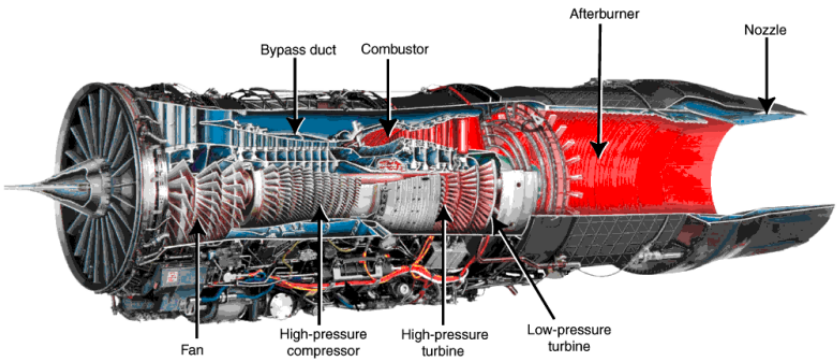

Figure 17: Cutaway of a commercial jet engine [49].

the temperature inside the combustion chamber has had to increase steadily over the years. With the operating conditions becoming more hostile, turbine blades have had to undergo various changes in materials and geometry. Several methods for cooling have been implemented, such as air channels and boundary layer cooling, so that the turbine blade material does not interact with gas that has a temperature above the metals melting point. The material has also changed over the years and is now dominated by superalloys. Nickel-based superalloys, with complex microstructure, are needed for high performance turbine engines that have temperatures exceeding 1200^oC [16].

The three typical microstructures found in Ni-based superalloys are equiaxed, directionally solidified and single crystal. Equiaxed is the least desired microstructure, but also the lowest in manufacturing cost, as it contains a large number of grain boundaries which reduces the materials ability to withstand creep at high temperatures. The directionally solidified microstructure has grain boundaries in one direction only, this allows for greater performance with fatigue and creep in the direction perpendicular to the boundaries. Single crystal microstructure, created using the Bridgman crystal growth technique, has no grain boundaries which allow it to have the greatest resistance to creep [39, 42].

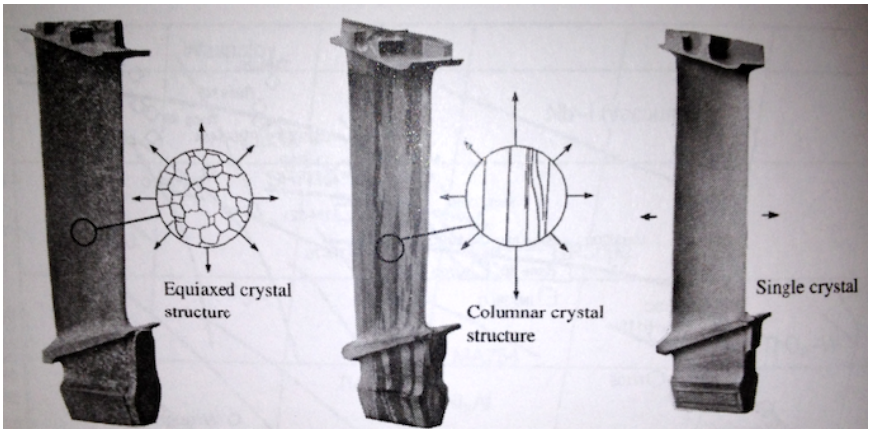

Figure 18: Equiaxed, directionally solidified and SX microstructure in turbine blades [40].

There are several types of Nickel-based superalloys including Haynes, Inconel and Mar-M but the focus of this thesis is on two specific materials: René-80 and CMSX-4. The chemical composition of the two materials is given in Table 1.

Table 1: Chemical Composition of CMSX-4 and René-80 by percent.

	C	Ni	Cr	Co	Mo	Al	B	Ti	Ta	W	Zr
CMSX-4	-	Bal	6.5	9	0.6	5.6	-	1	6.5	6	-
René® 80	0.17	60	14	9.5	4	3	0.02	5	-	4	0.03

René-80 was developed and patented by General Electric in 1971 and has an equiaxed microstructure [1]. It is a common material in industry and is found in a variety of engines. Different versions of the material exist on the market, differing by the heat treatment steps conducted [41]. The material in use with this thesis, the most common type, has undergone the full heat treatment cycle. CMSX-4 is an ultra high strength single-crystal alloy that has a peak operating temperature of 1163^oC. It was created in a joint venture between Rolls-Royce and Cannon-Muskegon to create a material with high creep resistance, good mechanical and thermal fatigue with high single- crystal yield efficiency[20]. When working with single-crystal materials, several issues can arise during processing in regards to the microstructure formation. In an ideal deposit the sample is one continuous grain, but inside of the grain are formations, called dendrites, that form during resolidification. These microstructure

formations, shown in Figure 19, must be aligned vertically when formed in turbine blades to meet the performance specifications set and the direction is referred to as orientation [001].

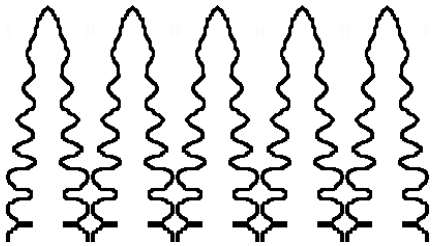

Figure 19: Primary and secondary dendrites seen in single crystal deposits.

During processing the SX deposit may have the dendrites growing in the correct orientation near the meltback line between the substrate and newly processed region but near the top of the sample it can shift. Shown in Figure 20(a) is an ideal deposit while Figure 20(b) is a more typical final product.

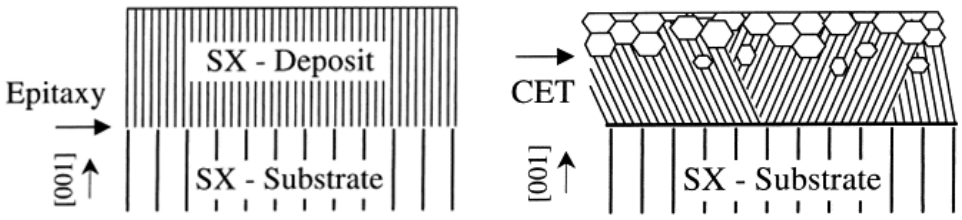

(a) Meltback transition schematic [21] (b) SX and defect regions schematic [21]

Figure 20: Meltback transition and defect region schematics.

The [001] SX deposit can be terminated in one of two ways near the top of the sample, by undergoing an oriented to misoriented transition (OMT) or a columnar to equiaxed transition. The oriented to misoriented transition, Figure 21(a), is caused by the maximum direction of the temperature gradient passing a threshold which changes the dendrite growth angle by 90^o. The transition then causes the dendrites to change direction so they can follow the progress of the laser across the sample. The columnar to equiaxed transition is found to occur near the very top of the sample and

can be seen in Figure 21(b). This is due to the amount of equiaxed grains generated in the solidifying region, related by the velocity-undercooling, passing a critical volume fraction [19, 27]. The termination of the [001] primary dendrites is an important feature of the microstructure and is detailed later in the thesis.

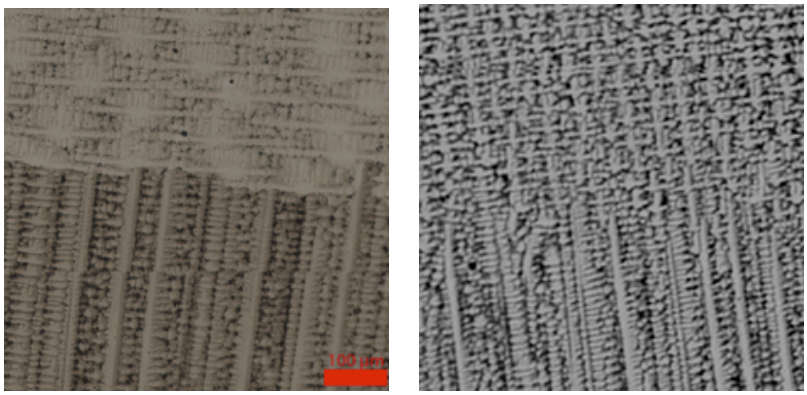

(a) Oriented to Misoriented Transition

(b) Columnar to Equiaxed Transition

Figure 21: OMT and CET as seen in CMSX-4.

3.2 Additive Manufacturing

Additive Manufacturing, otherwise known as 3-D Printing, is a class of manufacturing techniques that create three-dimensional objects through the use of an incremental layering system. Various techniques are used to work with polymers, ceramics and metals. The basis of additive manufacturing was first theorized by Blanther in 1890 [6] but did not become realized until 1972 when Mitsubishi Motors proposed the use of a photo-hardening material to be used [33, 7]. During the 1980s several advancements were made in technologies (lasers, computers and controllers) that would allow for additive manufacturing to grow significantly. Additive manufacturing with the use of metals is a more recent development in the industry and has created several types of processes such as Scanning Laser Epitaxy, Laser-Engineered Net Shaping and Electron Beam Melting [23, 3].

3.3 Image Processing

When an image undergoes any alterations or detailed analysis, the broad definition of image processing is applied. Image processing is divided into multiple subsets with the most common being low-level, shape-based and high level. Low level techniques are used to highlight and track simple geometry that is present in an image, such as line and edge detection. Shape tracking encompasses blob extraction and thresholding. Finally high-level image processing refers to computer vision, where information is analyzed, extracted and put to further use. While there are dozens of image processing techniques only the few utilized by this thesis will be explained in detail.

Two types of mathematical morphologies that have been put to use with grayscale images are dilation and erosion. Both morphologies utilize a structuring element, titled $b(x)$, that signifies the area of interest for each point analysed. It is commonly square or rectangular in size but can also be shaped as a cross. For dilation each point in an image is compared to the surrounding pixels in the structuring element and takes on the value of the pixel with the largest magnitude found in the structuring element [25].

$$(f \oplus b)(x) = sup_{y \in E}[f(y) + b(y - x)] \tag{1}$$

Figure 22(b) shows the change in a cell value due to the use of dilation. The red shaded block is the cell under current analysis while the blue shaded blocks are within the area of interest, the kernel. All other blocks, shaded white, are not considered for the current cell.

Erosion follows the same procedure as dilation except the infimum is found in the structuring element as described in Equation 2. Figure 23(b) shows the change of the selected, red, cell to the lowest value of the cells found within the blue structuring element [25]. Instead of altering the cell to become equal to its closest maximum, it now follows the minimum value.

6	2	1	2	7
4	6	5	3	3
2	3	5	2	1
8	3	7	8	5
5	6	4	2	9

(a) Cell value before dilation is performed

6	2	1	2	7
4	6	5	3	3
2	3	8	2	1
8	3	7	8	5
5	6	4	2	9

(b) Cell value after dilation is performed

Figure 22: Cell value alteration due to dilation.

$$(f \ominus b)(x) = inf_{y \in E}[f(y) - b(y - x)] \tag{2}$$

6	2	1	2	7
4	6	5	3	3
2	3	5	2	1
8	3	7	8	5
5	6	4	2	9

(a) Cell value before erosion is performed

6	2	1	2	7
4	6	5	3	3
2	3	2	2	1
8	3	7	8	5
5	6	4	2	9

(b) Cell value after erosion is performed

Figure 23: Cell value alteration due to erosion.

When dilation and erosion are used one after the other the procedure is titled opening or closing, depending on which operation is performed first. Opening is the dilation of the erosion of the function by the structuring element b. The opening operation is used primarily to remove upward outliers in an image. Figure 24 shows the two steps used to open an image using a kernel that considers only the point immediately before and after the primary point. The end result maintains the images overall original form but removes the excessive values and in doing so many lone outliers can be discarded. This function is able to provide a means to better clean an image of small, but high valued, noise. This process is commonly referred to as cleaning 'salt' from an image.

Figure 24: Opening of a data set using erosion then dilation [9]

The closing operation is performed by dilating then eroding an image. Figure 25 shows how the procedure removes low valued outliers and in doing to connects regions in the image. This process is used to remove low valued noise from a system, called 'pepper' noise, which provides a cleared resulting image. It is also commonly used to join areas in close promimity while still maintaining the same global structure. Finally this process will mitigate holes in a large volume.

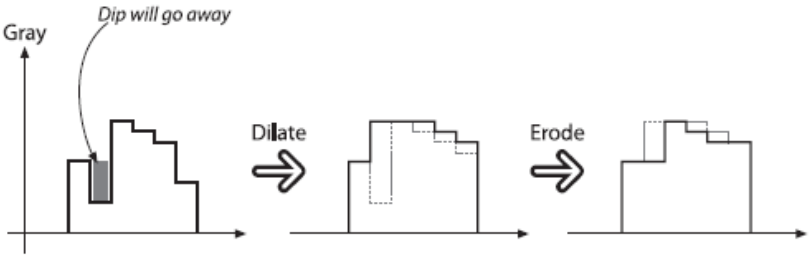

Figure 25: Closing of a data set using dilation then erosion [9]

Canny Edge Detection is a subset of edge detection where the primary purpose is to preserve important structural data while filtering out a vast majority of the images information. Canny edge detection, also known as optimal edge detection, has three fundamental goals. The first is to minimize the error at each point so that no edge is missed in the analysis and that a non-edge is not falsely tracked. The second goal is to provide good localization, minimizing the distance between where the edge is tracked in the analysis and the actual edge location on the image. The third goal is to

respond to each edge only once. The results of Canny edge detection can be viewed in Figure 26(b). It was able to successfully collect all of the major, and many minor, edges that are shown in the image and outputting them as single lines that allow for easy further analysis.

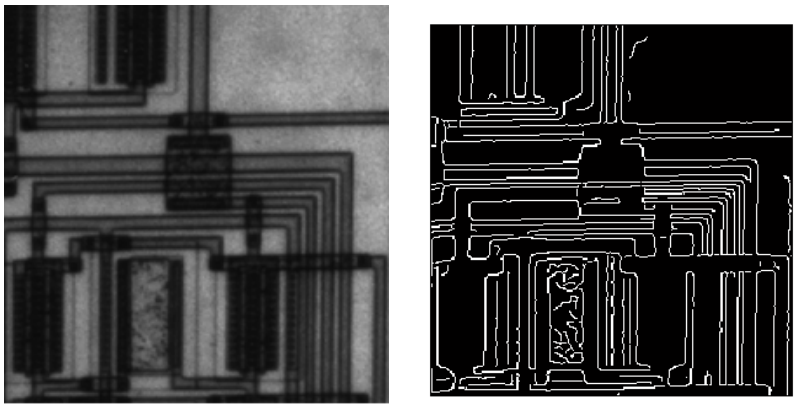

(a) (b)

Figure 26: Image before and after Canny edge detection

The first step in Canny edge detection is to reduce the amount of noise in the image, thereby reducing the chance of a false positive. A Gaussian filter is applied to the image resulting in a slightly blurred output where small noise has been reduced. Next the image has its first derivative taken in up to four directions; vertical, horizontal and at different angles. This directional information is saved for the next step of edge tracing. The edge detection has two steps utilizing dual thresholding with hysteresis. First a high threshold is used to find lines with large gradients while ignoring lines with low gradients and individual pixels with high gradients. Next the lower threshold is used to find lines with weaker gradients in the image while taking into account the information found in the prior step, a hysteresis analysis. Only weak lines with a starting point originating along a strong edge are tracked and saved.

This method is used to gather a large amount of edge information in the image which can then be further analyzed to provide clear data. Only the maxima values found are used as the Canny method searches for steps in a single direction, allowing

a feature to be counted only once [12, 32].

Active contours are splines that move due to external energies being applied to them though a map, usually associated with an image, while maintaining a shape through the use of an internal energy. The total energy of the snake line is given in equation 3 [28, 29, 5].

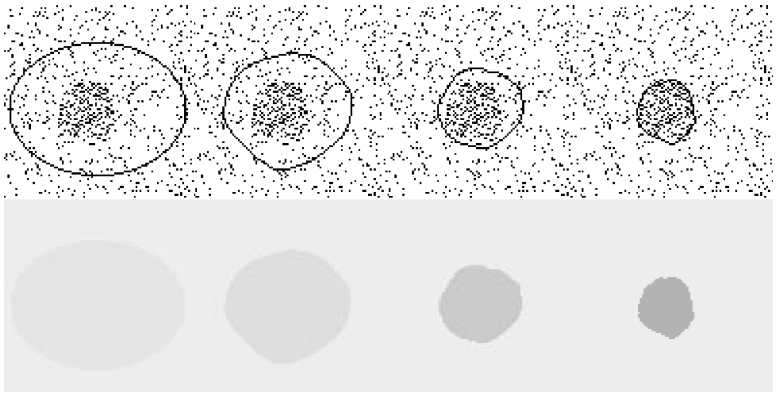

Figure 27: Closed loop active contouring applied to noisy data [13]

$$E_{snake} = \int_0^1 (E_{int} + E_{image} + E_{con})ds \tag{3}$$

E_{int} is the internal energy in the spline and is used to hold its shape. E_{image} is the force being applied to the spline from the image in question while E_{con} is used to exhibit constraints on the contour. The internal spline energy E_{int} is expressed in Equation 4, where the first order term makes the contour act as a membrane and the second order term makes it act as a thin plate [28].

$$E_{int} = (\alpha(s)|v_s|^2 + \beta(s)|v_{ss}(s)|^2)/2 \tag{4}$$

The image force, as seen in equation 5, controls how the active contour will react to lines, edges and terminations. The E_{line} term is the intensity from the original image, in this case a filtered image of the Canny output. The edge function attracts the contour to large image gradients and is given in equation 6. The termination

energy allows the contour to be attracted to corners of the image and is disregarded when finding the meltback depth as the corners of the image are already known. Of these three terms the primary force being exerted on the spline is the E_{line} term, which applies a downward force onto each spline knot. This pushes the spline away from the original top of the substrate towards the meltback transition. The edge term is also used, though in a smaller capacity, to help the spline adhere itself to the ends of the Canny-found lines that mark the meltback transition.

$$E_{image} = w_{line}E_{line} + w_{edge}E_{edge} + w_{term}E_{term} \tag{5}$$

$$E_{edge} = -|\nabla I(x, y)|^2 \tag{6}$$

The constraint energy E_{con} allows for external forces outside the scope of the image to be applied to the contour. A small external force is used which pushes the points upward, though this force is insignificant compared to the E_{line} energy. The spline will move downward until it passes the point of the newly formed single crystal region, where the E_{line} term approaches zero, it is at this point that the external and edge forces will be strong enough to form the line along the underside of the single crystal growth.

3.4 Design of Experiments

Design of Experiments have been commonly used in industry starting in the 1920s when first proposed by Ronald Fisher [48]. The main purpose behind a DOE is to minimize the number of experiments while maximizing the amount of data obtained.

Design of experiments are used to find the relation between a set of parameters and an output of the operation, in this case the resulting microstructure. A simple DOE will typically address linear effects of the parameters, power or scan speed, and combinational effects, (power)x(scan speed). If a DOE is simplified, the reasoning

behind this action is explained later in the section, the amount of information is reduced and confounding can occur. Confounding is when a relations effect on the outcome cannot be differentiated from another effect. If the power level is confounded with the scan speed then it is not possible to determine if a change in the outcome is a result of one or the other. This can be problematic if the linear order effects are confounded with each other. To minimize this issue, DOE designs tend to make any confounding that occurs be between higher level combinations, or at worse have a linear effect confounded with a higher level combination with the assumption that the higher level combination effect is nearly zero.

There are typically three stages involved with performing a series of DOEs to isolate the optimal operating parameters; screening, ascent and response experiments. Screening, or a phase zero DOE, is used to isolate parameters that hold the greatest significance for the process. By isolating the most important settings and focusing only on those for phase one and two the number of total experiments is greatly reduced. Phase one, ascent, is a broad search of the parameter optimizing range with the goal being to roughly locate the optimal area. Once the optimal parameter area is found a response surface DOE, phase two, is undertaken to more accurately map the region of interest [35]. The clear distinction of each phase is put in place to better conserve the number of experiments performed.

This thesis primarily works with a phase one design of experiment but does have some focus on phase two. When performing a phase one DOE the primary purpose is to use the method of steepest ascent to locate the area of optimal parameter settings. To accomplish this goal, while minimizing the total number of experiments, a factorial style analysis is iterated until the optimal region is recognized. Factorial experiments utilize discrete values for each parameter to simplify each experimental setting; this can be as simple as having a setting as either on or off, to discretizing a continuous setting with a set interval over a typical operating range. A full factorial DOE will

run through every level for every setting and is most easily visualized with three two level factors as shown in Figure 28.

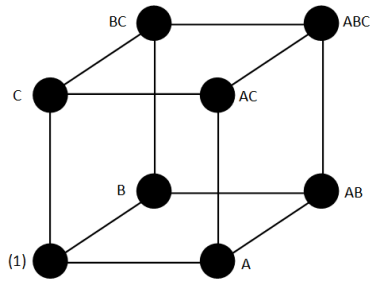

Figure 28: A full 2^3 factorial DOE

Performing a full factorial DOE becomes unnecessarily large as the number of settings and levels per settings increases, leading to the development of a fractional factorial design. Fractional factorial DOEs lower the number of experiments while sacrificing some level of confidence by using a carefully chosen subset of the full factorial design.

A direct comparison between a full factorial and fractional factorial design will best show the contrast between the two. For an experiment involving three factors each with two levels the number of experiments involved with a full factorial DOE would be 8 and is denoted by 2^3. This DOE would measure eight effects: the grand average, three main effects, three two-factor interactions and one three factor interaction. Instead of performing eight experiments a half fractional factorial design could be used, denoted by $2^{(3-1)}$ where four experiments would be needed. The tradeoff for lowering the number of experiments is through confounding effects. By carefully choosing which points to use in the fractional factorial DOE the confounding can be mitigated. In a $2^{(3-1)}$ DOE the main effects are each confounded with a two factor interaction.

The level of confounding for each fractional factorial DOE is described with a Resolution Type. There are three resolution levels that are most commonly used in

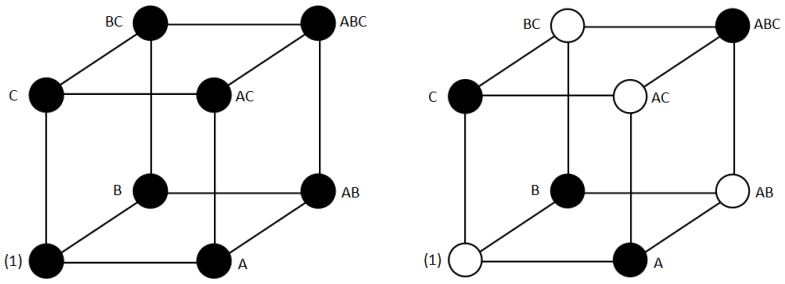

(a) 2^3 full factorial (b) $2^{(3-1)}$ fractional factorial

Figure 29: Two factorial DOEs for three parameters with two levels each

fractional factorial creation, named Resolution III, IV and V.

Resolution III: No main effect is confounded with any other main effect but a main effect is confounded with two-factor interactions. The 2^{3-1} fractional factorial is Resolution III.

Resolution IV: No main effect is confounded with any other main effect or any two-factor interaction. Main effects will be confounded with three-factor interactions while each two-factor interaction will be confounded with other two-factor interactions. The 2^{4-1} fractional factorial is Resolution IV.

Resolution V: No main effect or two-factor interactions are confounded with other main effects or two-factor interactions. The 2^{5-1} fractional factorial is Resolution V [8].

Once the optimal parameter range is isolated, the final step in a DOE procedure is to perform a response surface DOE. The response surface methodology provides greater insight into how a parameter can influence the result, at the cost of several additional experimental trials. There are several types of RSM Designs with one being a central composite design, Figure 30. This DOE has three main aspects to it, the first being a two level full factorial for the given number of parameters, in the Figure this is three. There is also a center point contained within the full factorial design. Finally there are axial points that extend beyond the limits of the factorial DOE along the axis of a single parameter.

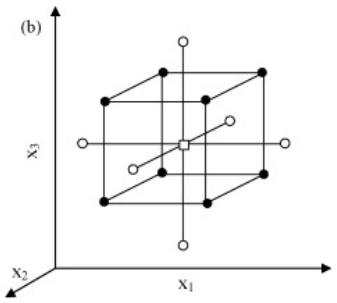

Figure 30: A central composite design RSM for three variables [4].

3.5 Data Fitting

The goal of data fitting is to relate a set of parameters to a single output. During data fitting the equation that will be used to describe the relation between the response and the parameters must be formulated. Once the equation has been decided; be it linear, quadratic, cubic or some other combination, the parameter data must be tabulated to correspond with the associated equation and for further reference will be labeled as matrix X. Once X is prepared a least squares estimate for the coefficients of the equation can be found using Equation 7.

$$b = (X'X)^{-1} * X' * y \tag{7}$$

The equation returns a vector, b, that holds all of the coefficient terms for the equation in question. The next step is to determine the unbiased error, which takes into account the equation complexity and number of samples. The unbiased error associated with the estimated coefficients b can then be calculated by first finding the Sum of Squares Error as shown.

$$SS_e = y'yb'X'y \tag{8}$$

Using the SS_e value along with the number of parameters in the equation found, denoted by variable p, and the number of observations, called n, the unbiased error can

be calculated. This allows for different equations, with different p values depending on the equations complexity, to be compared for the amount of error associated with the coefficient estimation.

$$\sigma^2 = \frac{SS_e}{n-p} \tag{9}$$

For each least squares analysis run, the coefficients found can be individually analyzed to find their level of importance relative to the whole equation, Equation 10. If the absolute value for a coefficient, its t_o value, is greater than the t_{test} value, found using a list with the number of parameters and desired accuracy, then it has a high significance to the equation. Coefficients that fall below this threshold may be removed from the data fitting equation to improve the accuracy and increase the certainty.

$$t_o = \frac{b_j}{\sqrt{\sigma^2((X'X)^{-1})_{jj}}} \tag{10}$$

It is common for statistical programs to use a t-chart to show the different t_o values and how they compare to the t_{test} threshold value found. Figure 31 shows a typical t-test with six parameters being listed. The t_o value for each parameter is the blue bar while the two red lines are the positive and negative t_{test} value. The figure shows that power, repeats, power times repeats and scan speed times repeats all pass the test. The removal of the additional two parameters that failed the test could lead to more accurate results. Typically not all parameters under the testing threshold are removed, only the lowest valued are taken out of the equation.

Once a data equation is fully formed it is tested for its level of certainty in predicting the actual effects. Using the Sum of Squares Regression and Error values, shown below, the F_o value can be found using Equation 13, titled an F-test. The F_o value is then compared with an F_{test} value obtained from a chart using the number of samples and degree of desired certainty. If the F_o value is greater than the F value,

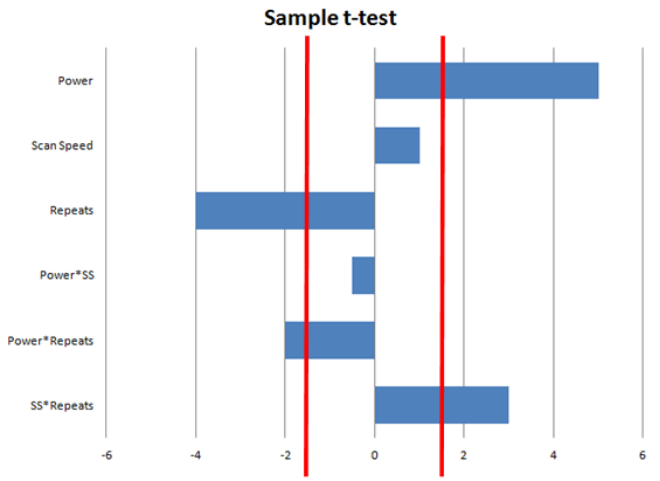

Figure 31: T-test performed on six parameters.

the equation is significant. The comparison style is similar to the t-test described above only taken for an entire equation instead of a single variable.

$$SS_R = b'X'y - \frac{(\sum_{i=1}^{n} y_i)^2}{n} \tag{11}$$

$$SS_E = y'yb'X'y \tag{12}$$

$$F_o = \frac{SS_R/(p-1)}{SS_E/(np)} \tag{13}$$

To better visualize the information, each data fitting equation is used to predict points within the maximum allowable operating range of the SLE process. For each point in a grid covering all four parameters the SLE settings are multiplied into the data fitting equation with the corresponding output being saved to matrix. Figure 32 shows a 2-D cut as a contour plot.

For each point it is also important to know the amount of uncertainty in the prediction. Using the t-test value, found in a chart for the desired accuracy and the degrees of freedom, the point in question and the sigma squared value; the uncertainty

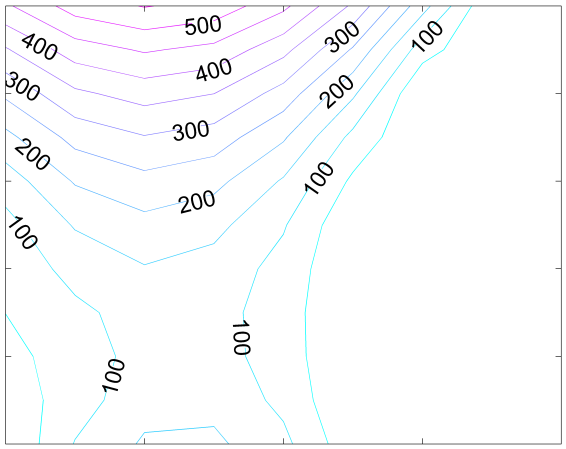

Figure 32: Contour plot showing predicted values from a data fitting equation.

can be predicted at each point. A contour plot can also be shown for the uncertainty of each point, giving some weight into the findings from the predictions.

$$uncertainty = t\sqrt{\sigma^2 x'(X'X)^{-1}x} \tag{14}$$

CHAPTER IV

METHOD

4.1 Experimental Procedure

SLE can be used to process a variety of superalloys commonly used in the aerospace industry. Each material requires a different amount of laser power, scanning speed and repeated scans to create the desired microstructure, which results in a large number of experimental runs to isolate the best settings. Due to the high cost associated with the material and components, a set of experiments are performed using several simplifications to recreate the conditions of the worn turbine blade while mitigating the cost.

During the initial testing phase of a new alloy, the geometry is simplified from a complex shape to a like-sized rectangular coupon that is 1.25 inches long by 0.27 inches wide by 0.1 inches thick, made from the same material as the turbine blade. This allows for lower cost sample creation, simplified conditions and faster processing. As the optimal operating parameters are better recognized the geometry will be altered to a more turbine blade-like design through two steps as shown in Figure 33. After the rectangular deposits are completed wave deposits are made on rectangular coupons. Next airfoil like designs are created on rectangular coupons and on airfoil shaped coupons.

Since turbine blades are much larger than the sample coupons a heat sink is needed that can correctly simulate the heat transfer that will occur when an actual blade is being repaired. An Inconel 625 baseplate was designed to contain five evenly spaced coupons. Within each well where the coupons rest, there is a through-hole that simulates the hollow space below the tip cap of a typical internally-cooled turbine

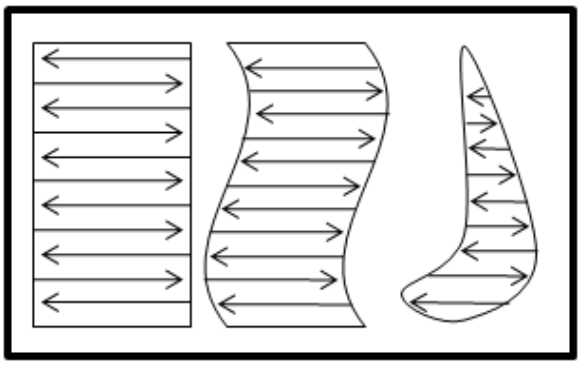

Figure 33: Raster scan complexity steps.

blade, creating a more realistic heat distribution during processing.

For each experiment, the sample coupons are first thoroughly cleaned to remove any possible contaminants from the process. They are then carefully set within insets located in the Inconel 625 baseplate. A containment vessel is then placed over the sample and fitted to the baseplate to hold the powder to a desired height. Using previously measured packing densities for each different powder, a precise amount of the powder being used is weighed and then metered into each cavity so that it may spread evenly. This procedure is shown in Figure 34, with the rightmost cavities left empty, the middle cavity holding the sample and the leftmost cavity holding the sample and powder.

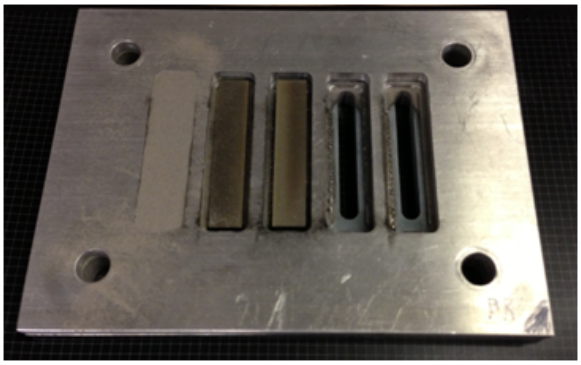

Figure 34: Sample preparation displayed in three steps.

Each baseplate can hold up to five samples and there are a total of four baseplates available for the current experimental coupons, providing up to twenty samples that

can be tested in one operation. Each baseplate is screwed onto a different aluminum breadboard measuring ten inches square with each board having inserts that allows them to be placed on a rail system. The samples are placed within a controlled-atmosphere process chamber, where they are inserted into a rail made from 80/20 extruded aluminum. The chamber is then purged with inert gas for processing. Once a full set of five samples on a baseplate are processed, the next breadboard can be moved into place along the rail to the exact operating location. During processing a 1kW Fiber Laser is used in conjunction with a galvonometer scanner as shown in Figure 35(b) to establish and progress the meltpool across a sample.

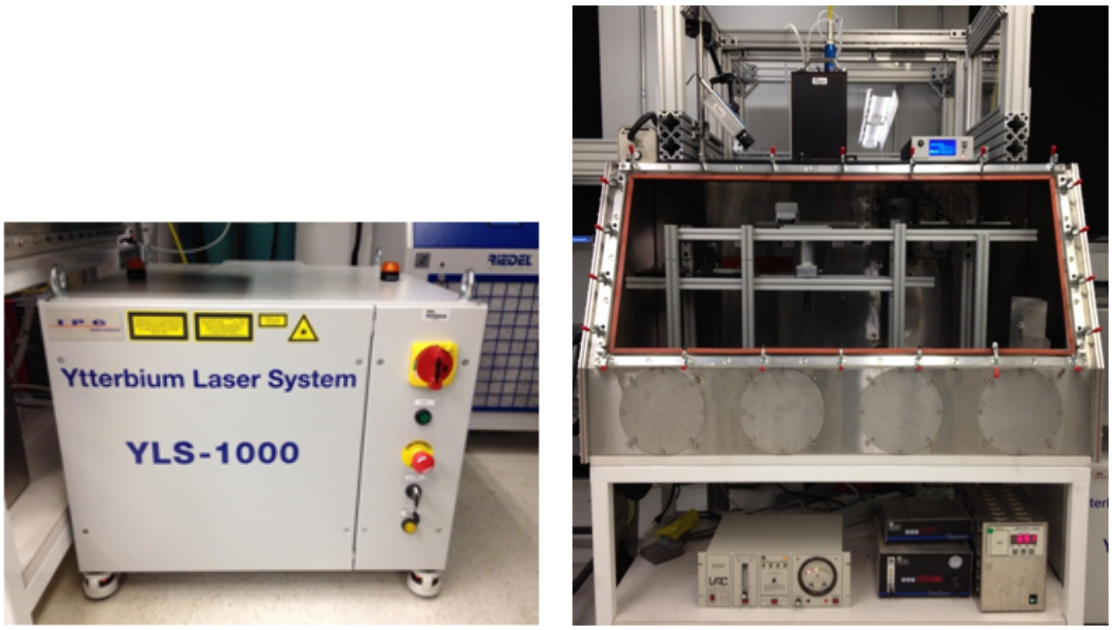

(a) Fiber Laser (b) Processing Chamber

Figure 35: SLE Equipment

During operation three instruments are used to collect data: a thermal imaging camera, video microscope and machine vision camera. The instruments mounted on the atmospheric chamber are shown in Figure 36. The thermal imaging camera is used to measure the temperature field of a sample during operation. This information is being used by another member of the group to provide data so that real-time control can be used to maintain a desired temperature field that will result in a desirable

microstructure. The video microscope allows a realtime view of the operation and can help with inspection after a run is concluded. The machine vision camera provides a clear view of the sample as it is being processed with no interference from the laser or ambient lighting. Machine vision cameras work by utilizing a high powered strobe light to shine light onto the sample at a specific frequency. The camera then collects information for only those instances, and combined with a filter to remove the wavelength most commonly associated with the laser, a clear image can be formed. The machine vision camera allows for the meltpool to be most readily observed and can even give insight into how the unprocessed powder is fed into it.

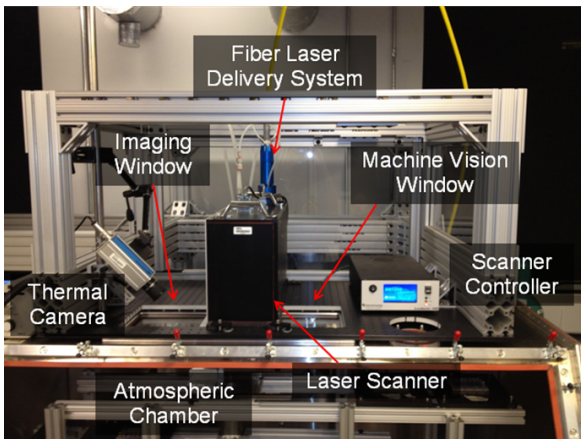

Figure 36: Overview of the equipment used in the SLE process.

Once a group of samples has been processed, several steps are taken so that they may be imaged for later analysis. First a sample is cut using a Buehler Table Saw lengthwise through the center width, marked as A on Figure 37. One half of the sample is kept for later imaging while the other is cut widthwise at several instances along the length of the sample. The lengthwise cut gives insight into how the process changes during operation while the widthwise cuts give information on how the meltpool and the deposit react near the edges of a sample. While both types of cuts are important, the sole focus of this thesis revolves around the lengthwise cuts for the samples.

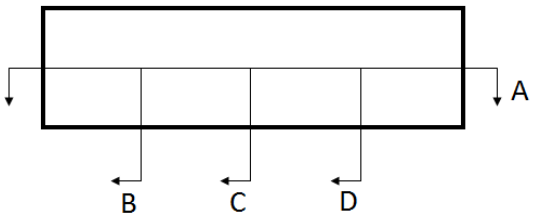

Figure 37: Locations where coupon samples are cut for analysis.

Each sample is mounted in Bakelite using a Beuhler press so that the cut section is visible. Next the sample is sanded flat using several steps with increasing grit sandpaper. Once sanded smooth, the sample is polished first using a 9 micron diamond polish suspension, then a 3 micron diamond polish suspension before finally undergoing a final polish with an silica slurry.

Once polished the sample is imaged under a Leica Microscope at 100 magnification. Using a moving stage, dozens of images are taken by the microscope and stitched together to create one seamless image. Each image for a lengthwise cut of a sample is typically 500 MB large with the size being in the vicinity of 7000 pixels high by 15000 pixels long. The size of the image allows the viewer to have the ability to view the sample at a macro level while retaining the ability to zoom in for viewing finer features. These images, which can be created within a day of the sample being created, are used as the sole visual input for every microstructure detection program described in the thesis.

4.2 Microstructure Detection

Tracking the various microstructure features requires several functions, each designed to isolate a specific characteristic found in the micrograph. Shown in Figure 38 are the steps taken to track each microstructure feature, shown as red ovals, for CSMX-4 and René-80 samples.

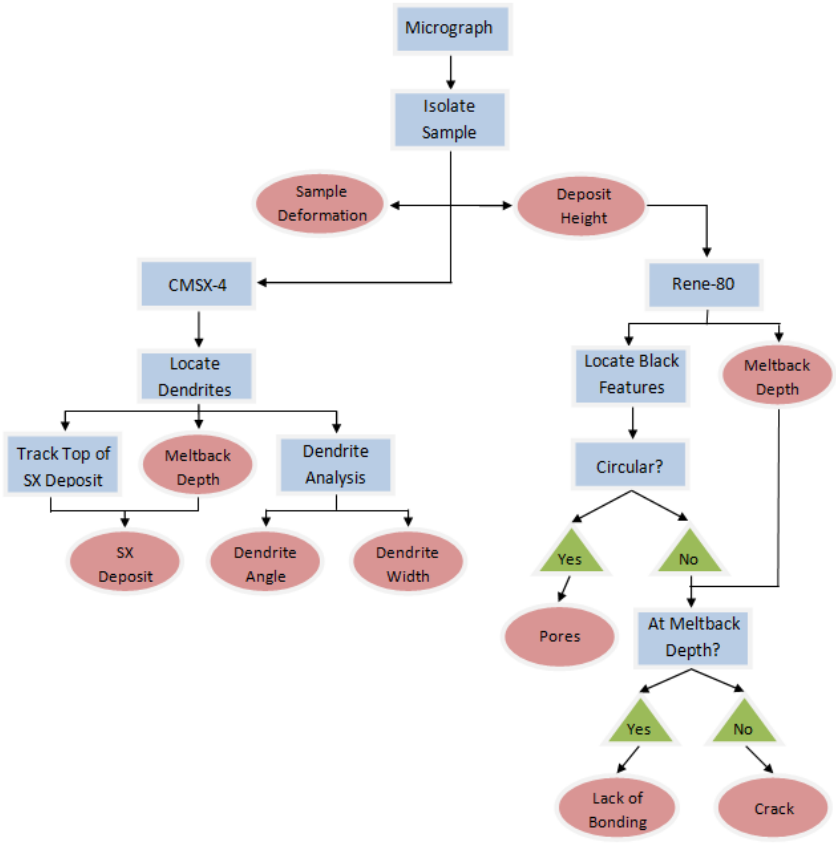

Figure 38: Microstructure Feature Recognition Diagram.

4.2.1 Sample Isolation

For every image to be analyzed in the microstructure detection program, be it René-80 or CMSX-4, the sample must be isolated. The first step taken to accomplishing this goal is to investigate the Bakelite deposit found around the sample. A basic assumption is made that the image will never have the bottom left corner of the sample be within fifty pixels of the bottom-left corner of the image. For most cases this must be true as the deposit extends beyond the substrate at the beginning of the scan, which is shown on the left size of the image. For all future image capturing this will be held as a rule of operation. The bottom-left corner of the image is analyzed 50 pixels high and wide to find the average intensity value of the Bakelite material. This number is now associated with the Bakelite level for all future investigations.

In every image taken, the Bakelite value is vastly different from the actual samples intensity values which provides a clear contrast and allows the sample to be isolated with relative ease. The need to investigate the Bakelite for each sample is due to the possibility that the Leica Microscopes settings have been adjusted, creating a fundamentally different Bakelite average intensity value.

Once the intensity is known, five active contouring steps are completed to isolate the sample along the bottom, top, left and right sides. First an active contour is generated along the bottom of the image along the entire length of the image. The contour is then pushed upwards by an in built force. The only external force acting on the contour is the image's intensity values minus the Bakelite average intensity. This allows the contour to move upwards from the bottom of the sample to the base of the substrate with little interference. Once the contour points begin intersecting with the sample the contour will begin to follow the base of the substrate. When iterating the contour the inner eighty percent of the line is compared to its last iteration locations. Once the inner eighty percent of the contour stabilizes at a constant location the iterating of the active contour is stopped. Only eighty percent of the contour is considered as the edges of the contour at either extreme of the image may take much longer to adhere to the sample and provide little to no relevance to the bottom of the sample.

The completed contour is searched for corner locations, seen by rapid vertical location changes between different points, to be used when searching for the left and right sides of the image. As shown in Figure 39 the first major step in the active contour previously found, denoting a corner, is used as the lowest section when generating a contour to find the left side of the sample. The left and right edges are found using a similar procedure as explained for the bottom edge. Once the two sides have been tracked the bottom-left corner and bottom-right corner of the image can be more accurately described.

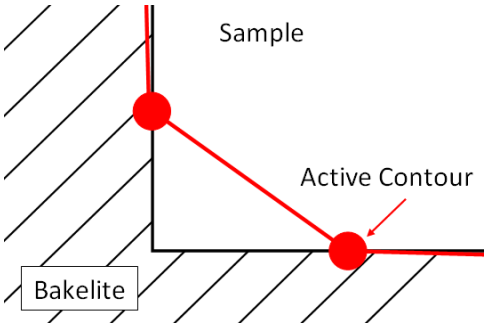

Figure 39: Closeup view of the active contour near the sample edge.

A second active contour is then run along the bottom of the sample within the bounds of the left and right bottom corners of the sample to isolate the bottom of the substrate. The same procedure is used to find the top of the sample by creating a contour along the top of the image and propagating it downward. The top and bottom sample lines are saved for later analysis: the top line denotes the total deposit height, shown in Figure 40, while the bottom line gives the sample deformation, shown in Figure 41.

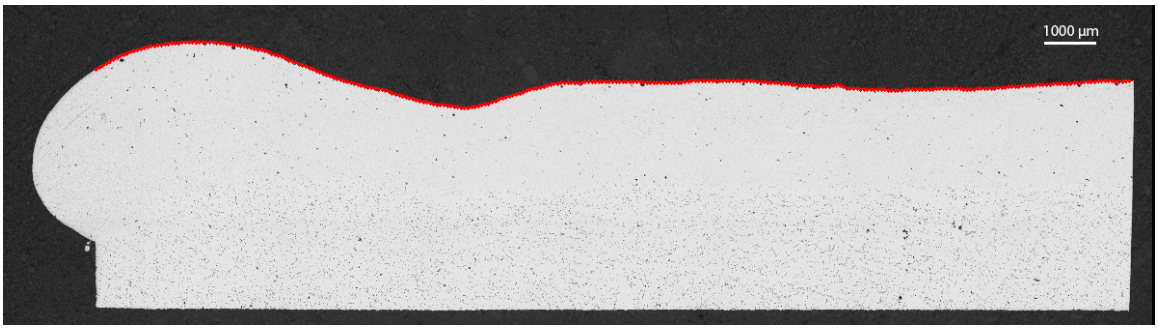

Figure 40: Tracked top of a sample overlayed with the image.

The bottom line, Figure 41, is used to understand the amount of deformation that the sample may have undergone. By looking at the change in angle of the sample across the entire sample length it is possible to see whether any warping occurred due to excessive energy being introduced to the system. The bottom line must also be accurately tracked as it is the sole way to determine the location of the original substrate height. Since the meltpool extends into the substrate by a varying amount

there is no visible way to determine where the substrate to powder transition point was prior to running the experiment. Using the bottom line, the thickness of the substrate and the known number of pixels per meter in the image it is possible to offset the bottom line the correct amount and show the original substrate location.

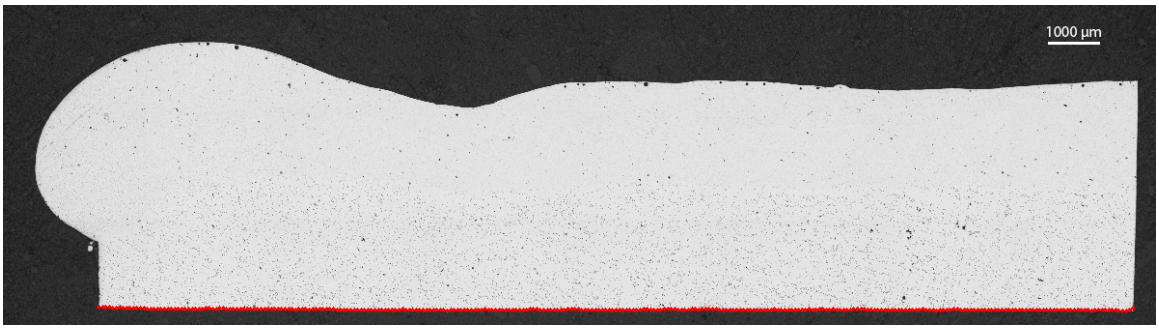

Figure 41: Tracked bottom of a sample overlayed with the image.

4.2.2 Basic [001] SX Dendrite Tracking in CMSX-4

When a dendrite is formed in a single-crystal region, there are two easily visible features, titled primary and secondary dendrite growths, that are shown in Figure 42. The primary growth acts like the trunk of a tree, it is a long vertical extension that forms in the direction of highest temperature gradient during solidification. The designation [001] indicates that these primary dendrite growths are vertically directed, the only acceptable orientation for single-crystal turbine blades. The secondary dendrite growths are shorter offshoots from the primary trunk and can be viewed as branches of a tree. The width between two secondary dendrite arms is related to the cooling rate of the metal during solidification and the thermal gradient [46]. The secondary dendrite arms are not a focus of this thesis but are described during the Future Works section as a possible area for future analysis.

In order to isolate the primary growths, the microstructure recognition program must not be overly influenced by the secondary dendrites. To accomplish this, the microstructure image is first differentiated in the x-direction to highlight intensity

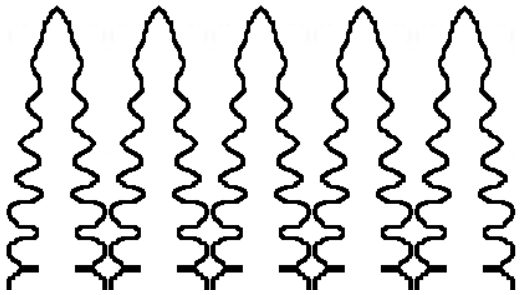

Figure 42: Primary and secondary dendrites seen in single crystal deposits.

changes that are most prevalent surrounding both sides of the single-crystal primary dendrite. This image is then processed when searching for edges utilizing the Canny edge detection algorithm. As stated in Chapter 4, the Canny edge detection finds major edges and minor edges that are linked with a major edge. This type of edge detection is necessary due to the primary and secondary dendrites complexity. Finding only major edges along the image results in segments along the outer section of the secondary growths and segments along the primary dendrite trunks. By allowing weaker edges these sections can be joined at locations and allows for a greater representation of the image to be found.

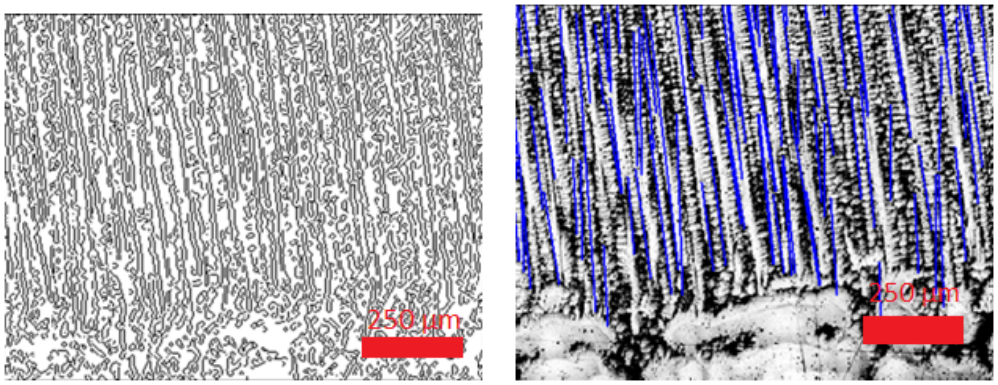

(a) Canny detection output

(b) Edges of dendrites found from Canny output

Figure 43: Canny edge detection and superimposed dendrite lines.

The Canny Edge Detection Algorithm returns an image with thousands of lines as can be viewed in Figure 43(a). A search must be conducted to find lines over a specific threshold that denotes a long vertical growth, a primary dendrite. The

searching method uses two maps, the Canny output and a hysteresis map. The hysteresis map marks any pixel that has already been searched and will not allow the searching algorithm to track across that location a second time. The searching algorithm runs through every pixel of the Canny output, starting at the top left corner of the image, until it finds a positive pixel value that indicates an edge. A separate function is used to track the line until completion. When searching for [001] SX lines the search is limited to 45 degrees from the vertical so that the more horizontal lines are not traced. A common occurrence when tracking a Canny line is branching. This is the key feature of Canny edge detection as it allows minor lines to be tracked as long as they intersect with a major line on the image. To efficiently track each branch for a given line, the searching algorithm tracks the split locations. The algorithm will follow the leftmost branch of the sample until its end then progress through each split back towards to top. Each line traced has both its beginning and ending points saved for later use while a starting point containing several branches will find a weighted ending point that best represents all of the splits.

Every significant line found is to be highlighted and tracked throughout the image. The lines found tend towards the left side of the dendrites and typically do not extend throughout the entire dendrite length but by utilizing a large number of tracked lines a general consensus for every region of the columnar growths can be found. Figure 43(b) shows the tracked single crystal growths for the region given in Figure 43(a). The blue lines are dendrite growths found using the canny edge detection and the searching algorithm. Each lines starting and ending point are saved for later analysis.

4.2.3 CMSX-4 Meltback Depth Tracking

The first step in tracking the meltback depth in CMSX-4 is to create a heat map based off of the dendrite edge data so that the transition point between the fine dendrites and the coarse dendrites can be accurately found. Each line found during the prior Canny

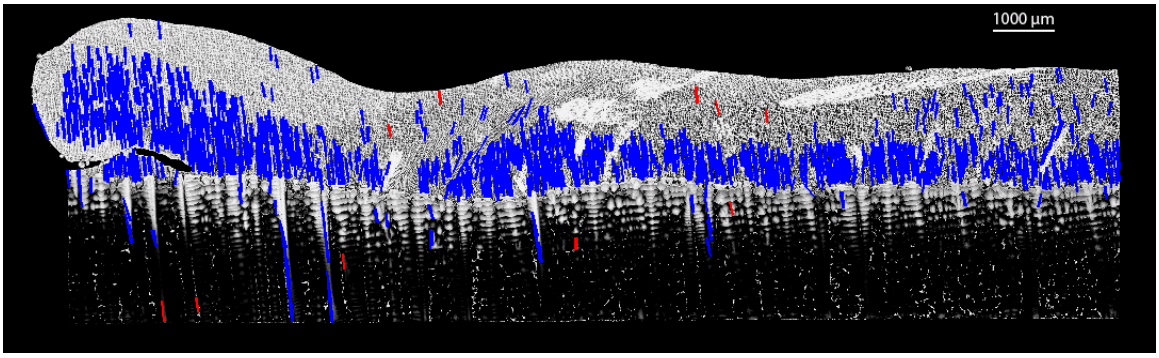

Figure 44: Tracked line for a CMSX-4 sample using Canny edge detection.

edge detection step is saved using only the beginning and final points. Bresenhams line algorithm is used to accurately recreate a straight line using the initial and final points saved during the Canny step. The line algorithm, demonstrated in Figure 45, uses the slope found between the two points to track the amount of error being built as the line progresses in a specified direction. When the program is recreating a shallow line every step will accumulate an error as described in Equation 15.

$$e = \frac{dy}{dx} \tag{15}$$

Starting from the initial position described in the Canny step each pixel being created will progress in the x direction, $x_{i+1} = x_i + 1$. A total error will also be updated as shown in Equation 16. Once the error passes a threshold of 0.5 the y coordinate of the next point generated will increase by one, $y_{i+1} = y_i + 1$. The total error will then have one subtracted from its value.

$$E_{i+1} = E_i + e \tag{16}$$

This same procedure is used for steep lines, only with the error term being inverted and with the y-value of the newly created points always being the direction incremented. Using this procedure the line can be created using minimal computation time and recreates a close approximation to the original straight line [18]. A separate

function was created that allows for the line to be quickly found at any orientation so that it may be called on in later programs.

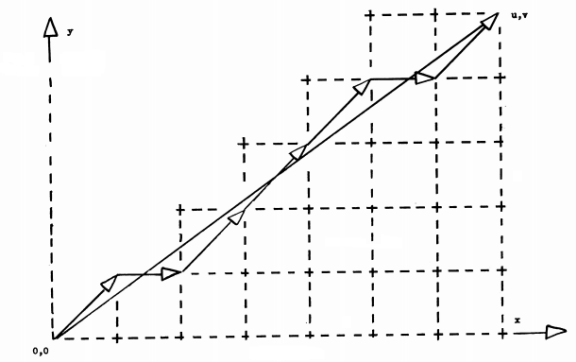

Figure 45: Overview of Bresenhams line algorithm [38].

As the program is recreating each line a weight is added for the surrounding pixels. For each newly generated pixel created with the Bresenthal's Algorithm the pixels located to the left and right, for a steep line, are increased in value on the heat map. The new intensity value for a pixel is determined using Equation 17, with σ being the distance from the pixel in question to the Bresenthal's pixel that was just created.

$$I(x, y) = I(x, y) + \frac{1}{\sigma} \tag{17}$$

Starting at an intensity value of one for the actual line, the intensity is reduced in direct proportion to the distance the pixel is located to the line. This weighing extends ten pixels outside of the line and allows for gaps between each thin dendrite to be partially filled. This is needed to allow the lines to better represent an entire area of the sample so that an active contour can later be used to track the meltback depth. A small amount of weighting is also added to both the top and bottom of each line. The additional force allows for an active contour to better conform to the edge of the single crystal area than it would if the intensity changes form a near zero value, indicating no single crystal, to a high value.

Once each line is recreated on the heat map the active contour function is called.

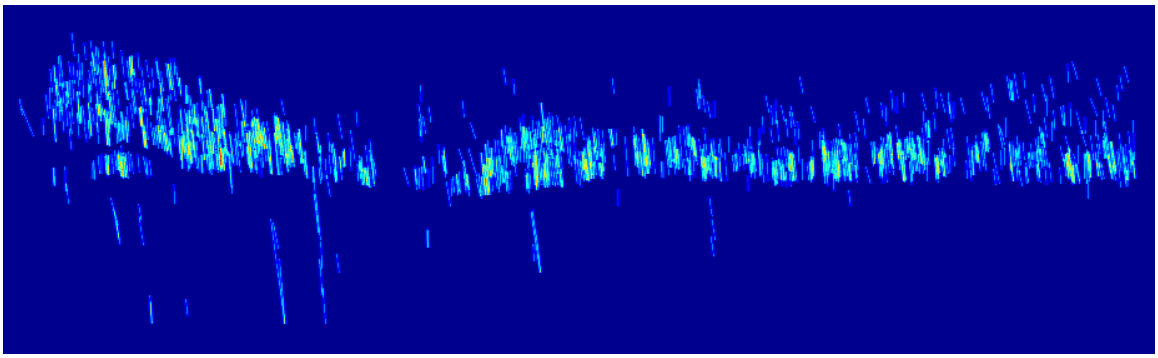

Figure 46: Heatmap created from edge detection to be used with meltback tracking.

The heat map is used as the external force and the initial active contour is placed along the location of the original top of the substrate, found using the bottom line and the known thickness of the substrate. By placing the contour at the original substrate/powder interaction layer it will be closer to the meltback depth than any other location thereby minimizing the amount of runtime and also reduces the amount of local maximums in its path. As shown in Figure 47 the active contour is able to bypass local maximums as it travels across the sample. The color of the lines shown in the figure denote the iteration step of the active contour, with the color red meaning a later step.

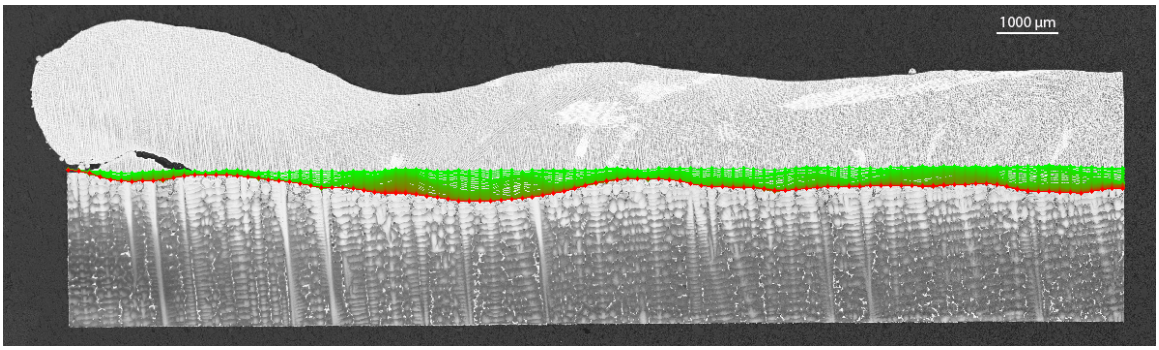

Figure 47: Active contouring iterations when finding the meltback depth for a CMSX-4 sample.

A small upwards force is exerted on the active contour as it is subjugated to the external force of the heat map. This allows it to better conform to the lower points found on the heat map, creating a closer approximation to the actual transition from

unmelted to processed material. Another reason to include an upward force is due to the possibility for lack of fusion in the sample, where the deposited powder is not joined with the underlying substrate. At these points there will be not be an intensity found on the heat map allowing that area of the contour to rise slightly above the top of the substrate. This is needed to better contrast times where the meltback depth exists, though at a very small depth, and where there is a lack of fusion. This rise in the contour can be seen in Figure 48 and is used in several instances in later analysis.

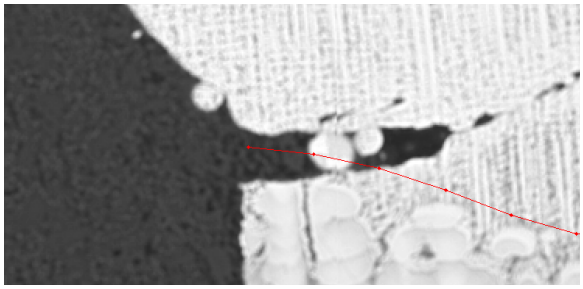

Figure 48: Meltback line when near a lack of fusion.

Once the contour reaches a point where it no longer shifts in position, and the total energy of the line remains near constant for two subsequent iterations, the active contour is recognized as completed. A final output is made, as seen in Figure 49 that shows the image with the final contour drawn on it. An active contour is created from a list of points with a specific spacing, seen as dots on the figure, while the interpolated line between the points is not accessible. Using the Bresenham's algorithm along with the contour points a complete line is assembled that represents the meltback line across the entire image.

4.2.4 CMSX-4 Detailed Dendrite Tracking

Finding the meltback in CMSX-4 samples depends on having access to a large amount of information regarding the new single-crystal deposit locations. The information does not need to be accurate in regards to each dendrite as it is the quantity of information that allows the meltback to be tracked. When finding the dendrites'

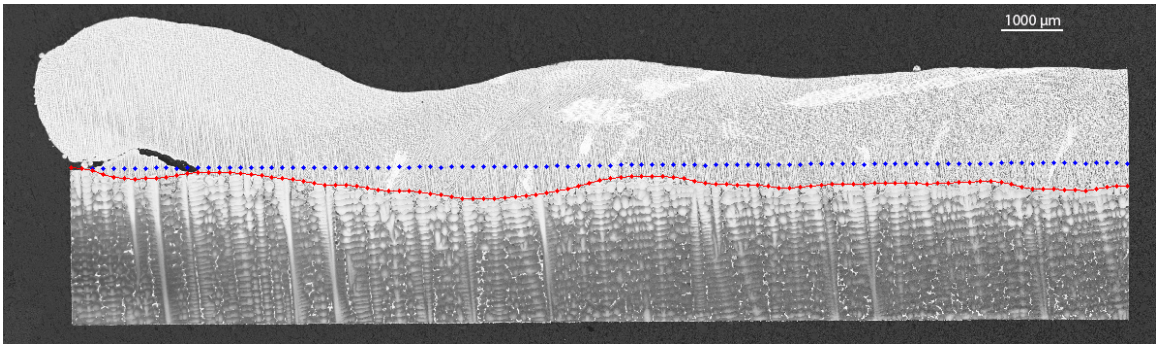

Figure 49: Final contour for a CMSX-4 meltback line.

angle of orientation and average primary trunk width a more detailed analysis is needed that stresses a smaller number but greater quality dendrite tracking.

The primary reason that a coarse analysis of the dendrites is used earlier in the program is due to the interference of the secondary dendrites. These small perpendicular offshoots from the primary dendrites create interference when trying to track the primary dendrite locations. The first step in performing a detailed tracking of the dendrites is to mitigate the secondary dendrites effect. To do this, the canny edge data found during the initial dendrite tracking function is called. Using the same procedure followed previously to create straight lines between the starting and ending points of each saved edge, the image is slightly blurred in that direction for pixels in close proximity to the line.

To do this the area around each line is convolved with a Gaussian kernel, Equation 24, with σ equal to ten. This 1-D kernel is rotated by the angle of the line using a rotation matrix, Equation 19.

$$g(r) = \frac{1}{2\pi\sigma^2} e^{-0.5\frac{r}{\sigma}^2} \tag{18}$$

$$R = \begin{bmatrix} cos(\theta) & -sin(\theta) \\ sin(\theta) & cos(\theta) \end{bmatrix} \tag{19}$$

Finally the area of interest around the line is convolved with the rotated kernel

using Equation 20. The convolution is performed only within ten pixels of any point on the line in question. This procedure is repeated for each line tracked previously, leading to the reason that each individual line influences only a small region around it, bounding the summation terms a and b seen in the equation. Keeping each blurring attempt localized mitigates the propagation of errors caused by a poorly tracked dendrite from the earlier section.

$$h(i,j) = \sum\sum g(a,b)f(i-a,j-b) \tag{20}$$

While the initial dendrite tracking was not highly accurate the general direction of each dendrite was found allowing the blurring effect to diminish the secondary arms. By blurring in this direction the primary dendrites shape remains largely unaffected while the secondary dendrites intensities are lessened, as shown in Figure 50(b).

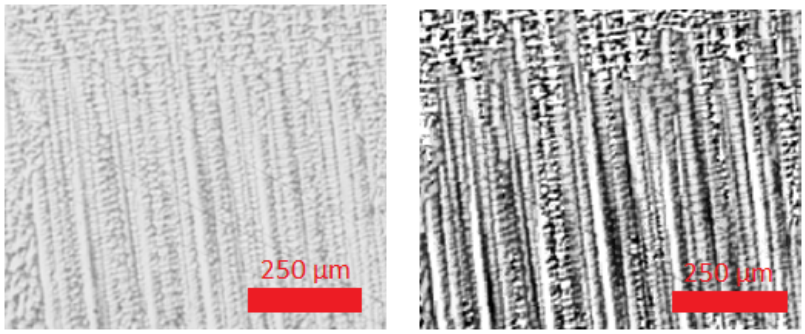

(a) Before Blurring (b) After Blurring

Figure 50: CMSX-4 sample before and after sharpening and blurring is completed.

After blurring the image using every traced edge the image then goes through a closing operation, the use of dilation then erosion. This removes low value outliers and can join high intensity regions which helps better highlight the trunks of each dendrite.

The canny edge detected lines that were saved during the basic dendrite analysis are recalled one final time. The starting point of each line is used as a possible location of a primary dendrite in the sample, allowing the function to have a more

refined search for dendrites. A single point is seeded at the starting location of each canny line, after which a separate procedure is followed. From the single point the area surrounding it on the heat map is searched for the direction holding the highest intensity. In the direction found, a new point is generated at a distance of five pixels, approximately 15 microns, from the preceding point. This is iterated five times before the angle of the created line is determined, now referred to as α. Once the angle is found the direction for any future points generated has to be within a tolerance of that angle as shown in Equation 21, with θ being the angle between the investigated point in question and the starting point for the line.

$$e^{-sin(|\alpha-\theta|)} \tag{21}$$

This is needed as primary dendrites are straight features and the only time the contour being created would need a drastic change in angle is if tried to follow a different dendrite or came upon a stray grain formation. Creating lines from the canny edge points and limiting their direction of growth limit the number of dendrites that can be tracked but both techniques are needed to avoid the possibility of false positives.

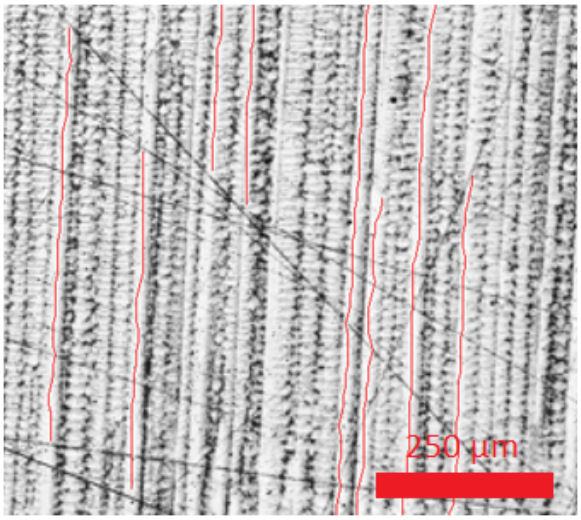

Figure 51: Dendrites tracked using detailed analysis overlaid with CMSX-4 image.

Every time the location of greatest intensity direction is found before creating a new point the intensity level is compared to a threshold. The threshold is high enough that if a single pixel along the length being checked is near zero, then it is not acceptable. This stops the line from jumping two closely aligned dendrites, but also adds a deterrent for directions that have a low average pixel density. If none of the intensity summations from the five pixels, in multiple directions, is not above the threshold then the line is terminated. At this point the total length of the line is checked to see whether it is long enough to have significance. If the completed line is long enough then each point is saved for later use.

This procedure is followed for every canny edge starting point throughout the image, though lines cannot be formed on top of one another or cross paths. The final result are dozens to hundreds of lines found across the length of the sample with accurate tracking of the primary dendrite trunk as seen below.

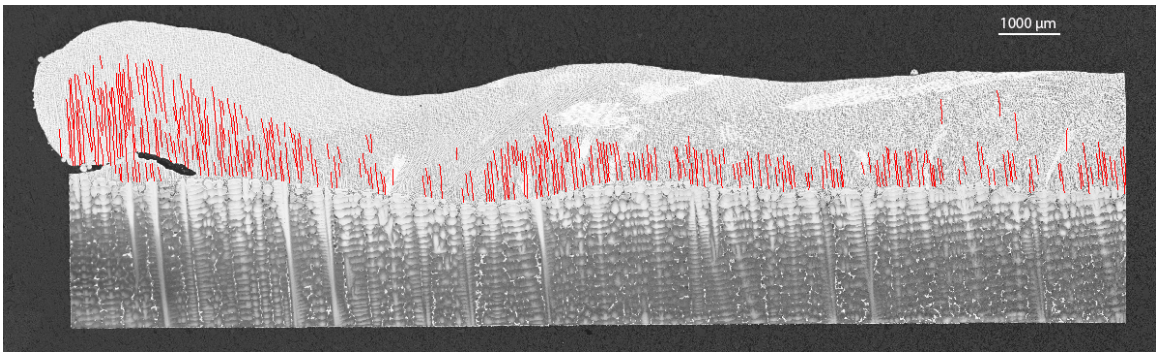

Figure 52: Accurate dendrites shown across an entire CMSX-4 sample.

A heat map is generated using the starting and ending point of each accurate dendrite tracking, following the procedure used when finding the CMSX-4 meltback line. The single difference between the two is that each accurate dendrite line effects pixels further out than the meltback procedure. This is needed as there are fewer lines than before, due to the much more stringent standards, so they must cover more ground. Again the intensity of a pixel is directly proportional to its proximity to the actual line so the newly added values are extremely small.

After following the same guidelines as when finding the meltback depth of CMSX-4 an active contour is established along the top of the sample. This line then propagates downwards until reaching the SX termination points at the top of the tracked dendrites as seen in Figure 53.

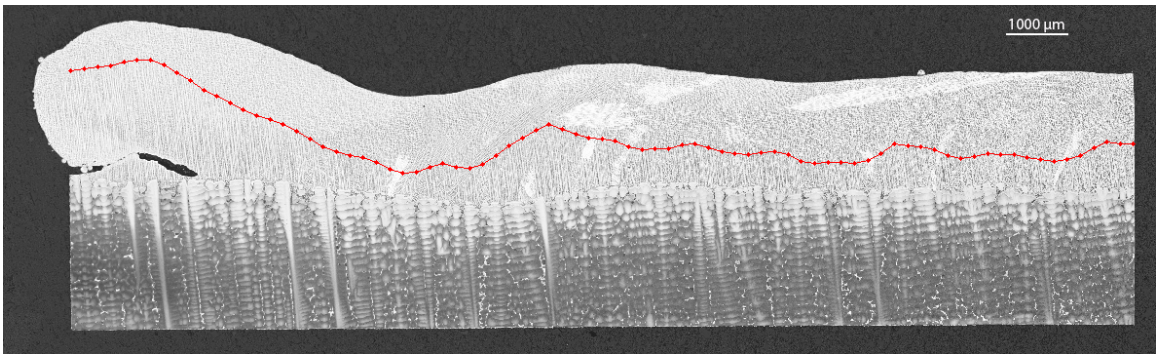

Figure 53: Final contour found when tracking the single crystal deposit on CMSX-4.

It is difficult to see the transition between the vertical single crystal growth and the equiaxed or misoriented sections when the image is so small. Below is a closer view of the SX termination line at a single crystal to equiaxed transition location. It shows a close approximation to the actual termination point across the region. The most problematic area of the SX height contour is the occurrence of large stray grains. A small stray grain can be seen near the venter of the image below, though at this size it does not cause any undue issues. As detailed in further work this would be an area of further exploration, to locate and track all of the stray grains of the image.

The angles of the dendrites are then found for each line generated with the location along the x-axis, the length of the sample, and the angles value being saved for further analysis. Only the longest dendrites tracked are used to provide data for this microstructure feature to give a more accurate representation. The points must also terminate near the meltback line as it is the angle relative to the substrate that is needed. A simple plot is shown with the angle of the primary dendrite being along the y-axis and the length of the sample along the x-axis.

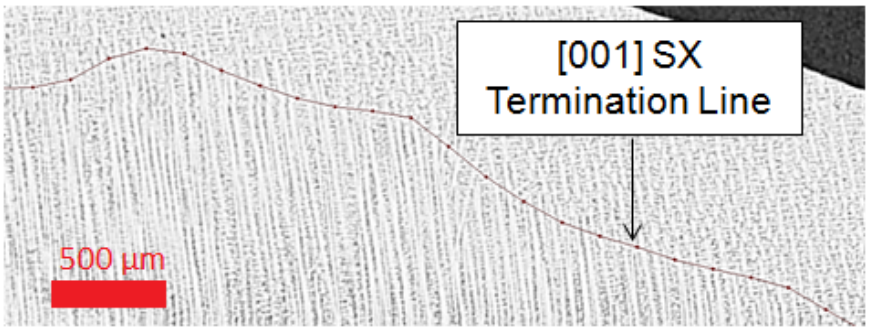

Figure 54: A close view of the SX termination point found with the active contouring.

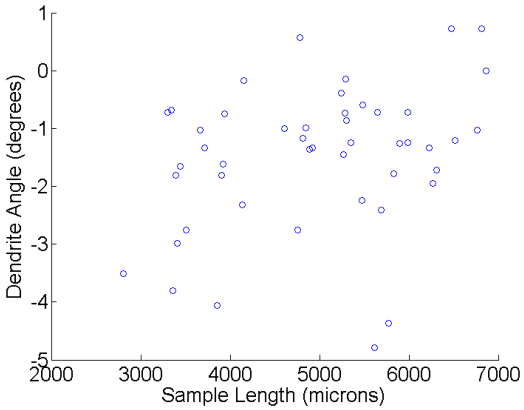

Figure 55: Angle of newly deposited dendrites along the sample length.

Finally the width of the primary dendrite trunk is found for each of the lines along their entire length. The heat map previously created is differentiated in the x-direction so that the transition from the dendrite trunk to the secondary growths, which were blurred in a prior step, is highlighted. For each point that was generated in the line, every five pixels, the transition from trunk to secondary growth is found to the left and right of the point.

To accomplish this an assumption is made that the center dendrite trunk area is clipped, or close to it, in the image. Since the center area of the trunk spans many pixels this assumption can be shown as in Equation 22 and 23. A search is then conducted to the left and right of the point in question looking for a pixel that has the first derivative not equal to zero.

$$\frac{dy}{dx} = 0 \tag{22}$$

$$\frac{d^2y}{dx^2} = 0 \tag{23}$$

The interior of the dendrite trunk will have a small variation in value near its edges and this is taken into effect. When a nonzero value of the first derivative pixels is located it is checked against a large threshold, set to 20 through analysis of multiple dendrite trunks. If the pixel in question is below the threshold then it is most likely not the edge of the trunk and a value is saved slightly greater than the one in question as a secondary threshold. As the search continues, if a pixel in question exceeds this second threshold then it is assumed to be the edge of the trunk. Looking at the second derivative of the heat map at that point will determine if the termination point is on the left or right side of the trunk.

$$\frac{dy}{dx} < 0 \implies \text{Right Side Termination} \tag{24}$$

$$\frac{dy}{dx} > 0 \implies \text{Left Side Termination} \tag{25}$$

The search is made both to the left and the right of the original point from the created contour. If the search conducted to the right of the original point does not result in finding a right side termination then the data found is labelled as error prone and is not used. This same analysis is done on the left side. This check helps mitigate issues during operation.

After completing this analysis for every point the average is found for the dendrite and saved relative to the location along the sample length. Figure 56 uses the starting and ending points for the accurate dendrites to draw a straight line near the center of the primary dendrite trunk, as shown with the red line. The two blue lines are created at an offset to represent the average width along the dendrite length.

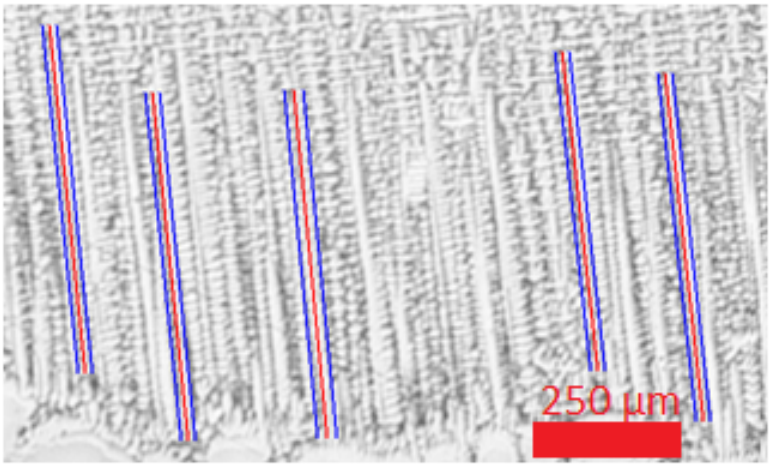

Figure 56: Dendrite width overlayed on a CMSX-4 image.

4.2.5 René-80 Meltback Depth Tracking

Unlike CMSX-4, and other single-crystal superalloys, equiaxed superalloys do not have as clear of a transition from the substrate to the re-melted region denoting the meltback line. When viewing Figure 57 at this scale it is difficult to see where the meltback line is across the entire length.

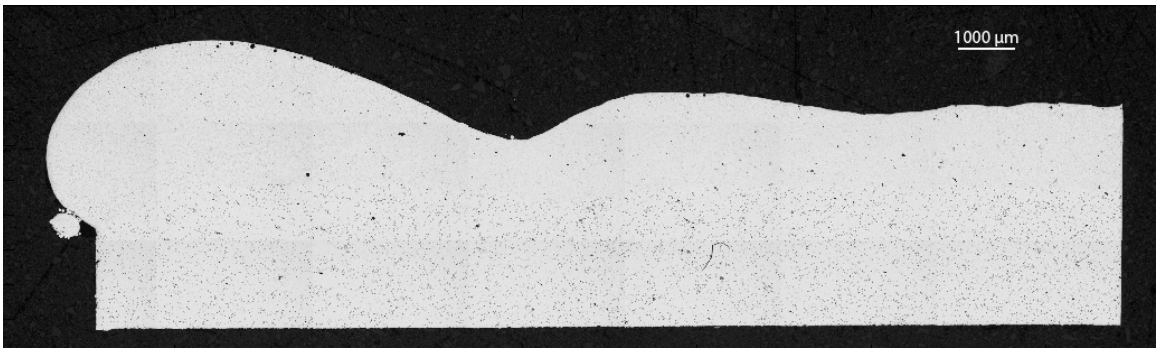

Figure 57: Initial image of René-80 microstructure.

Several steps are taken to better realize the transition points in the image by looking at small features found in René-80 samples that change across the meltback line. The first step is to average each pixel of the image using an 11x11 kernel. This is done as the deposited material has a finer amount of variation across it but it also tends to be slightly lower in intensity than the cast section. As shown in Figure 58

the meltback line becomes more visible though some areas are still problematic and further processing must be completed before the meltback line can be isolated.

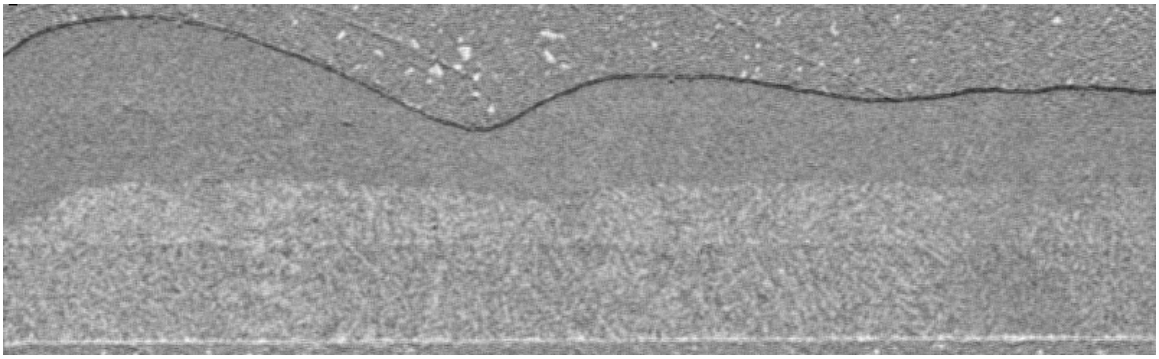

Figure 58: René-80 image after averaging the pixels.

Searching along the bottom of the substrate and the top of the sample, using the top and bottom lines found while isolating the sample, average pixel values for the two regions can be determined. Using an intensity value between the upper and lower numbers and subtracting that amount from the image gives a starker contrast between the substrate and remelted region by making a majority of the substrate positive while the newly deposited region becomes negative. An opening algorithm is then used on the image to better connect separate features and fill holes found in high intensity locations. The image is then converted to a binary image, using a zero value threshold, providing the figure shown below. This resulting image makes the transition from the substrate to the processed section easily visible to the eye.

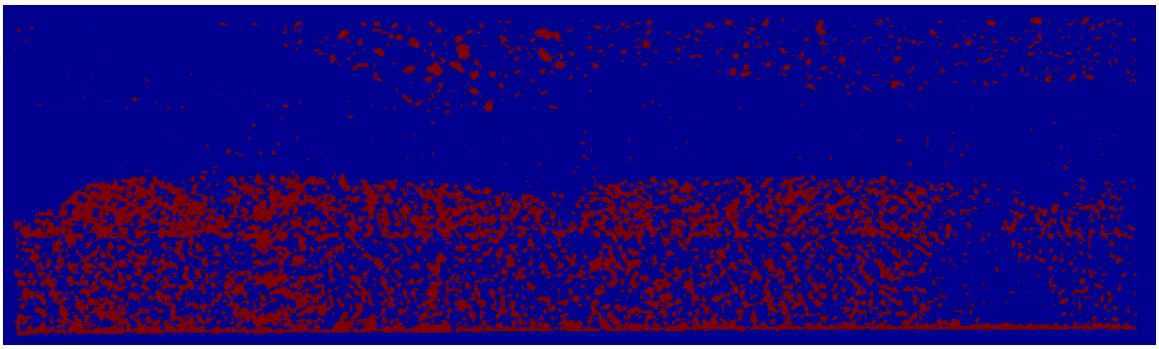

Figure 59: René-80 sample after averaging and a binary threshold.

This data map provides a good contrast at the meltback depth but some areas still lack values indicating a transition, specifically near the end of the sample in Figure 59. The blue region that is located inside of the substrate along the right side the image will cause an active contour to treat it as though it is a part of the newly processed section, giving a false positive. The main difference between large blue regions in the substrate and the blue regions in the newly formed sections is that the substrate areas are still in close proximity to the red islands. Using this reasoning an additional step is undertaken to assess each pixels proximity to a zero pixel, shown in Figure 59 as red points. A distance transform of the image is taken using a Euclidean distance. Distance transforms of a binary image denotes each pixel, or voxel if the matrix is 3-D or larger, by the distance to the closest non-zero pixel following Equation 26. The $d(p, q_k)$ term uses the Euclidean distance, Equation 27, to find the distance between original pixel p and and potential pixel q located within image P. This is repeated for all points k within the listed set of S and the minimum path is chosen [34, 10].

$$t(p) = min_k\{d(p, q_k) : P(q_k) = 0 \wedge 1 \leq k \leq S\} \tag{26}$$

$$\sqrt{(x_1 - x_2)^2 + (y_1 - y_2)^2} \tag{27}$$

This provides a template shown in Figure 60, denoting each pixels distance from the closest nonzero pixel.

Overlaying the two maps, while putting greater emphasis on the binary image than the distance mapping image, provides a detailed transition between the substrate and the remelted section of the sample while minimizing errors found in the binary image. The meltback line is found with a good consistency in samples as shown in Figure 61 and with the inclusion of the binary distance mapping, the active contour can bypass sections of local minimums.

As it is difficult to see the meltback transition using an original, unaltered, image

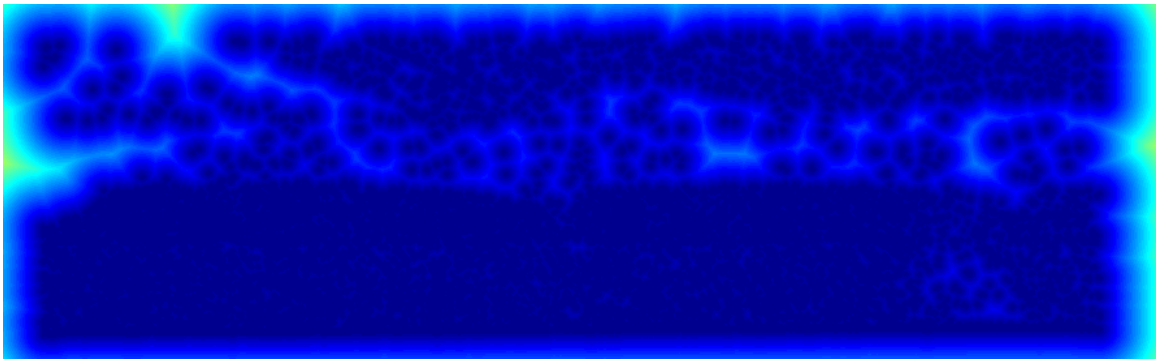

Figure 60: René-80 binary plot analyzed for distance to high pixels.

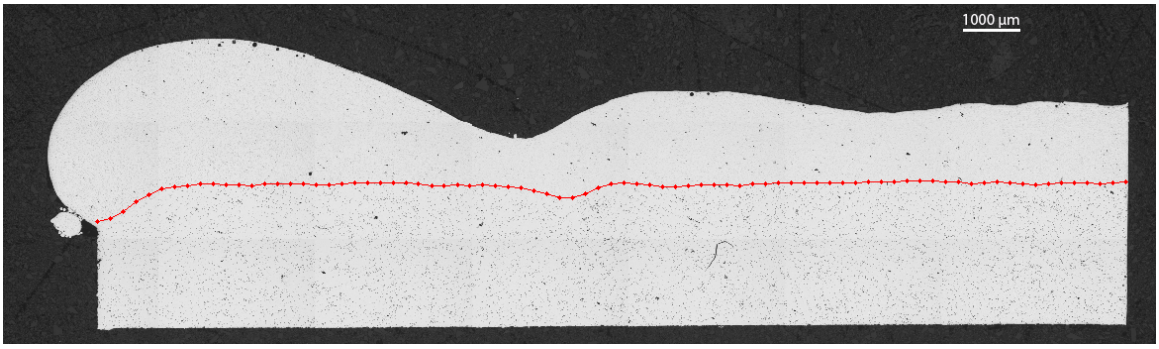

Figure 61: Meltback line tracked across an entire René-80 sample.

a closer look can help provide a better visualization. As seen in Figure 62 the newly processed section, on the upper section of the image, has a larger amount of intensity variation which is a major point of separation used to find the meltback.

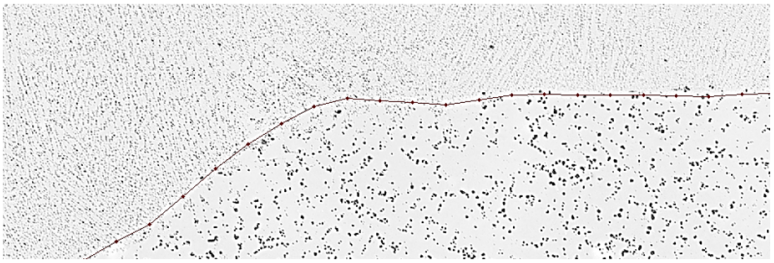

Figure 62: Closeup view of the Rene-80 meltback line.

When finding the meltback depth the active contour is initially created near the bottom of the substrate, from where it propagates upwards. Shown in Figure 63 are the active contour steps taken to converge to the solution viewed above. Of special note is the right side of the image in the region where the problematic area was

described earlier. As can be seen the active contour was able to bypass the local maximum area, though it took a great increased number of steps to do so. If the second heat map, created using the Euclidean distance from a pixel to a high intensity pixel, had been given a larger weight, then this area would be less problematic but an unintended consequence of doing so would be a less severe transition at the meltback depth.

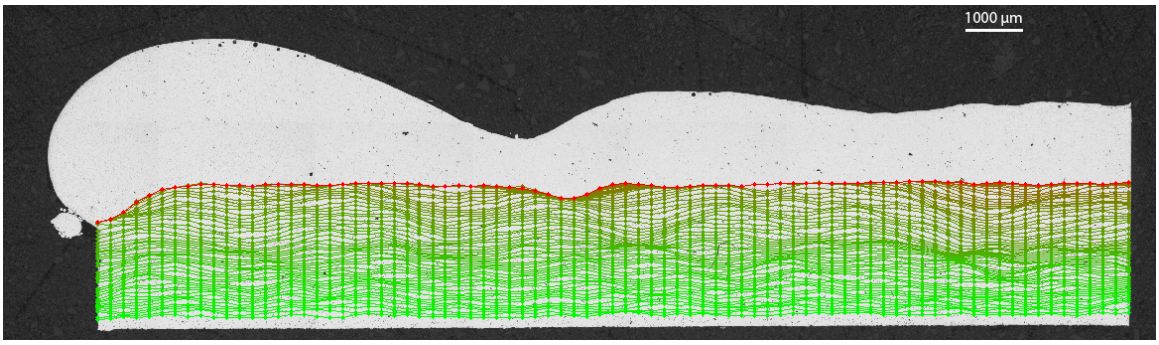

Figure 63: The active contour steps taken when finding the meltback depth of a René-80 sample.

4.2.6 René-80 Crack and Pore Tracking

When locating the cracks and pores the most important feature of the image is the intensity values found in the cavities, since it is closely associated with the intensity of the surrounding Bakelite. Using a threshold on the image based on this information, a binary image is created as shown in Figure 64. This creates a near ideal situation where only the pores and the cracks, shown in red, are discernable from the sample's body.

Using an algorithm that tracks connected components in a binary image, a list of each section shown in red in the image above is isolated. Every pixel of the image is searched, with each being either one or zero. When a zero value pixel is found, denoting a crack or pore, a flood algorithm is used. A flood algorithm finds all connected points of the same characteristic, in this case zero valued pixels. From the starting pixel each neighboring pixel is investigated. If a searched pixel is the value

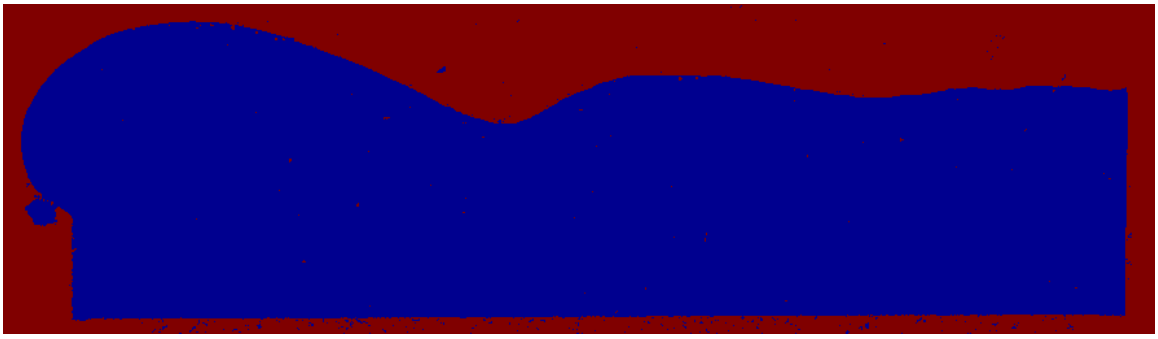

Figure 64: René-80 sample after binary threshold used to locate pores and cracks.

of interest then it is recorded as a pixel in the flooded section. For each new iteration each neighboring pixel to the flood section is checked until no additional pixels are found. For each step the newly added pixels must also be searched for duplicates and trimmed accordingly.

Each listed flood section is then searched for multiple criteria to establish its relevance and type. First the area of the component is determined. Next the major axis of the tracked object is called and used as the diameter of a circle when finding a theoretical area, with the radius denoted as M. By comparing the area calculated, which is representative of a perfect circle, and the actual area of the component in question a crack can be differentiated from a pore. Cracks tend to have a long major axis, extending along the length of the crack, that would create a large ideal circular area. When comparing this area to the actual crack area, the number tends towards zero in contrast to a pore that is more circular in nature which tends towards one.

$$Eccentricity = \frac{FloodArea}{\pi M^2} \tag{28}$$

In order to best determine when an object is a pore or a crack using the method above a number of sample shapes needed to be explored. Pictured in Figure 65 are a group of objects that were tested. As can be seen in the image there is a sharp contrast between circular and lined shapes. In some instances there can be an issue with differentiating between the two. This is why a system will make problematic

shapes easily viewable for the user to inspect has been incorporated in the program. The shape in question will have been placed as either a crack or pore at the time of the search but it is a simple matter for the experimenter to alter which list it is on if corrective measures are needed.

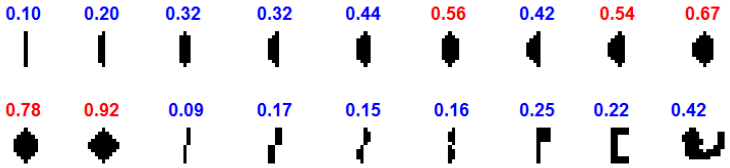

Figure 65: Sample shapes used to isolate settings for cracks and pores.

After checking each component found in the image for their degree of circularity, the final results are tabulated for later use and shown on the original image as seen in Figure 66. On a final output image all of the pores are highlighted with red, the cracks are highlighted with blue and the problematic shapes are denoted with green. The number of problematic shapes is very low relative to the total number of pores and cracks in a sample, usually being near zero in total, but this color system allows for a quick and easy visual inspection of the operation.

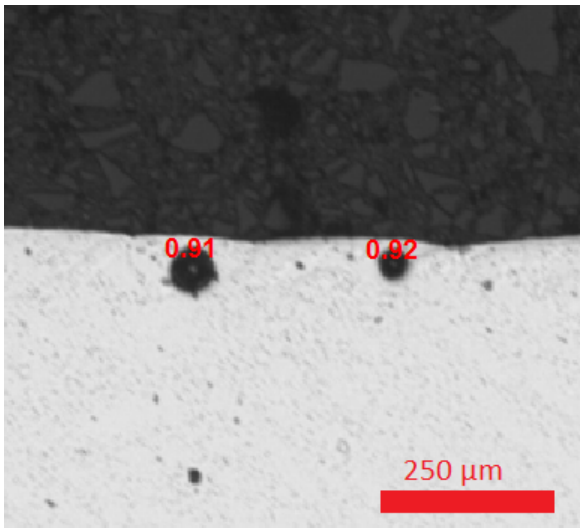

Figure 66: Pores found on a René-80 sample with level of circularity labeled for each.

It is worth noting is that some programs already exist to track the cracks and porosity found in micrographs. One such example is a program available through Clemex that follows the same procedure described above [14]. An improvement in the present pore and crack tracking program is that it not only recognizes the pores and cracks but can also track where they are relative to the meltback line. This can separate the features found in the cast section of the material and the newly formed deposit, which is of greater significance for developing the SLE process.

4.3 Data Retention

As each sample is analyzed using all of the microstructure recognition programs described in the preceding sections, the data must be organized and saved for later use. Some data is in the form of a single value, such as the power level of the laser for the sample in question, while others are vectors thousands of cells long so any attempt to organize information by samples must be able to contain these different types. Structure arrays, which can hold various fields and data, were utilized in Matlab to save this information. CMSX-4 and René-80 each have their own structure array to contain all of the information for each sample analyzed. As a new sample is being investigated a new structure is added to the structure array for that specific sample, allowing for an ever increasing number of samples to be added in subsequent experiments. Shown in Table 2 are all of the fields associated with each structure, the information for the sample in question, for CMSX-4 and Rene-80.

Table 2: CMSX-4 and Rene-80 Retained Microstructure Information.

CMSX-4	Rene 80
Sample Name	Sample Name
Laser Power	Laser Power
Scanning Velocity	Repeat Velocity
Repeat Scans	Raster Velocity
Powder Thickness	Repeat Scans
Substrate Deformation	Substrate Deformation
Total Deposit	Total Deposit
Melt Line	Melt Line
Melt Depth	Melt Depth
SX Deposit	Pore List
SX Angle	Crack List
Substrate Angle	Microns Per Pixel
SX Width	
Microns Per Pixel	

4.4 Data Analysis

There are several methods utilized to interpret the information gathered in the microstructure investigation stage of this thesis, the first being to better visualize the features. In the past, when comparing different samples visually to try and find relations between microstructural features and SLE settings, the only approach was to print the images onto computer paper and lay them side-by-side. Using the information saved in the Matlab structure it is now possible to plot the information and if desired overlay multiple lines onto the same plot. Any continuous feature, such as meltback depth or deposit height, can be plotted as lines to contrast these characteristics. While any samples can be plotted, some comparisons hold greater significance than others. By plotting samples that have only one SLE parameter changing between them, such as laser power, the first order interaction with the feature being shown can be better visually compared. Figure 67 shows a plot comparing two samples where the only change in settings is the laser power and it highlights where the power setting has greatest significance on meltback depth.

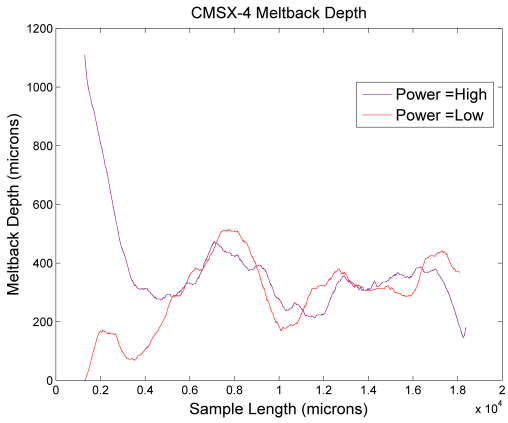

Figure 67: Direct comparison of two CMSX-4 sample for meltback depth.

To save time and effort a function was created that would search through all samples of the same material, CMSX-4 or René-80, and find all of the groups of samples where a single parameter is changed. Plots like the one above are then created for each group showing the significance of every feature. This allows all of the relevant information to be relayed to the experimenter, giving a greater chance for the observation of the lower order effects caused by individual parameter changes.

Some features cannot be plotted as single lines and are represented in ways that best features their occurrence. For pore and crack feature detection the output is a list of every pore and crack along the sample, making a delta plot an ideal way to visualize the information. Figure 68 shows two plots created from the same sample with each peak value indicating either a pore or a crack. These plots can also have different samples overlayed onto each to allow for comparisons between different samples. This gives a good representation for both the frequency of pores and cracks while also giving an indication on where they are located. Totals of each can also be easily tabulated to give the user a single value to compare different specimens.

Another unique type of feature that is tracked is the angle of the primary dendrite in the newly formed material relative to the underlying substrate's dendrite angle. The location of each dendrite tracked is saved in the structure array along with the

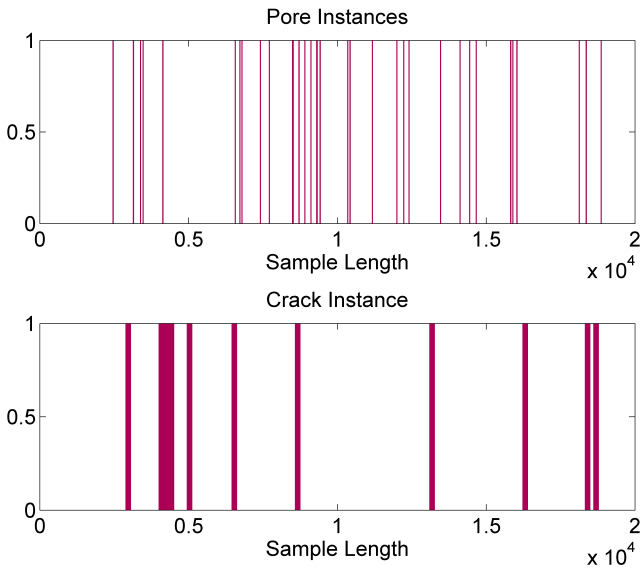

Figure 68: Crack and pore delta plots for a Rene-80 sample.

angle of the dendrite at that location. Outputting a plot with the sample length along the x-axis and the angle of the dendrite on the y-axis visualizes the dendrite angles going across an individual sample, Figure 69. It is also possible to plot only a linear or quadratic fitted line for each sample's angle data, providing a cleaner interpretation of the microstructure feature.

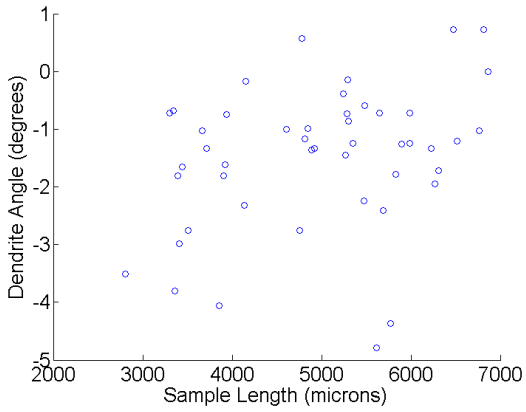

Figure 69: Angle of primary dendrites across a sample length.

Finally the various microstructure features can undergo data fitting to find an equation that best fits the parameters to the feature in question. This is done using

two distinct steps, window types and fitting types. Each sample can have the information tracked for a feature windowed into smaller subsets for analysis. It starts at a single window, which encompasses the entire sample, then increasing it through two, three and four windows each of equal size. A data fitting equation is then found for each window. When finding this fit a linear equation is attempted, followed by a quadratic and finally a combinational equation that combines effects like (power)x(scan speed), is tried. Each of these data fitting equations is then checked for their degree of accuracy for the single window and the best choice is saved. After this is attempted for each window in a single sample the degree of accuracy for all of the best data fitting equations combined is found and saved. This global fit is then compared for each window size to find which will provide the most accurate representation.

Once the ideal data fitting equations are found for a sample, the number of equations depending on the best window size determined, each equations constants can be reviewed. When performing the search for the best type of data fitting equation all of the relevant terms are used, so when trying a quadratic equation each parameter has a linear and squared term, to simplify the search. At this point, when only a small number of equations need to be reviewed, each term in the equation can be searched for its importance, as described in the Background section.

With a complete set of data fitting equations for each sample, a set of predicted points are calculated along with their degree of uncertainty. Using a combination of these predictions, a global map is created that shows areas of interests on the process map for future trials. A search is conducted in two areas of the process map, locations of high certainty for each prediction and areas for medium certainty. High certainty denotes locations that are well explored and give a high confidence to the predicted value. Medium certainty predictions are those that extend slightly beyond the area of testing. The best prediction is then found for each of these certainty types and

compared. If the best point is located in the medium certainty area then further exploration is needed for the process map, so a fractional factorial DOE is created in the region of the best point found. If the best point was located in the high certainty region then no further exploration is needed. Instead a response surface DOE would be completed that would provide a very detailed analysis of the area in question.

CHAPTER V

RESULTS

Direct comparison plots were created to contrast the meltback depth and deposit height for René-80 and CMSX-4 samples. Creating and analyzing these graphs allows the experimenter to better visualize how the samples change depending on different SLE parameters and can provide insight into first order relations for each microstructural feature. The data fitting, and the contour plots created with the realized information, show a deeper level of interaction between the parameters and microstructural features.

5.1 Data Interpretation

5.1.1 René-80 Meltback and Deposit Analysis

The first approach to utilizing the data collected is to directly overlay multiple lines, that could express the level of meltback or deposit across a sample, that have only one SLE setting changing between them. This gives the user the ability to compare samples where only one parameter is altered, such as power, so that a better understanding of first level interactions between the parameters and resulting microstructure are realized.

There are four SLE parameters that will be discussed and compared in the results section for René-80; the laser power level, repeat scan speed, raster scan speed and the number of repeat scans. The repeat scan speed is used to control the laser movement during the initial formation of the meltpool at the beginning edge of the substrate, Figure 70(a). The raster scan is the speed when the laser is moving across the rest of the substrate, Figure 70(b).

The first plot presented is a comparison of deposit heights between samples. When

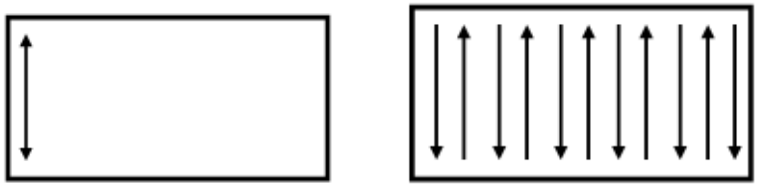

(a) Repeat scans (b) Raster Scans

Figure 70: Types of scans used in the SLE process.

investigating the amount of material deposited for René-80 samples several relations can be found when comparing samples of differing power levels, Figure 71(a). In both plots provided, an increase in power level will result in a larger buildup of material at the starting edge, as the meltpool is being established. The consequence of this large buildup can then be viewed as the meltpool becomes starved shortly after in three of the four lines. It seems as though with a larger power level the meltpool increases in size allowing more powder to enter it. The additional deposit at the beginning of the scan is unnecessary, as it would be removed during post processing to leave a flat surface. The one line that mitigates this starvation is the lowest power level of the four, 300 Watts, and is able to maintain a much more consistent deposit across the sample. For the later section of the samples, having a larger power level can also increase the deposit height, however, when comparing the two plots below against one another it is clear that other parameters greatly influence this as well.

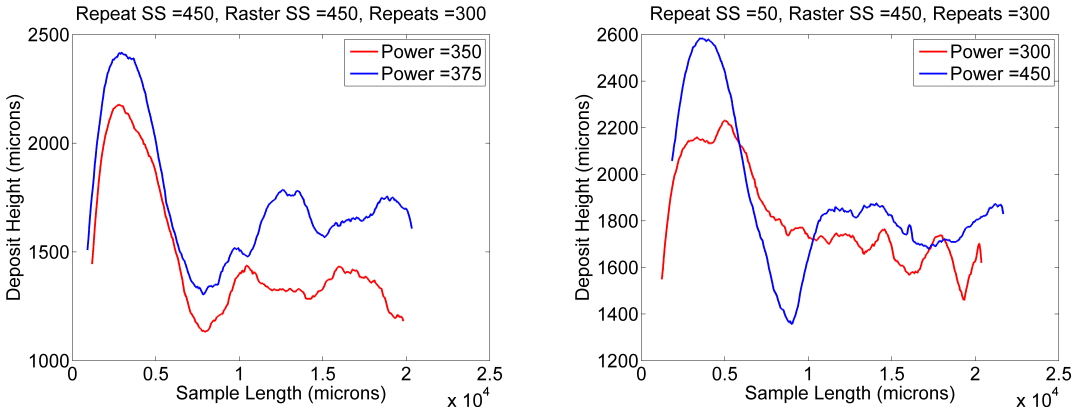

Figure 71: René-80 deposit height with various power levels.

When looking at the change in the number of repeat scans, as shown below, an interesting trend can be seen. In both Figure 72(a) and Figure 72(b) there is a dip in deposit height around 800 microns into the sample for a specific repeat value of 250. When the number of repeats are lower or higher than this value the dip in starvation is lessened. As the number of repeat values comes closer to the 250 mark the starvation dip will approach a minimum point of only 800 microns of deposit. While the drop in deposit height is significantly larger near the 250 repeat mark, the amount of buildup prior does not seem significant. Bringing into question what caused the sudden drop in height. Further tests would need to be done around this number of repeats to see if it is an actual effect in the SLE process or a minor occurrence.

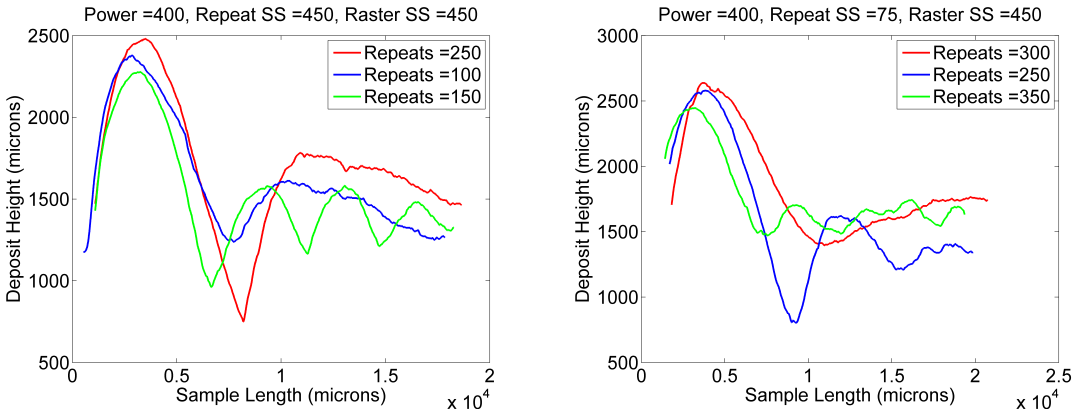

Figure 72: René-80 deposit height with various repeat levels.

The next area of analysis is the meltback depth in René-80 for various samples. For many of the René-80 samples created, the scan speed was varied from the repeat scans to the raster scans to better control meltpool generation. Figure 73 shows a contrast between a high repeat scan speed of 450 mm/sec and a lower repeat scan speed of 75 mm/sec, while holding a constant raster scan speed. By reducing the scan speed the amount of meltback into the sample drastically increases to over six times the amount, though its contributions to the meltback for the rest of the sample is not nearly as noticeable.

The plot shows that altering the repeat scan speed has a very large effect on the

amount of energy entering the system near the start of the scan. The main issue is the energy dump is not pre-heating the sample far enough in advance to allow the meltback to be maintained at a proper depth. Slowing the scan speed to 75 mm/sec did leave the meltback depth extended into the substrate for a slightly longer time than the 450 mm/sec scan, but the excessive meltback depth created may outweigh the positives of this approach.

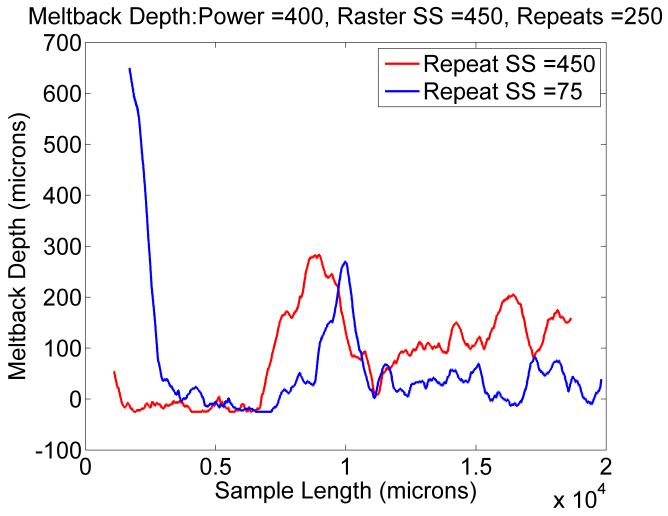

Figure 73: Rene-80 meltback depth with different repeat scan speed levels.

When considering the repeat scan speed at lower values, between 50 and 150 mm/sec, the amount of meltback at the beginning of the sample can vary widely. In the two plots below, all three samples that had a repeat scan speed of 75 mm/sec had a meltback over 1mm deep near the beginning of the scan, which also falls in line with the meltback seen in the previous figure. At speeds higher and lower than 75 mm/sec the amount of meltback is less significant, which can again be seen with three different samples. One explanation that could account for this change in meltback depth near the start of the sample would be to separate the conditions leading to less meltback in the 150 mm/sec run and the 50 mm/sec run. The 150 mm/sec sample may be following the same pattern noted in the figure above, a higher repeat scan speed leading to a meltpool being established with less energy input. The 50

mm/sec samples could be seeing a consequence of such a slow scan speed. If the laser is not moving fast it may take longer to establish a continuous meltpool across the sample width. In the time that it takes for the laser to leave one side of the sample, scan the width, and arrive back at the starting point, the material could have cooled significantly. Taking longer to establish a continuous meltpool along the sample width could also hinder the pre-heating along the sample length, accounting for the very poor meltback depth maintained in the later portions of the sample.

Keeping the repeat scan speed low is a very recent development for SLE processing and little is currently known on how the sample will react to changes. The plots shown here signify that further experiments should be conducted at low scanning speeds while keeping their variation small, as it is easy to see that a small variation in scanning speed in the sample can cause drastic changes.

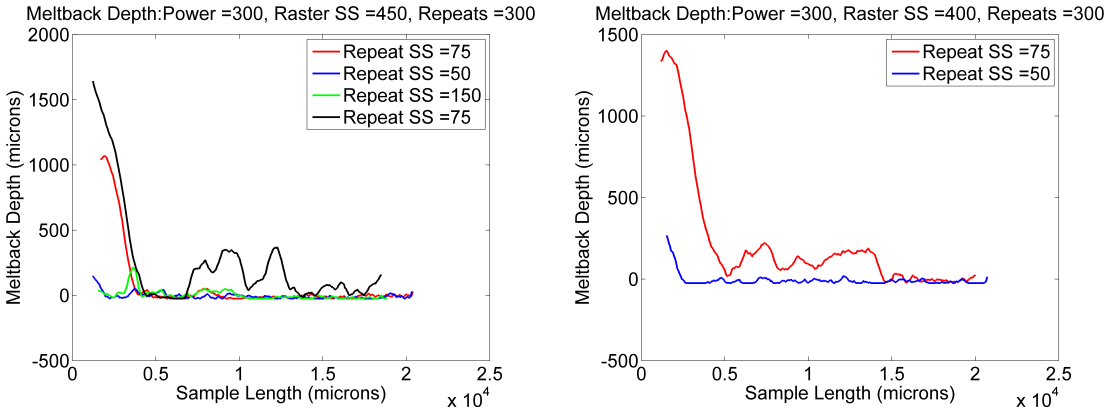

Figure 74: René-80 meltback depth with different repeat scan speed levels.

When considering both deposit height and meltback depth it seems that the most problematic area is the location of starvation and low meltback depth when the process transitions from the repeat scans to the raster scans. In regards to the laser power, the best solution seems to be to keep the power lower during the initial scans so that the amount of power flowing into the meltpool is lessened. The meltback depth has shown very little in the way of an improved result when moving between a slower and faster repeat scan speed, though the initial meltback depth can clearly be

altered. A technique that may help increase the meltback depth to an acceptable level near the repeat-to-raster transition point is to start at a slower scan speed for the repeat scans, then transition to a faster raster scan speed in a linear fashion instead of a step function. This would allow an increase in preheating for the sample and if the power is kept low the meltback depth should not become too excessive.

5.1.2 CMSX-4 Meltback and Deposit Analysis

The first microstructure feature to be explored for comparison is the SX deposit height relative to the original substrate location. As stated before, this is the equivalent microstructure characteristic to the René-80 total deposit height. Special consideration should be placed on areas of the sample that exhibit the lowest SX deposit, as this would be the largest usable amount for a sample after it is ground flat. Direct comparison plots are again utilized to better overlay the samples and to provide an avenue to enhanced comprehension of first order effects.

Four SLE parameters have been altered during all of the experiments used in the CMSX-4 trials to-date. As seen with René-80, the laser power and number of repeat scans are used. For CMSX-4 samples the laser scanning speed is kept constant through the repeat and raster scans and now accounts for only one variable. The final parameter for CMSX-4 samples is the amount of powder placed on the substrate before scanning; it can be as low as 1mm and as high as 2mm in the samples.

The first area of exploration with CMSX-4 samples is the single crystal deposit height relative to the original substrate-to-powder layer, before processing occurs. Altering the amount of powder laid on top of the substrate before scanning has a much more consistent relation to the SX deposit height than any other factor. The powder thickness does not cause any large changes in where minimum and maximum deposit heights are located across the sample length, but it does offset the entire line. The increase in powder thickness causes a vertical shift in the line almost identical to

the amount of additional powder used, in the later portion of the samples. Near the start of the scans the increase is larger than the change in powder height. The cause of this would be due to the larger amount of powder the meltpool has access to, both in the later portion of the substrate and in the excess powder region surrounding the part within the well. Overall this result agrees with a practical aspect of SX deposition; the more powder available during the scan the larger the buildup.

While this trend allows for ever increasing single-crystal deposits, there is an upwards limit, not due to the amount of deposit but caused by balling at the starting edge and a shallow meltback depth. This aspect of the microstructure will be further detailed later in this section.

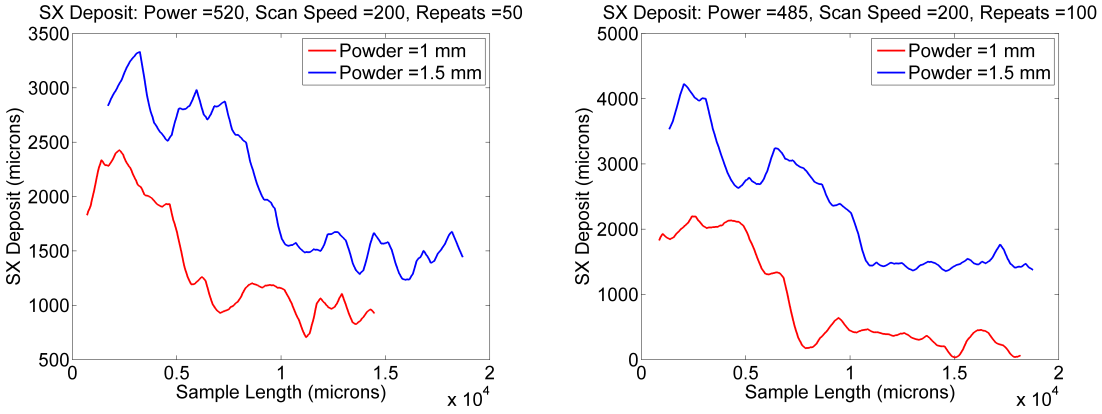

Figure 75: CMSX-4 deposit height with varying powder thickness.

Three factors for meltback depth in CMSX-4 samples are detailed below, one being laser power and the second the powder thickness and finally repeat scans. As can be seen in Figure 76 an increase in laser power, by almost 50 Watts, does not have an adverse effect on the meltback depth in the later portion of the samples. Instead the last three quarters of the samples were very consistent and displayed no influence with the power level. This is interesting as an increase in power is usually regarded as a direct contributor to an increase in substrate preheating, a direct cause to excessive meltback depth later in the sample. One possible explanation is the power combined with the scan speed has a greater effect on excessive meltback depth or that power

has no direct relation to this feature in the later portions of the sample. This type of relation is better investigated using the data fitting function to explore higher level interactions.

Unlike the last three quarters of the sample the first section did have a strong relationship to power, as a higher power level caused excessive meltback in contrast with the low power level having a lack of fusion at the immediate starting edge. This is a common occurrence with CMSX-4 samples as a larger amount of energy is being placed into the meltpool during its formation.

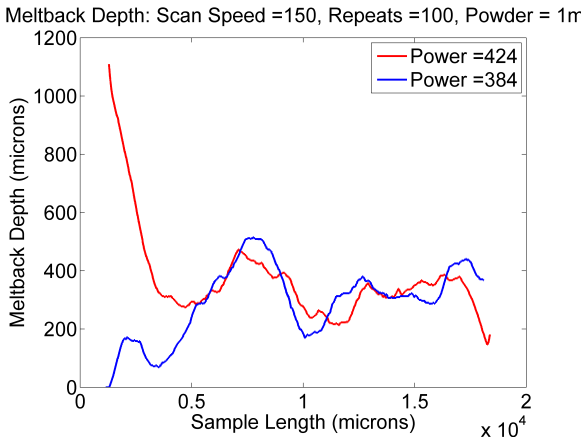

Figure 76: CMSX-4 meltback depth with different power levels.

Powder thickness, as shown below, can drastically change the amount of meltback depth found in CMSX-4 samples. In large part this is due to the difficulty of working with larger powder thicknesses and creating a good fusion between the substrate and deposit material when initializing the meltpool. During the meltpool formation stage it is common to see the powder melt become a ball that sits on top of the substrate without actually melting into it. As more time goes on the molten powder ball continues to absorb the energy from the laser and begins to preheat the unmelted powder that it is touching. It is not until the meltpool starts progressing into unmelted powder that there is a chance for the meltpool to extend into the substrate. This can be overcome using higher power and lower scanning speeds, but at similar parameters

outside of powder thickness it is easy to see the difficulty when working with larger deposits.

Comparing the results for SX deposit height and the meltback depth while changing powder thickness shows that it is important to find a mediation point between different features. Another area of consideration with the changes in powder thickness is the importance of the single-crystal deposit height relative to the meltback depth. While an increase in powder thickness allows for a greater SX deposit height, the difficulty controlling the other microstructure features may not make it worthwhile. This analysis instead brings into light the importance in maintaining a more consistent SX deposit height, so that the deposit may be made with a lower powder amount. Working towards maintaining a flatter SX deposit height instead of maximizing it could help mitigate other issues that arise when processing samples and would provide a significant shift in focus from past experiments.

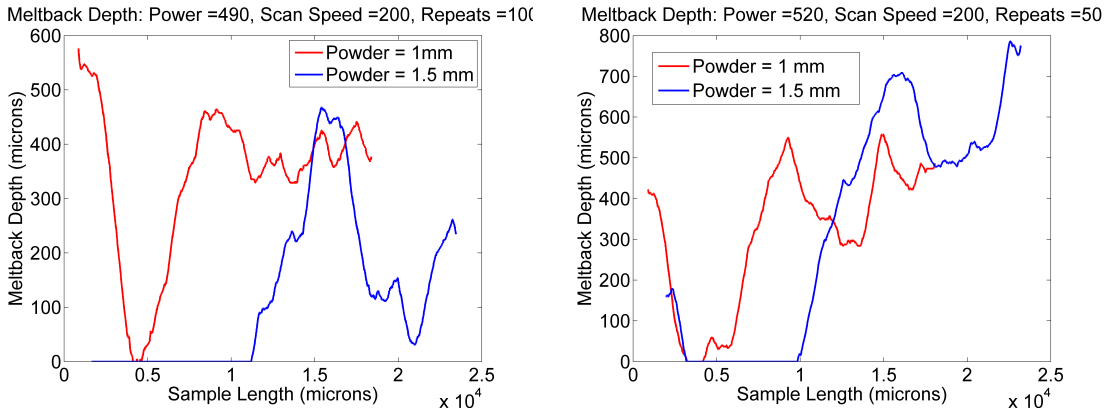

Figure 77: CMSX-4 meltback depth with varying powder thickness.

Finally, the number of repeat scans can be contrasted in Figure 78. The number of repeat scans has a direct relation to the amount of meltback seen in a sample, as shown in the figure with an increase of 50 repeat scans where it increased the meltback depth by over 100 microns. An important trait seen in this plot is that while the meltback depth was increased near the start of the scan, it had little effect on mitigating the drop in meltback near the transition from repeat to raster scans.

This, along with the seemingly little influence the change in raster scans causes with the later meltback in the sample, calls into question its importance to controlling the meltback depth.

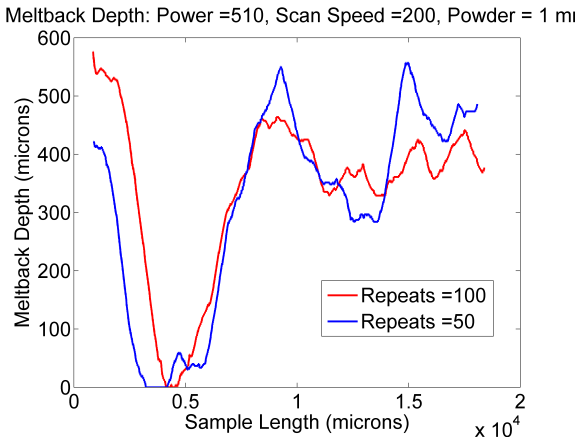

Figure 78: CMSX-4 meltback depth with different number of repeats.

The graph also highlights the importance of preheating the substrate during a run. The reason the meltback depth took longer to approach the zero mark for the larger number of repeat scans is due to the amount of preheats occurring in the substrate. By heating the area that has not yet been processed a greater degree of meltback can be obtained when the meltpool progresses through that region. While increasing the number of repeats does not solve the issue of lack of bonding at the transition from repeat to raster scanning it does show improvement in preheating the substrate.

5.1.3 CMSX-4 Additional Analysis

Two charts were created using the CMSX-4 power density equation. Power density is the relation between the laser power, placing energy into the system, and the scan spacing, held constant between all experiments, the scan speed and the powder thickness. Equation 29 shows the formation of the power density.

$$PowerDensity = \frac{LaserPower}{(ScanSpacing) * (ScanSpeed) * (PowderThickness)} \tag{29}$$

Power density is a commonly used variable with additive manufacturing and weld repair as it allows for a deeper understanding of the energy input into a system and the resulting effects it may have. Shown in Figure 79(a) is the power density being applied to the deposit height for CMSX-4. For each sample the mean height and the standard deviation of the deposit were tabulated and plotted. The red lines are samples that underwent 50 repeat scans and the blue had 100 repeat scans. As can be seen in the graph the data is largely contained in two separate areas, this is caused by the large jump in powder thickness. The lower power density, that has a higher powder thickness, tends to have a much larger variation in deposit height then the higher power density levels. With this larger amount of deposit also comes a greater level of variation in the deposit. The plot shows that having a higher power density leads to a better controlled process but also mitigates the amount of deposit.

The power density was also plotted against the amount of meltback depth found in each sample, Figure 79(b), with red lines having 50 repeat scans and blue lines having 100. The lower power density samples show a lower amount of meltback with a much higher amount of variation than those with higher power density. With many of the lower power density samples the meltback reaches zero at points, meaning there was a lack of fusion in the sample being represented. This higher amount of variation in meltback coupled with the occurrence of lack of fusion during their runs gives a clear indication that a higher power density when processing samples; created through higher power, slower scan speed or lower powder thickness, will lead to samples with a smaller but consistent deposit with a larger meltback depth. Further work can be done for power density between 0.06 and 0.07 J/mm^3 with a powder thickness being left a 1mm. This may lower the amount of meltback, so that it will always be below the maximum allowable amount, while maintaining a good single crystal deposit.

When viewing the primary dendrite angle across multiple samples a trend started to form that had not been noticed during prior analysis. For most samples the

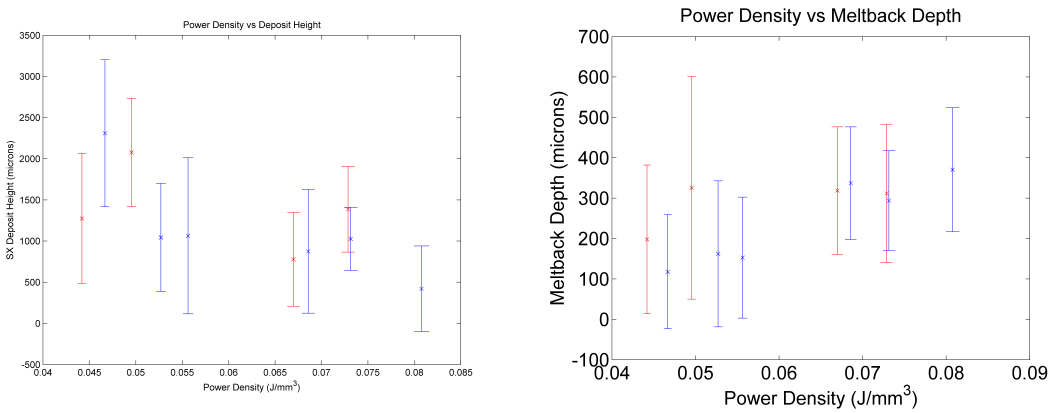

(a) Power Density vs SX Deposit Height

(b) Power Density vs Meltback Depth

Figure 79: CMSX-4 Power Density Plots

dendrite angle is near vertical when the process starts but as the process continues across the sample length the dendrite angle becomes more aligned with the underlying substrates angle, shown on all charts as a zero angle. Typically a CMSX-4 samples cast substrate dendrite angle is within 5 degrees of the vertical but since there is no way to tell which direction the dendrites are facing before the sample is cut and imaged the substrate angle could be leaning forward or back relative to the vertical for each part processed.

When the substrate angle is positive the graphs, shown in Figures 80(a) and 80(b), indicate the newly formed SX angles to begin as negative then progress to zero. When the substrate angle is negative to the vertical, Figures 81(a) and 81(b), the newly deposited dendrite angles are shown as positive in inclination then progressing towards zero to again align with the substrates angles. This could be caused by having a much stronger vertical temperature gradient near the start of the scan then near the end, caused by a larger amount of preheat occurring as the laser progresses across the sample.

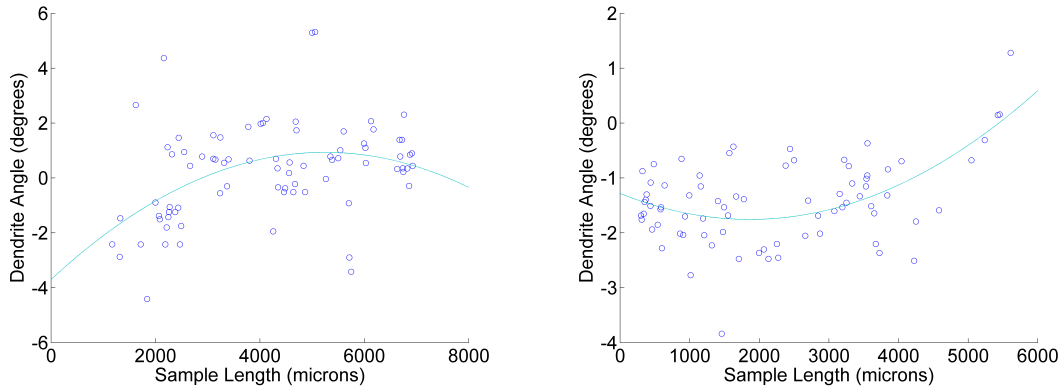

Figure 80: Deposited dendrite angle relative to a positive substrate dendrite angle.

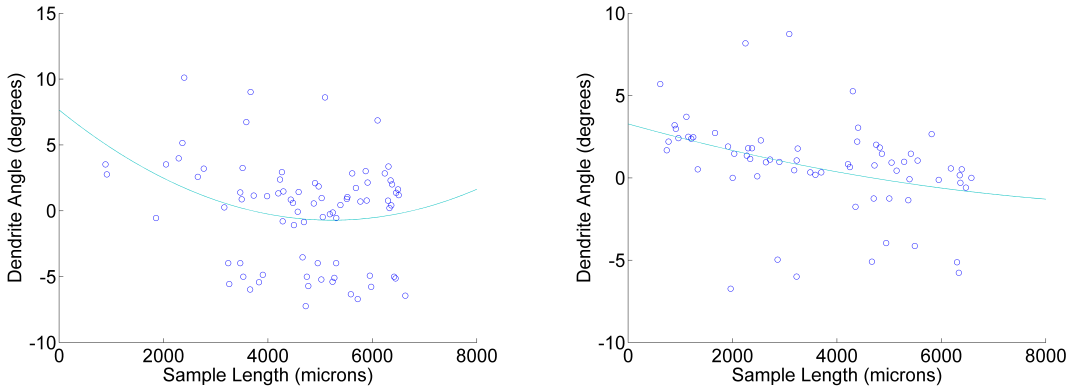

Figure 81: Deposited dendrite angle relative to a negative substrate dendrite angle.

5.2 Data Fitting

5.2.1 René-80 Meltback Depth

After developing the process of calculating the data fitting equations relating a microstructure feature to the processing parameters a large investigation was completed to find the most significant relations. The equations found to be most important when deciding future experimental parameters for René-80 are related to the meltback depth and deposit height.

The meltback depth is portrayed through two means: excessive meltback into the substrate beyond the allowed amount and lack of fusion. When calculating the excessive meltback in the sample, the amount that the meltback exceeds the allowed value is taken into consideration, placing more harm on meltback that vastly exceeds

the set boundary. The data fitting found that using four windows allowed the best insight into how the process behaves.

A contour plot holding repeat scans constant at 200 and raster scan speed constant at 350 mm/sec, shown in Figure 82(a), provides a brief overview on the relation between power, repeat scan speed and the excessive meltback. Table 3 describes the terms used for each window, giving the constant associated with the parameter, with the most significant being highlighted in red. The first window, the initial quarter of the sample, has a linear relation between the parameters and the excessive meltback with the largest importance being the repeat scan speed. This agrees with experimental observations and recent conclusions into the cause of excess meltback at the formation of a meltpool; that by increasing the repeat scan speed the excessive meltback seen in the sample would diminish. For the final three quarters of the sample both linear and combination effects were found to have some level of significance. The raster scan speed and (power)x(repeat scan speed) hold the greatest significance in this section of the scan. Both terms relate to the amount of energy being exerted on the system, the combination effect causing preheating of the substrate during the repeat scans and the raster scan speed maintaining and extending the preheating during the later portion of the sample.

Table 3: René-80 excessive meltback depth data fitting equation terms.
A = Power, B = Repeat SS, C = Raster SS, D = Repeats

	A	B	C	D	AB	AC	AD	BC	BD	CD
Window 1	1	**-2.6**	0.5	0.3						
Window 2	-1	-0.5	**2.5**	2	**5**	0.5		0.5		
Window 3	-0.5	0.1	**1.2**	0.9	**2.5**	0.5		0.5		
Window 4	-4.5	-23	**47**	40	**92**	0.5	-12	21	-24	

The conclusions drawn from the table seem to fit with the basic understanding found with the simple plots explored earlier in the section. In the plots it was found that power alone did not have an adverse effect on the meltback depth later in the scan, agreeing with the lack of importance power alone has in the table. The first section of the sample was also found to be largely effected by the repeat scan speed,

which is in perfect agreement with the first windows conclusion.

The contour plot holding raster scans constant at 200 was created using the quarter window data fitting equations. The plot shows that lower power and higher repeat scan speed will minimize the amount of excessive meltback in the sample. As can be seen in the table, the first window is most influenced by the repeat scan speed with power being a close second which causes this relation to be shown in the contour plot. The contour shows that by controlling the power and repeat scan speed, important both individually and as a combination, the amount of sample preheating undergoes can be monitored. By minimizing the preheating of the sample the amount of excessive meltback will be lowered, giving an improved sample.

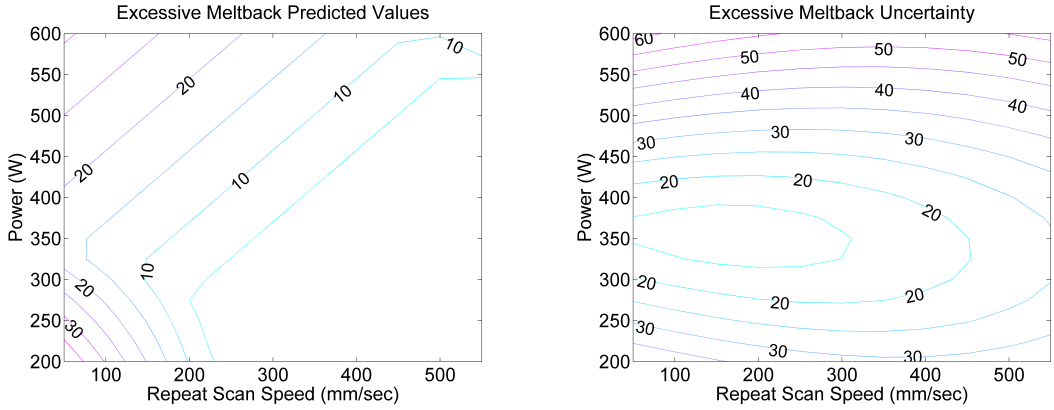

Figure 82: Contour plots showing predicted René-80 excessive meltback depth and data uncertainty.

5.2.2 René-80 Lack of Fusion

The relation between a sample's lack of fusion and the operating parameters was found to be linear for a quarter window fit. As with the excessive meltback depth, the first quarter of the sample is most affected by the laser scanning speed during the repeat scans used to establish the meltpool. It shows that a faster repeat scan speed results in a larger accumulation of lack of fusion. This makes intuitive sense as it most directly influences the establishment of the meltpool and by keeping it too low or high the meltpool may not penetrate the substrate or it may penetrate too

far. The final three quarters of the sample showed a greater relation with the laser power when determining the lack of fusion. The importance of the power level shows that once the meltpool is established and propagating across the sample a higher power will allow the lack of fusion to be minimized by creating a larger meltpool that will be able to extend into the substrate. One final piece of data highlighted in the table is the importance of the raster scan speed during the second quarter of the scan, where a higher scan speed will reduce the lack of fusion in that area. This does not follow the basic principles seen in SLE where a lower raster scan speed will allow the meltpool to penetrate further into the substrate. Since this is weighted so heavily near the transition from repeat to raster scanning, one explanation may be that a faster raster scan speed can best take advantage of preheating created during the repeat scanning.

Table 4: René-80 lack of fusion data fitting equation terms.

A = Pow, B = Rep SS, C = Ras SS, D = Rep

	A	B	C	D
Window 1	-0.2	**2.5**	-0.5	-0.2
Window 2	**-1.3**	-0.6	**-1.4**	-0.3
Window 3	**-1.2**	-0.75	-1	1
Window 4	**-2.5**	-1.5	-0.8	0.8

Figure 83(a), below, has the same value as those for excessive meltback and shows one trend worth noting. As the power becomes a low value the change in repeat scan speed has nearly no effect on the lack of fusion. This follows a pattern we have discovered where a slow heating of the powder when establishing the meltpool can cause the melted powder to form a ball on top of the substrate instead of having the melted powder mix into the substrate. So long as the power is kept at a low setting the speed of the scan has a reduced role as all of the energy entering the system will heat only the powder region. It is only once the scan progresses beyond the initial edge that newly melted powder can heat the sample to a temperature high enough to

induce melting, allowing mixing of the substrate and deposited powder to occur. By this point in the scan, the initial section has already solidified with the melted powder never melting into the sample, causing a poor lack of fusion condition. The contour plot shows that only when the power is high will the repeat scans hold significance.

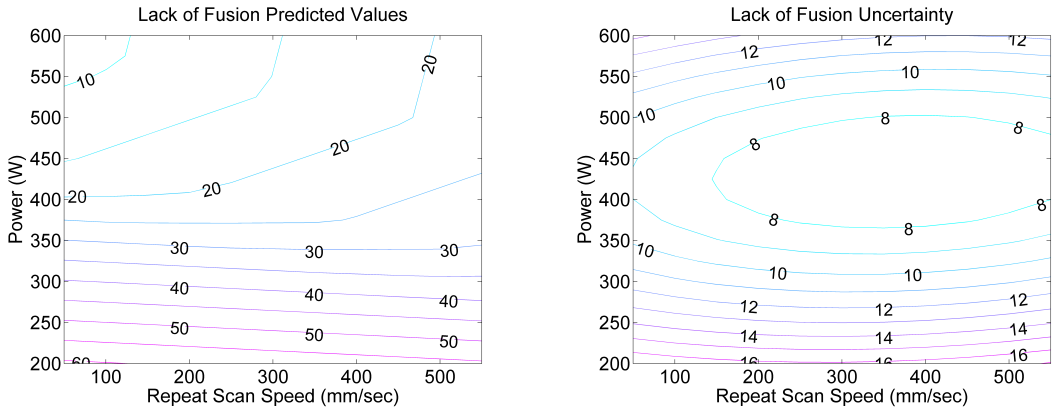

Figure 83: Contour plots showing predicted Rene-80 lack of fusion and data uncertainty.

5.2.3 René-80 Deposit Height

There are several means by which the deposit height can be evaluated across a sample, the one found to be most relevanct is the overall minimum deposit height. After creating a deposit using SLE, the part would need to undergo a contour grinding operation until it has the desired curvature without any crevices across the deposited surface. This makes controlling the minimum deposit height very important as it determines the usable amount of material that has been added to the substrate. A quadratic fit was found to best describe the relation between the minimum deposit and the SLE parameters with the largest importance placed on repeat scan speed and the number of repeat scans, Table 5. This follows a conclusion found earlier in the section when comparing the deposit heights of various samples against one another. By altering the number of repeats and the repeat scan speed the initial deposit can be altered. When the buildup is increased at the starting edge there is a resulting starvation that occurs, usually being the minimum deposit height for the sample.

Table 5: René-80 deposit data fitting equation terms.
A = Power, B = Repeat SS, C = Raster SS, D = Repeats

	A	B	C	D	A^2	B^2	C^2	D^2
Window 1	-1.2	-2	-0.3	1.8	0.2	4.5	1.5	3.5

As can be seen in Figure 84(a) there is a minimum well in the contour with an improved deposit height equally spaced around it, expressed by a larger number. The well is caused in part by the interesting feature described during the plot comparison for the number of repeat scans, where a mid-range of repeats causes a sharper drop in deposit height. A similar type of relationship may be found with the repeat scan speed, leading to the contour plot shown.

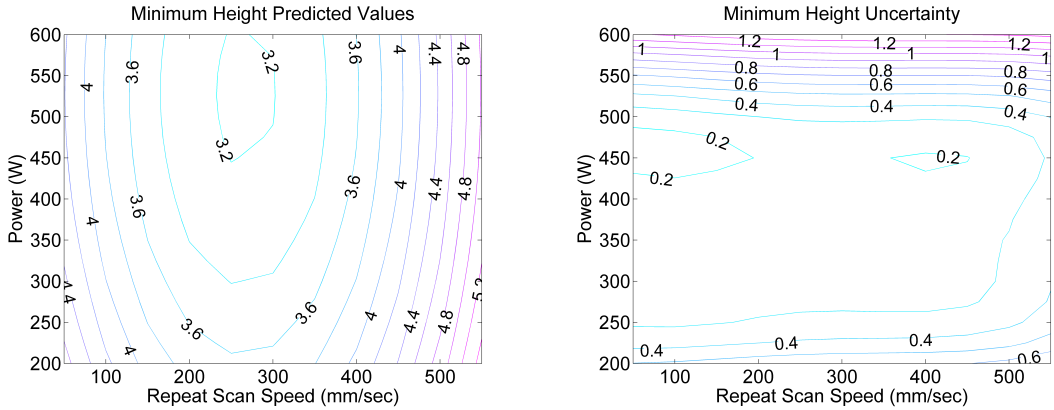

Figure 84: Contour plots showing predicted René-80 deposit height and data uncertainty.

Currently, when a sample is processed with a single large layer deposition there can be a great deal of variation in the total deposit height. So long as the minimum deposit height is larger than the required amount, with the excess areas being ground flat, having a varying height is not a primary issue. The importance for having a smooth deposit does have some significance for later experimentation and any understanding that can be acquired now would be helpful and has been expressed earlier in this section as a possible way to better approach future problems. By depositing a flatter surface there would be less waste in the process, which can bring down the material costs significantly due to the high cost of powder, and would allow more freedom in

choosing other parameters as a larger powder thickness layer would not be necessary.

Having a flat surface is also important for later experiments when attempting multi-layered deposits. If the deposit has a large height variation then it will be impossible to add a new layer of powder over it, creating a point of critical failure in the operation. While single layer deposits can be ground flat a multi-layered deposit cannot be corrected by a similar approach after every deposition. By minimizing the deposit variation now, and therefore gaining a better understanding of the causation behind it, future work will become easier.

Table 6: René-80 deposit variation data fitting equation terms.
A = Power, B = Repeat SS, C = Raster SS, D = Repeats

	A	B	C	D	A^2	B^2	C^2	D^2
Window 1	3.8	0.8	2.4	-1.7	-0.5	**-8.5**	-2.8	-3.3

The analysis found that a single window over the entire sample with a full linear and quadratic fit was enough to relate the deposit variation with little uncertainty, Table 6. While several factors are held as important with height change, the scan speed for the repeat scans has the most significance. This relates well to real tests as the largest shift in deposit height tends to be near the beginning of the deposit, caused by the stationary meltpool as it is being fully formed. During the time of creation, a large amount of powder is able to fall into the meltpool, creating an excessively high deposit, and when the meltpool begins to transverse the sample length the powder immediately available after movement begins has already been lessened. Having access to less powder causes starvation for the meltpool and results in a much lower meltback depth until the powder feeding into the meltpool stabilizes, a symptom seen in an earlier plotting exercise. By better controlling the repeat scan speed this effect can be mitigated in later trials.

The contour plot below shows a peak formation near the top of the operational field that gives the largest variation. The lower values surrounding, especially to the right of the peak, designate a lower variation in sample deposit height. The contour

plot is created with a mid-range raster scan speed and number of repeats and shows that by holding the repeat scan speed to a higher value there will be a lower variation in deposit height. Again, this follows a similar reasoning seen before as a faster repeat scan speed will lesson the impact of the meltpool size and will cause less starvation.

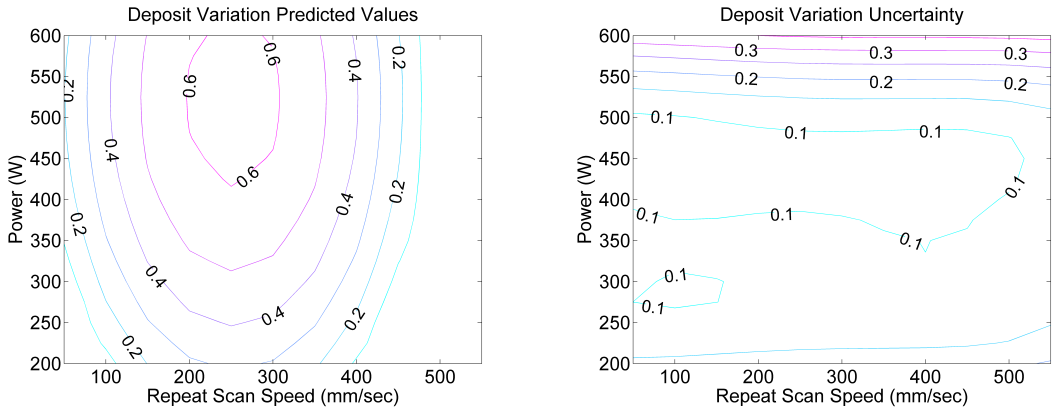

Figure 85: Contour plots showing predicted René-80 deposit height variation and data uncertainty.

5.2.4 René-80 Combined Data Fitting

Once all of the major relations between features and settings were found they were normalized and combined into one final system representing the operating map for René-80, Figure 86. The uncertainty values for each point were also combined in a separate matrix.

A search was completed looking into each calculated uncertainty value, a combination of the individual fitted uncertainties, looking for those within a high and medium confidence. The high confidence points designate regions that have already been explored, or areas that are extremely well represented, while the medium confidence denotes areas of interest that may provide greater understanding to the overall process mapping. The ideal parameters within these two ranges are found, giving the locations for the best future operating parameters. For René-80 the best operating points were found in the medium confidence range; carrying the significance that future testing is needed before an optimal area is located with high confidence. The

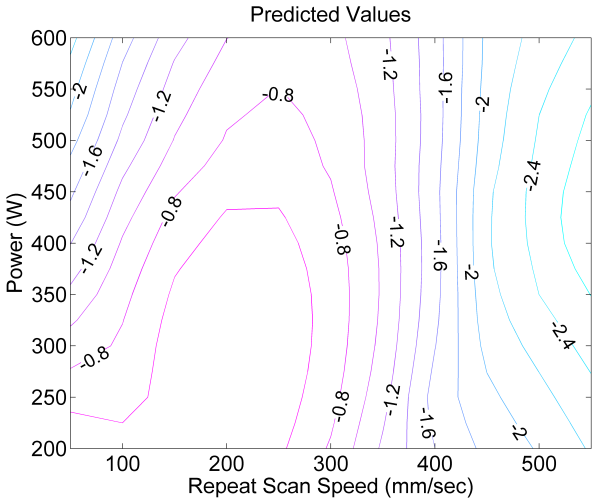

Figure 86: René-80 combine contour plots for future point selection.

contour plot shows the region of interest, power being 400W and repeat scan speed of 450, which should provide improved results.

Using the suggested points a fractional factorial DOE was created in Matlab using a range provided by the user. Since the area for future testing was found to be in the medium confidence range, suggesting further exploration of the operating parameters before isolating the optimal area, a fractional factorial DOE is created. The DOE list, Table 7, is a Resolution 4, 2 Level DOE that will provide insight into the area of interest and give greater detail for first order effects.

Table 7: Rene-80 future trials

Power	SS Repeats	SS Raster	Repeats
350	450	500	350
350	450	600	450
350	550	500	450
350	550	600	350
450	450	500	450
450	450	600	350
450	550	500	350
450	550	600	450

5.2.5 CMSX-4 Excessive Meltback Depth

Performing the same procedure as done with the René-80 samples yields several relations between the CMSX-4 microstructure and the SLE parameters worth exploring.

The first area of analysis for CMSX-4 samples is excessive meltback depth. The analysis found that two windows, each representing fifty percent of the total sample length, would best express the relation, Table 8. The first half of the sample has a linear relation that stresses the powder height as the main relation to excessive meltback depth. This agrees with the plots compared earlier as an increasing amount of powder will cause the meltpool to not fuse the new material with the substrate. Though this is an undesirable trait for the SLE process, in terms of excessive meltback depth it is ideal. The second half of the sample has a quadratic relation that places the greatest importance on the scan speed. This would best relate to the amount of preheating the system will undergo later in the sample. It was found during experimentation that as the scan speed decreases, slowing the progression of the meltpool across the sample during processing, the meltback will become more excessive during the later portion of the scan.

Table 8: CMSX-4 excessive meltback depth data fitting equation terms.

A = Power, B = Scan Speed, C = Repeats, D = Powder Thickness								
	A	B	C	D	A^2	B^2	C^2	D^2
Window 2	0.9	-0.7	1.5	**-3.8**				
Window 1	2.25	0.3	1.6	2	1.3	**-2.5**		

The contour, Figure 87(a), shows that having a high scan speed lowers the chance for excessive meltback depth, agreeing with the experimental observations described above. An issue displayed on the second contour plot below is the large amount of uncertainty. While the data equations were deemed relevant, having an F-Value of 5.022 which exceeds the F-Value of 4 needed, the information still has a great deal of variation.

5.2.6 CMSX-4 SX Deposit

When creating a relation equation that represents the SX deposit height, the equation denotes the best samples with a larger value, that directly correlates with the amount

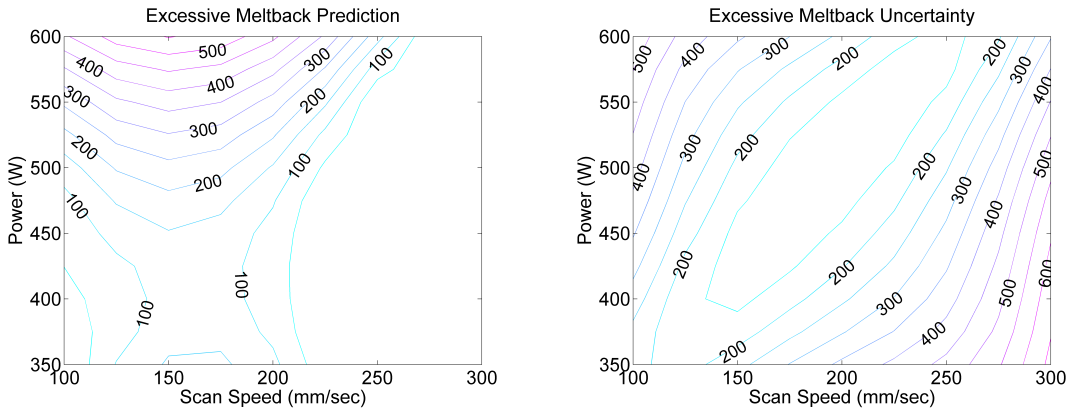

Figure 87: Contour plots showing predicted CMSX-4 excessive meltback and data uncertainty.

of powder being deposited. The average single crystal deposit height relative to the underlying substrate was found to have a quadratic fit, encompassing the entire sample, that is greatly affected by the powder thickness term squared as seen in Table 9. This agrees with the observation made earlier that the greater amount of powder made available during a scan, the larger the SX deposit will be. A second parameter that influences the deposit height is the number of repeat scans. Fewer repeat scans will lead to a reduction in initial buildup and the subsequent starvation in the sample.

Table 9: CMSX-4 SX deposit data fitting equation terms.

A = Power, B = Scan Speed, C = Repeats, D = Powder Thickness

	A	B	C	D	A^2	B^2	C^2	D^2
Window 1	-5.5	4.5	**-6.2**	5.8		-4.5		**6.1**

The contour plot, Figure 88(a), displays a hill with an increasing amount of SX deposit as the power is kept lower and the scan speed is increased. To best maximize the SX deposit height the chart shows that having a high or low power would be best, though this would prove problematic when paired with the other features tracked. Additional investigation was done in the single crystal deposit height, such as a minimum deposit amount, but the data fitting equations found were not accurate enough given the information provided. The code to investigate these SX descriptors are still available and may provide insight into the deposit given more information

after conducting future experiments.

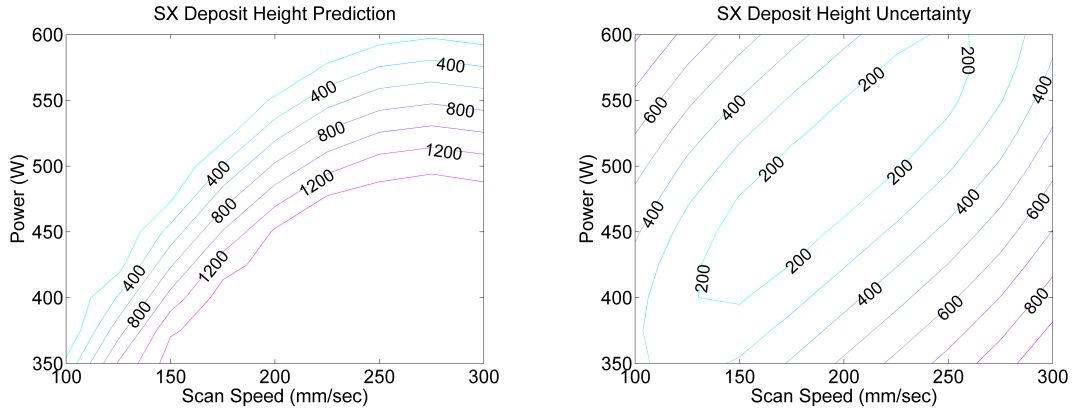

Figure 88: Contour plots showing predicted CMSX-4 SX deposit height and data uncertainty.

When creating the single-crystal deposit, it is important that a large variation in height is avoided so that a more consistent and overall larger deposit can be made, the reduction in variation is represented as a lower number generated in the data equation. Both the power and powder thickness were found to be significant, in a quadratically fitted single window equation, when maintaining an even deposit. As shown when investigating the SX deposit height, the powder thickness has a great level of influence into the upper threshold on the deposit, allowing it to best affect both the mean and variation. An interesting effect found in the table is that an increase in power level will cause a decrease in the height variation.

Table 10: CMSX-4 SX deposit variation data fitting equation terms.

A = Power, B = Scan Speed, C = Repeats, D = Powder Thickness

	A	B	C	D	A^2	B^2	C^2	D^2
Window 1	-0.5	0.75	-1.3	0.75	-2.75			0.1

The contour plot, 89(b), holds the powder thickness constant at 1.5mm and the repeats at 100. The area of highest SX variation overlaps partially with increasing mean deposit height shown in the previous figure. This follows the basic reasoning that a larger deposit height will allow a larger variation. The plot shows that by avoiding an operating range of 400 to 500 Watts with high scan speed the maximum

variation can be avoided while still maintaining a large deposit as seen in Figure 89(a), which can be used to influence the next set in a future DOE.

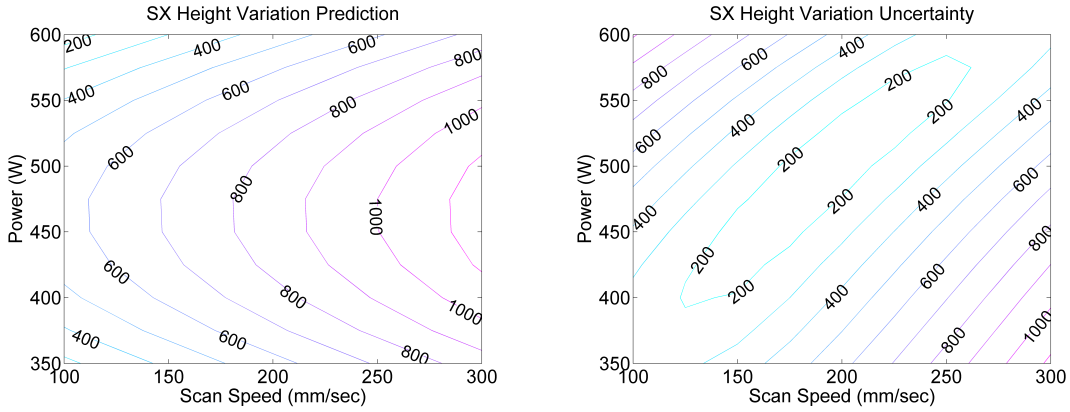

Figure 89: Contour plots showing predicted CMSX-4 SX deposit height variation and data uncertainty.

5.2.7 CMSX-4 Sample Deformation

The final area of exploration for CMSX-4 data fitting is the amount of deformation that is found in the substrate. Substrate deformation is caused by a large amount of energy being sent into the system causing the part to warp. The amount of substrate deformation seen in CMSX-4 samples tends to be small, but an analysis of the feature does find a relation between the SLE parameters and the amount of possible warping. The two highest order affects on sample deformation are power and scan speed as shown in Table 11. This makes intuitive sense as the two parameters are most responsible for the amount of energy being supplied into the part during processing. By raising the power level or decreasing the scan speed the amount of energy entering the system increases. As the amount of energy entering the system raises to a high level there is a chance that warping can occur; this problem has been witnessed with several samples when early runs are conducted on a new material.

As can be seen in the contour plot, Figure 90(a), the ideal region of operation to avoid warping is at a medium power and scan speed range while holding powder thickness constant at 1.5mm and repeats at 150. The plot shows that a scan speed

Table 11: CMSX-4 sample deformation data fitting equation terms.

A = Power, B = Scan Speed, C = Repeats, D = Powder Thickness								
	A	B	C	D	A^2	B^2	C^2	D^2
Window 1	1.25	0.25	-1	4	-5	8.5		

at either extreme will lead to a bad case of warping, though the higher scan speed range is also subject to a much larger amount of error in the estimate.

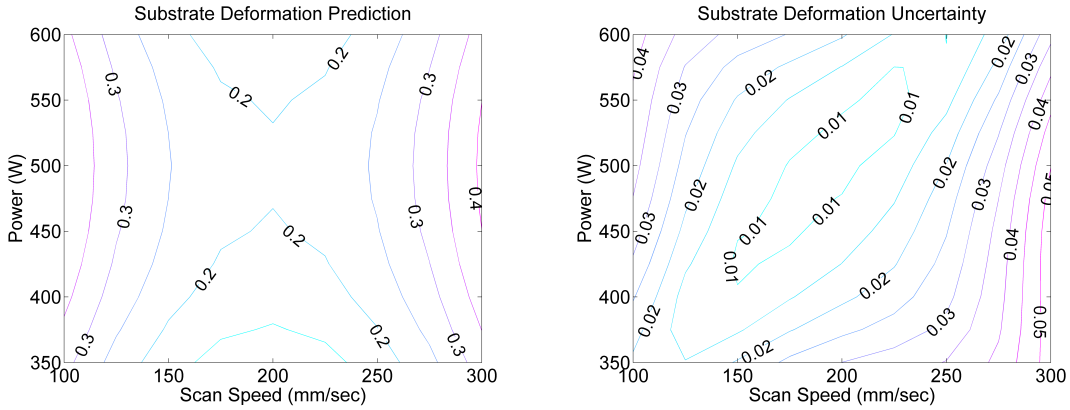

Figure 90: Contour plots showing predicted CMSX-4 substrate deformation and data uncertainty.

5.2.8 CMSX-4 Combined Data Fitting

The feature tracking relation equations described above can be normalized and combined to provide insight into where future trials should be located. When combining the relation equations a larger weight is provided to the excessive meltback depth, the mean deposit height and the variation in deposit height, diminishing the overall affect of the substrate deformation. The combined affects can be seen in Figure 91 where a lower value denotes a better observed outcome. There is a single area on the contour that shows a clear improvement in the samples, at a power level around 500 Watts and a high scan speed. When outputting the three areas of highest interest in the CMSX-4 combinational contour all three pointed to the same vicinity, as expressed in the red region. It gave a power variation between 500 and 550 as the locations of interest, giving further insight into where to place future experiments.

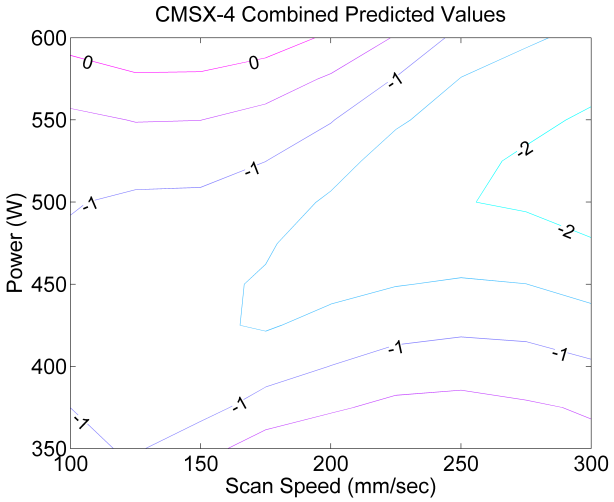

Figure 91: Combined CMSX-4 contour plots for future point selection.

Since the area of suggested further study was not in a location of high certainty, which would have denoted an optimal zone, a fractional factorial DOE is the best type of design to implement. As described above, the points of interest that were given by the program provide the location and range of the generated DOE.

Table 12: CMSX-4 future trial runs

Power	Scan Speed	Repeats	Powder Thick
500	225	175	1
500	225	225	1.5
500	275	175	1.5
500	275	225	1
550	225	175	1.5
550	225	225	1
550	275	175	1
550	275	225	1.5

CHAPTER VI

FUTURE WORKS

6.1 Secondary Dendrite Arm Space Tracking

There are several areas of this thesis that can be investigated and further explored. In regards to the microstructure tracking aspect, an additional feature that could provide insight into the process is tracking the secondary dendrite arms found in a single crystal deposit. The secondary dendrite arm spacing is affected by the cooling rate as the material solidifies, so knowing how it changes during the process or between different samples will provide insight into how the meltpool behaves during operation. The secondary arms can be tracked using the primary dendrite trunk width information. Knowing where the trunk ends, and the secondary arms begin, means that the search needs to be conducted just beyond the traced section. The procedure used to better exemplify the primary dendrite arms can be augmented to highlight the secondary arms instead. Blurring in a direction perpendicular to the primary dendrite angle can provide a clearer image of the secondary arms while mitigating the primary dendrites.

6.2 Stray Grain Tracking

In CMSX-4 samples it would be beneficial to also track the stray grain formations, both their location and size. The number of stray grains must be kept to a minimal level in fabrication of acceptable parts, so gaining further insight into how they are created could prove beneficial in subsequent trials. Stray grain formations have been a common area of research for Ni-based superalloy welding techniques and continue to hold a great deal of interest in the industry [43, 47]. Most major stray grains could

be found by investigating regions within the single-crystal zone that do not contain tracked primary dendrites. Instead of using a procedure to find angles close to the vertical direction, steps could be taken to search at several other angles. Checking these areas for primary dendrites at irregular angles, compared to the single-crystal zone at large, would be a large indication of stray grains. Another technique to be considered uses the fact that many stray grains will be formed at the meltback line. This gives a smaller area to explore for major stray grains and can simplify the process.

6.3 Further Testing

The data analysis and fitting operations detailed in this thesis make use of all the information currently available for CMSX-4 and Rene-80 parts. The best way to improve the analysis and find further relations is to increase the number of trials for each material, run the microstructure investigation program and perform another set of data fitting runs. The analysis portion of this thesis was designed to allow for future trials to be easily included with the current information and will provide no undue effort to expand the data set.

6.4 René-80 Void Mitigation

When investigating the voids found in René-80 there was no correlation found between the laser power, scanning speeds or repeats and the resulting voids. Since the main cause of voids is impurities in the meltpool, causing poor resolidification, a series of experiments could be conducted to mitigate the void formation. By tracking how the powder is prepared, loaded onto the substrate and the operating conditions within the chamber, the data fitting program can be applied. A specific technique in preparing and processing the samples could provide greater results for void mitigation which would provide higher quality samples than are currently possible.

6.5 Additional DOE Work

Another area for future improvement is in the DOE portion of the program. Currently the program can only provide two types of experimental setups, fractional factorial or response surface. These two types provide the most important designs when it comes to exploring and mapping a process but additional steps can be applied. In some cases, other types of DOE's are better suited for analysis, such as a Taguchi L9, a type of fractional factorial DOE that was designed for three level factors. Improvements can also be made to the current fractional factorial generator. An example would be giving it the ability to be rotated to provide more useful information while maximizing the orthogonality to the global data.

CHAPTER VII

CONCLUSION

The primary goal of this thesis was to allow for a better understanding of the relationships between the SLE processing parameters and the resulting microstructure found in CMSX-4 and René-80 samples produced through this technique. To accomplish this goal, three areas of research were pursued: (1) Tracking of the major microstructural features prevalent in the two materials in question; (2) Providing the experimenter with the microstructural feature information in a way that would provide an easy comparison between various SLE settings; and (3) Finally using the data fitting equations to find higher level interactions between the parameters and responses. All three sections were successfully completed, giving results that provide greater insights into the SLE process and supplying areas for further investigation.

The microstructure tracking program allows all of the major features found in CMSX-4 and René-80 samples to be isolated and saved for future use. The program is sufficiently robust such that it works for samples at different locations in the image, various brightness levels, and contrast states. It can also mitigate the error caused by blurred image sections and scratches along the surface. There are two ways in which the program improves upon the standard found in industry. First, it is able to track features that have not been isolated before in single-crystal and equiaxed deposits. This provides the user with the ability to better comprehend complex aspects of the process. The second area of improvement is the rate of return on the information. Using an optical microscope as the sole source of microstructural data, program has a turn-around time of minutes once it is supplied a sample image. This helps with the features never before tracked but also provides a benefit to microstructural features

that are able to be determined with other methods. Having a fast and accurate system in place to provide feedback for future experiments can cut down on the number of erroneous experiments and mitigate material and man-power costs.

Visual comparisons allow for the experimenter to grasp a deeper meaning of the lower order effects between a process parameter setting and the resulting microstructure. Being able to see patterns, or the absence of, can provide the user with a more robust understanding. Information that normally is difficult to observe in detail, such as the fluctuation in meltback depth when looking at a micrograph, can now be easily compared and better conclusions can be drawn in doing so.

The final area of the thesis was to provide a deeper understanding of the SLE parameters and the subsequent microstructure characteristics. Through the use of windowing the data and applying various data fitting equations to each window, the best representation of the data is located. The terms in each equation provide insights into how the different settings weigh on the microstructure in question. Using this information to predict future points, and their level of accuracy, allows the thesis to give direct feedback to the SLE process. Using the fast turnaround time involved with the thesis program each subsequent set of trials can be influenced by the previous samples created, increasing the rate at which the optimal parameters are found while also minimizing the total amount of wasted coupons and material.

This thesis provides several contributions to both optical metallography and additive manufacturing. Several features that have been detailed in this thesis, such as dendrite angles, are capable of being tracked using current optical metallography techniques. The improvement in this area is in the capability of now accomplishing these tasks using a simpler and easier interface, an optical microscope, instead of more complex methods such as EBSD. Areas that have not been explored before in optical metallography have also been investigated in the thesis. Tracking transitions between different types of manufacturing techniques, single-crystal primary trunk widths and

others are areas that have not been explored previously.

Designing the optical metallography specifically for additive manufacturing is another significant area of improvement. The additive manufacturing field for alloys is newly formed and has not been a primary focus of optical metallography in the past. This thesis provides significant improvements in bringing optical metallography into this area. Finding transition points between layers can provide a greater level of insight into where and when errors occur in a process. It also gives the user the ability to better understand how the parameters involved with the additive manufacturing field effect the created part. The feature tracking software has been created using Scanning Laser Epitaxy samples but since the program tracks microstructural features found in any type of additive manufacturing technique involving alloys it can be altered to work with other processes.

While significant improvements have been made in tracking microstructural features one of the greatest accomplishments of this thesis is the coupling of the optical microscopy with the data analysis. Normally when finding a data fitting equation or analyzing a DOE, the information must be tabulated outside of the statistical program. This provides limitations on how the data can be analyzed and interpolated. By allowing the statistical program access to all of the available data, some of which hold thousands of data points, it is faster and easier to run more complex analysis. Previously it was difficult to accurately describe the meltback depth of a sample to a DOE program, and it was impossible to consider its slope across the sample. Using the programs created in this thesis, both types of analysis can be conducted quickly and easily. Saving all of the microstructure information and allowing the statistical program direct access to the information allows for previously created samples to stay relevant. When the statistical program is separate from the total data repository, it is limited to whatever the user inputs. This causes data fitting equations to be created with only the information from one DOE. The program created gives

the data fitting equations the ability to recall any and all information available from prior experiments. This gives the user the opportunity to have more accurate results while minimizing the amount of experiments that must be conducted.

This thesis brings optical analysis and image processing directly in line with additive manufacturing. As time goes on, this area of investigation will become more important as more and increasingly complex products are created using additive manufacturing. This thesis highlights some of the most important features that can be found in this manufacturing field for alloys and provides areas for several improvements in future work. The idea of directly linking data analysis with image processing gives another area of growth for the industry. With the current speed of computers and the low cost of data retention it is clear that having access to the most amount of information for a statistical program will yield great results with no negative impacts.

REFERENCES

[1] "Cast nickel base alloy," Oct. 26 1971. US Patent 3,615,376.

[2] Agarwala, M., Bourell, D., Beaman, J., Marcus, H., and Barlow, J., "Direct selective laser sintering of metals," *Rapid Prototyping Journal*, vol. 1, no. 1, pp. 26–36, 1995.

[3] Atwood, C., Ensz, M., Greene, D., Griffith, M., Harwell, L., Reckaway, D., Romero, T., Schlienger, E., and Smugeresky, J., "Laser engineered net shaping (lens (tm)): A tool for direct fabrication of metal parts," tech. rep., Sandia National Laboratories, Albuquerque, NM, and Livermore, CA, 1998.

[4] Bezerra, M., Santelli, R., Oliveira, E., Villar, L., and Escaleira, L., "Response surface methodology (rsm) as a tool for optimization in analytical chemistry," *Talanta*, vol. 76, no. 5, pp. 965–977, 2008.

[5] Blake, A., Isard, M., and others, *Active Contours*, vol. 1. Springer London, 2000.

[6] BLANTHER, J., "Manufacture of contour relief-maps," May 3 1892. US Patent 473,901.

[7] Bourell, D., Beaman, J., Leu, M., and Rosen, D., "A brief history of additive manufacturing and the 2009 roadmap for additive manufacturing: looking back and looking ahead," in *US-Turkey Workshop on Rapid Technologies*, 2009.

[8] Box, G. and Hunter, J., "The 2 kp fractional factorial designs," *Technometrics*, vol. 3, no. 3, pp. 311–351, 1961.

[9] Bradski, G. and Kaehler, A., *Learning OpenCV: Computer vision with the OpenCV library*. O'Reilly Media, Incorporated, 2008.

[10] Breu, H., Gil, J., Kirkpatrick, D., and Werman, M., "Linear time euclidean distance transform algorithms," *Pattern Analysis and Machine Intelligence, IEEE Transactions on*, vol. 17, no. 5, pp. 529–533, 1995.

[11] Bunker, R., "A review of turbine blade tip heat transfer," *Annals of the New York Academy of Sciences*, vol. 934, no. 1, pp. 64–79, 2001.

[12] Canny, J., "A computational approach to edge detection," *Pattern Analysis and Machine Intelligence, IEEE Transactions on*, no. 6, pp. 679–698, 1986.

[13] Chan, T. and Vese, L., "An active contour model without edges," *Scale-Space Theories in Computer Vision*, pp. 141–151, 1999.

[14] Clemex, "Porosity and crack analysis," *Image Analysis Report*.

[15] Curtis, C., "Apparatus for generating mechanical power," Oct. 31 1899. US Patent 635,919.

[16] Donachie, M. and Donachie, S., *Superalloys: a technical guide*. Asm Intl, 2002.

[17] Drawin, S., "European commission research and innovation."

[18] Flanagan, C., "The bresenham line-drawing algorithm," 2009.

[19] Flood, S. and Hunt, J., "Columnar and equiaxed growth: Ii. equiaxed growth ahead of a columnar front," *Journal of Crystal Growth*, vol. 82, no. 3, pp. 552–560, 1987.

[20] Fullagar, K., Broomfield, R., Hulands, M., Harris, K., Erickson, G., and Sikkenga, S., "Aero engine test experience with cmsx-4 alloy single crystal turbine blades," *Am Soc Mech Eng Pap*, pp. 1–12, 1994.

[21] Gäumann, M., Bezencon, C., Canalis, P., and Kurz, W., "Single-crystal laser deposition of superalloys: processing-microstructure maps," *Acta Materialia*, vol. 49, no. 6, pp. 1051–1062, 2001.

[22] Gäumann, M., Henry, S., Cleton, F., Wagniere, J., and Kurz, W., "Epitaxial laser metal forming: analysis of microstructure formation," *Materials Science and Engineering: A*, vol. 271, no. 1, pp. 232–241, 1999.

[23] Gibson, I., Rosen, D., and Stucker, B., *Additive manufacturing technologies: rapid prototyping to direct digital manufacturing*. Springer Verlag, 2009.

[24] Glavicic, M., Sargent, K., Kobryn, P., and Semiatin, S., "The repair of single crystal nickel superalloy turbine blades using laser engineered net shape (lens) technology," tech. rep., DTIC Document, 2003.

[25] Haralick, R., Sternberg, S., and Zhuang, X., "Image analysis using mathematical morphology," *Pattern Analysis and Machine Intelligence, IEEE Transactions on*, no. 4, pp. 532–550, 1987.

[26] Humphreys, F., "Characterisation of fine-scale microstructures by electron backscatter diffraction (ebsd)," *Scripta Materialia*, vol. 51, no. 8, pp. 771–776, 2004.

[27] Hunt, J., "Steady state columnar and equiaxed growth of dendrites and eutectic," *Materials Science and Engineering*, vol. 65, no. 1, pp. 75–83, 1984.

[28] Kass, M., Witkin, A., and Terzopoulos, D., "Snakes: Active contour models," *International Journal of Computer Vision*, vol. 1, no. 4, pp. 321–331, 1988.

[29] Kichenassamy, S., Kumar, A., Olver, P., Tannenbaum, A., and Yezzi, A., "Gradient flows and geometric active contour models," in *Computer Vision, 1995. Proceedings., Fifth International Conference on*, pp. 810–815, IEEE, 1995.

[30] Kruth, J., Froyen, L., Van Vaerenbergh, J., Mercelis, P., Rombouts, M., and Lauwers, B., "Selective laser melting of iron-based powder," *Journal of Materials Processing Technology*, vol. 149, no. 1, pp. 616–622, 2004.

[31] Lefebvre, A., *Gas turbine combustion*. CRC, 1999.

[32] Marr, D. and Hildreth, E., "Theory of edge detection," *Proceedings of the Royal Society of London. Series B. Biological Sciences*, vol. 207, no. 1167, pp. 187–217, 1980.

[33] Matsubara, K., "Molding method of casting using photocurable substance," *Japanese Kokai Patent Application, Sho*, vol. 51, no. 10813, p. 1974, 1976.

[34] Maurer Jr, C., Qi, R., and Raghavan, V., "A linear time algorithm for computing exact euclidean distance transforms of binary images in arbitrary dimensions," *Pattern Analysis and Machine Intelligence, IEEE Transactions on*, vol. 25, no. 2, pp. 265–270, 2003.

[35] Myers, R., Montgomery, D., and Anderson-Cook, C., *Response surface methodology: process and product optimization using designed experiments*, vol. 705. John Wiley & Sons, 2009.

[36] Nickel, A., Barnett, D., and Prinz, F., "Thermal stresses and deposition patterns in layered manufacturing," *Materials Science and Engineering: A*, vol. 317, no. 1, pp. 59–64, 2001.

[37] Park, J., Babu, S., Vitek, J., Kenik, E., and David, S., "Stray grain formation in single crystal ni-base superalloy welds," *Journal of Applied Physics*, vol. 94, p. 4203, 2003.

[38] Pitteway, M., "Algorithm for drawing ellipses or hyperbolae with a digital plotter," *The Computer Journal*, vol. 10, no. 3, pp. 282–289, 1967.

[39] Pollock, T. and Argon, A., "Creep resistance of cmsx-3 nickel base superalloy single crystals," *Acta Metallurgica et Materialia*, vol. 40, no. 1, pp. 1–30, 1992.

[40] Reed, R., *The superalloys: fundamentals and applications*. Cambridge Univ Pr, 2006.

[41] Safari, J. and Nategh, S., "On the heat treatment of rene-80 nickel-base superalloy," *Journal of Materials Processing Technology*, vol. 176, no. 1, pp. 240–250, 2006.

[42] Stanford, N., Djakovic, A., Shollock, B., McLean, M., DSouza, N., and Jennings, P., "Seeding of single crystal superalloys—-role of seed melt-back on casting defects," *Scripta Materialia*, vol. 50, no. 1, pp. 159–163, 2004.

[43] Vitek, J., "The effect of welding conditions on stray grain formation in single crystal welds–theoretical analysis," *Acta Materialia*, vol. 53, no. 1, pp. 53–67, 2005.

[44] Vitek, J., Babu, S., and David, S., "Welding of single-crystal nickel-based superalloys," *Mathematical Modeling of Weld Phenomena*, vol. 7, pp. 235–250, 1996.

[45] Vitek, J., Babu, S., David, S., and Park, J., "Microstructure development in single crystal welds," in *Materials Science Forum*, vol. 426, pp. 4123–4128, Trans Tech Publ, 2003.

[46] Wang, W., Lee, P., and McLean, M., "A model of solidification microstructures in nickel-based superalloys: predicting primary dendrite spacing selection," *Acta Materialia*, vol. 51, no. 10, pp. 2971–2987, 2003.

[47] Yang, X., Dong, H., Wang, W., and Lee, P., "Microscale simulation of stray grain formation in investment cast turbine blades," *Materials Science and Engineering: A*, vol. 386, no. 1, pp. 129–139, 2004.

[48] Yates, F., "Sir ronald fisher and the design of experiments," *Biometrics*, vol. 20, no. 2, pp. 307–321, 1964.

[49] Younossi, O., Arena, M., Moore, R., Lorell, M., and Mason, J., "Military jet engine acquisition: Technology basics and cost-estimating methodology," tech. rep., DTIC Document, 2002.

[50] Zhang, J. and Singer, R., "Hot tearing of nickel-based superalloys during directional solidification," *Acta Materialia*, vol. 50, no. 7, pp. 1869–1879, 2002.

[51] Zong, G., Wu, Y., Tran, N., Lee, I., Bourell, D., Beaman, J., and Marcus, H., "Direct selective laser sintering of high temperature materials," in *Solid Freeform Fabrication Symposium Proceedings, The University of Texas at Austin*, pp. 72–85, DTIC Document, 1992.